Searching for Non-Standard Model Highly Ionizing Processes and Long-Lived Neutral Particles With the MoEDAL-MAPP Detector

by

Alejandro Alberto Salazar Lobos

A thesis submitted in partial fulfillment of the requirements for the degree of

Master of Science

Department of Physics

University of Alberta

Abstract

The Monopole & Exotics Detector at the Large Hadron Collider (MoEDAL) is designed to search for highly ionizing particle avatars of physics beyond the Standard Model of particle physics. Phase 1 of the MoEDAL Apparatus for Penetrating Particles (MAPP-1) upgrade is currently being installed to take data at LHC's Run-3. MAPP-1 is designed to extend the discovery horizon of MoEDAL to include sensitivity to feebly interacting particles such as mini-charged particles, as well as very long-lived charged and neutral particles. Phase 2 of the MAPP detector, MAPP-2, will be installed in LS3 of the LHC for data taking during LHC's Run-4 which is scheduled to start in 2029. MAPP-2 is designed to greatly extend the sensitivity of the MoEDAL-MAPP detector to long-lived neutral particles. This thesis reports contributions to four main areas in the development of the MAPP-1 and MAPP-2 detector systems. The first contribution is the planning and fabrication of the main scintillator elements of the MAPP-1 detector and the LED calibration system. The second contribution details the testing of the PMT readout for the scintillating elements of MAPP-1. A third contribution presents a refinement to the calculation of ionization energy loss for a neutral particle with an anomalously large EDM. An example of such a particle has been hypothesized to be a fourth-lepton generation Majorana particle through a heavy neutrino, a member of a fourth generation lepton doublet with an anomalously large EDM. A fourth topic of the thesis work is the development of prototype tracking and vertexing software for MAPP-2. Here, it was shown that vertex resolutions around 2.0 cm in all dimensions could be achieved using a scintillator tile technology utilizing X-Y WLS fibre readout with a 1 cm pitch.

"A theory with mathematical beauty is more likely to be correct than an ugly one that fits some experimental data" - Paul Dirac

"It doesn't matter how beautiful your theory is, it doesn't matter how smart you are. If it doesn't agree with experiment, it's wrong" - Richard Feynman

This thesis is dedicated to those who find beauty in truth

Acknowledgements

I express my gratitude towards by supervisors, Dr. James L. Pinfold and Dr. Marc de Montigny. Thanks to Jim, for sharing his expertise in Experimental Particle Physics and his life anecdotes. Thanks to Marc, for sharing his knowledge on Theoretical Particle Physics, showing me new jazz music, and for the times that we went to the movie theater to take a break from academic work. Also special thanks to Javier Andrés Chávez, for introducing me to Physics, back in 2012; for showing me his approach to scientific knowledge under the light of the humanities.

Special thanks to Antonio Vinagreiro, for his excellent machining work and his help on 3D design and printing, and for the knowledge we exchanged on art, history, and politics. Thanks to Dr. Richard Soluk, for his guidance in technical matters. A thank you to Dr. Carsten Krauss, for lending his clean room facility. Special thanks to Dr. Juan Pablo Yanez for lending me the pulsing laser facility. My gratitude as well towards Andreas Gaertner and Tian Ooi, for helping me in getting familiar with the equipment and software necessary to operate the laser. Also thanks to Dr. Mark Freeman, for allowing me to use The Shack's 3D printing and laser engraving equipment.

Thanks to Ameir Shaa and Michael Staelens as well, for their valuable support in the theory part of this thesis concerning the calculations of the energy loss of an electric dipole moment. My gratitude also towards Pierre-Philippe Ouimet, for sharing his knowledge on Quantum Field Theory with me.

I also want to acknowledge the support I received from my parents, Rodolfo Salazar and Daisy Lobos. Thanks to Rodolfo for encouraging me to study Physics at the university level, and for teaching me to be simple and honest when making life decisions. Thanks to Daisy, for her time during the countless hours we pondered on topics on philosophy and logic, and their relation to my studies and personal projects.

Table of Contents

List of Tables

List of Figures

Acronyms

ATLAS
: A Toroidal LHC ApparatuS

BSM
: Beyond the Standard Model

CERN
: "European Council for Nuclear Research", from French "Conseil Européen pour la Recherche Nucléaire"

CM
: Center of Mass

CMS
: Compact Muon Solenoid

CLLP
: Charged Long-Lived Particles

DY
: Drell-Yan

EDM
: Electric Dipole Moment

FIP
: Feebly Interacting Particle

GPD
: General Purpose Detector

GUT

Grand Unified Theory

GWS Electroweak Theory

Glashow-Weinberg-Salam Electroweak Theory

HECO

High-Electric-Charge Object

HIP

Highly Ionizing Particle

HL-LHC

High Luminosity LHC

LHC

Large Hadron Collider

LLCP

Long-Lived Charged Particle

LLP

Long-Lived Particle

MAPP

MoEDAL Apparatus for Penetrating Particles

MC

Magnetic Charge

mCP

mini-Charged particles

MDM

Magnetic Dipole Moment

MM

Magnetic Monopole

MMT

Magnetic Monopole Trapper

MoEDAL

Monopoles and Exotics Detector at the LHC

NLLP

Neutral Long-Lived Particle

NTD

Nuclear Track Detector

PMT

Photomultiplier Tube

SiPM

Silicon Photomultiplier

SM

Standard Model

SUSY

Supersymmetry

TOE

Theory of Everything

QFT

Quantum Field Theory

QM

Quantum Mechanics

Summary

The Monopole & Exotics Detector at the Large Hadron Collider (MoEDAL) is an experiment that looks for physics beyond the Standard Model. The MoEDAL main detector is primarily designed to search for magnetic monopoles and other highly ionizing particles produced from high-energy collisions at the LHC. The MoEDAL Apparatus for Penetrating Particles (MAPP) is a subdetector of the MoEDAL experiment. MAPP is designed to detect mini-charged particles, fractionally-charged particles, and long-lived neutral particles, and the detector itself can be divided into two parts: MAPP-1, designed to detect mini-charged particles and highly-ionizing processes, and MAPP-2, aimed at detecting decay products of long-lived particles. In particular, MAPP-1 could possibly detect heavy neutrinos through the energy loss of their permanent electric dipole moment. Part of the identification of particles at MAPP is done via the reconstruction of decay vertices. This thesis is divided into three main parts: 1) the construction and testing of the main elements of the MAPP-1 detector, 2) the development and evaluation of of the algorithm to be used at MAPP-2 for the reconstruction of decay vertices of long-lived particles; and lastly, 3) the consideration of the energy loss of an EDM in the detector.

Chapter 1

Introduction

1.1 Beyond the Standard Model

The Standard Model (SM) of particle physics describes the behavior of all known elementary particles and their interactions. It includes three generations of matter particles (quarks and leptons), and bosons, which transmit the fundamental forces between these particles. The last piece of the SM puzzle was the Higgs boson, which was discovered at CERN in 2012 [1, 2] and is responsible for giving particles mass. The strong force is mediated by eight gluons, the weak force is mediated by the W and Z bosons, and the electromagnetic force is mediated by the photon. The Standard Model predicts the behavior of these particles with great accuracy and has been confirmed through numerous experiments.

However, the SM has its limitations. It fails to predict the masses of the quarks and leptons, for instance, and of several other parameters, about twenty free parameters, which have to be determined by experiments [3]. It also provides no explanation for neutrino masses, and it cannot explain the extreme imbalance between matter and antimatter in the Universe. It does not account for the observed dark matter and dark energy in the universe, and it does not incorporate the theory of gravity, which is described by General Relativity. Thus, it is clear that there must be a deeper more fundamental theory underlying the SM. The search for physics Beyond the SM (BSM) is the key motivation behind the work presented in this thesis.

1.2 The MoEDAL-MAPP Project

In 2010, the Monopole and Exotics Detector at the LHC (MoEDAL) was approved as the seventh experiment at the LHC [4], and started its first tests in 2011 [5]. It officially started collecting data in 2015 [6]. MoEDAL's main purpose is to search

for Highly Ionizing Partilces (HIPs) such as the Magnetic Monopole (MM), dyons, Q-balls, strangelets and charged black-hole remnants. During the LHC's Run-1 and Run-2, MoEDAL placed the world's best limits of MMs [7], and the first-ever limits on dyons [6] and MMs produced via the Schwinger mechanism [8].

The addition of MAPP to the MoEDAL experiment was approved by CERN in 2021, to take data during LHC's Run-3, which starts in 2022. The Phase-1 MAPP detector (MAPP-1) is dedicated to expanding the search for mini-charged particles (mCPs) and other feebly interaction particles, such as particles with an anomalously large Electric Dipole Moment (EDM). MAPP-1 is also sensitive to charged and neutral Long-Lived Particles (LLPs). Phase-2 of the MoEDAL-MAPP project will see the installation of the MAPP-2 detector for data taking at the High Luminosity LHC in 2029. MAPP-2 is designed to greatly enhance the ability of MoEDAL-MAPP to detect neutral LLPs. It is currently planned that MAPP-2 will collect data during the LHC's Run-4, starting in 2029. A summary of the MoEDAL-MAPP project is given in Figure 1.1.

The MoEDAL Apparatus for Penetrating Particles (MAPP) is designed to expand the physics reach of the MoEDAL detector, dedicated to the search for Highly Ionizing Particle (HIPs) avatars of new physics, to include the search for Feebly Interacting Particles (FIPs), such as mini-Charged Particles (mCPs), Charged Long-Lived Particles (CLLPs), and Neutral Long-Lived Particles (NLLPs).

1.2.1 MoEDAL

MoEDAL stands out from other collider experiments in that it is the first dedicated search detector, a new class of detector at colliders. MoEDAL is also unique among the LHC detectors in the sense that it is a passive detector. It has the capacity to capture particles for further analysis and to collect permanent records of HIP tracks [6]. This is achieved by using plastic nuclear track detectors (NTDs) and trapping subdetectors (MMTs) [6]. A Geant4 description of the MoEDAL detector is given in Figure 1.2

MoEDAL is designed to search for HIP avatars of BSM physics. Its physics program [6, 8] defines over 34 scenarios with potentially revolutionary insight into foundational questions, involving: magnetic charge, a fourth lepton generation, heavy neutrinos, extra dimensions, new symmetries, and dark matter. To date, MoEDAL has placed the world's best limits on the existence of singly and multiply charge MMs [9, 10, 11, 12, 13, 14] and Highly Electrically Charged Objects (HECOs) [15]. It has also carried out the first-ever searches for 1) Spin-1 MMs [10]; 2) dyons [16], particles with electric and magnetic charge; and 3) MMs produced in heavy ion collisions via the Schwinger Mechanism [17, 18] (published in Nature). Additionally, it has published the LHC's only search for MM production via photon fusion [11].

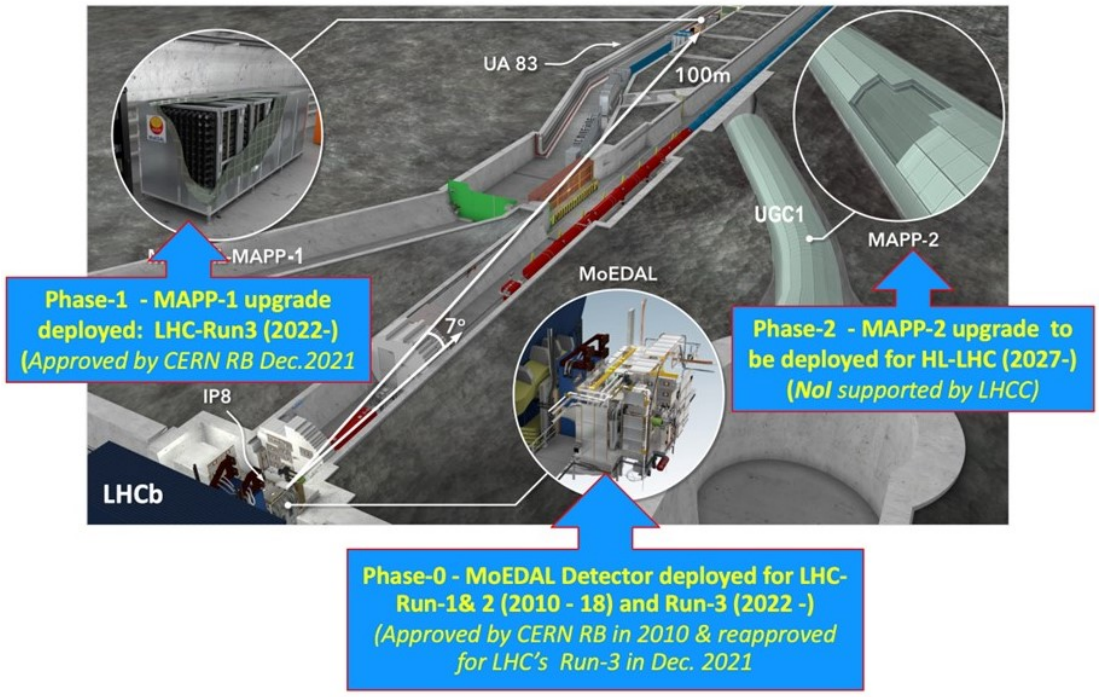

Figure 1.1: Summary of the MoEDAL-MAPP project as located a the LHC. MoEDAL is located around LHCb, in the Intersection Point 8 (IP8). MAPP-1 is located approximately 100 m away from MoEDAL, in the UA 83 gallery. MAPP-2 is located approximately 40 m away from MoEDAL within the UGC1 tunnel.

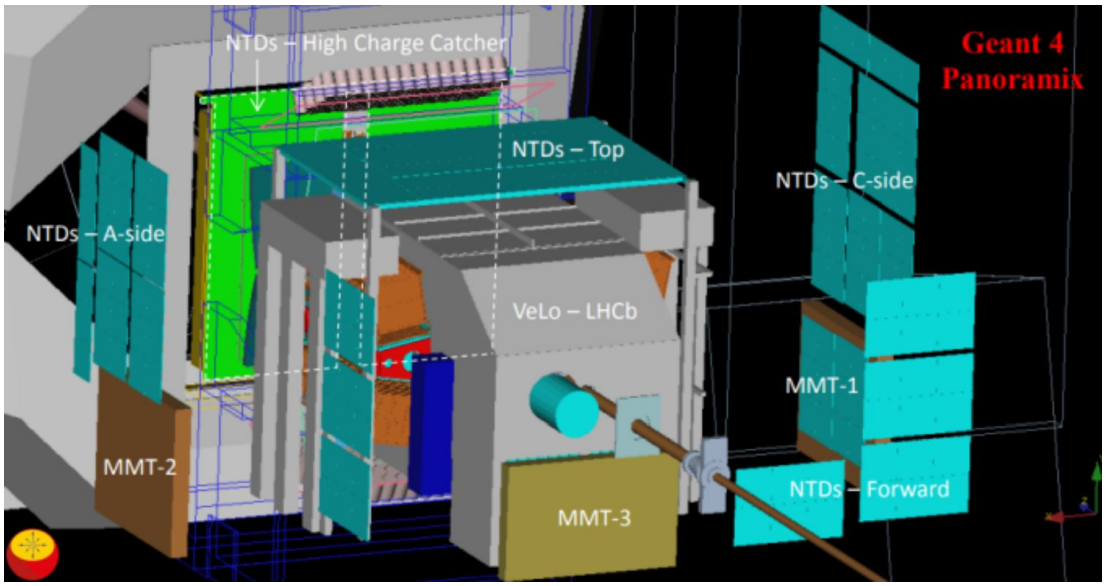

Figure 1.2: Geant4 simulation of the MoEDAL detector surrounding LHCb. The detection of HIPs is achieved passively via Nuclear Track Detectors (NTDs) and Magnetic Monopole Trappers (MMTs). Taken from [6].

MoEDAL is complementary to the General Purpose Detectors (GPDs), ATLAS, and CMS. The GPDs are not optimized for HIPs. However, MoEDAL is specifically designed to maximize its sensitivity to HIPs, thus limits obtained using the MoEDAL detector surpass other current experiments.

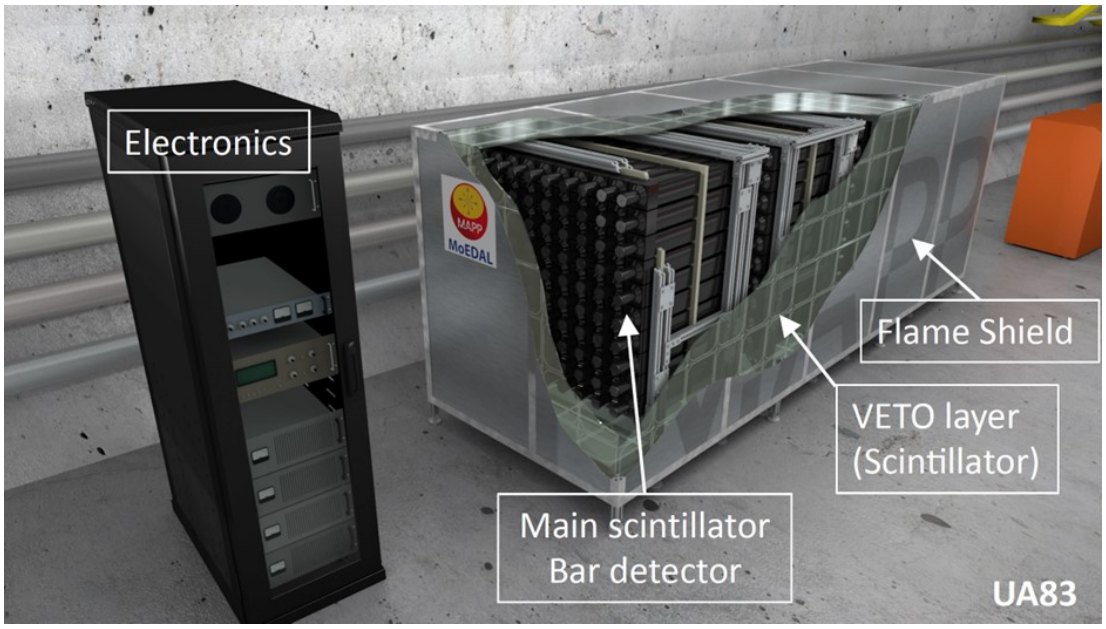

Figure 1.3: An illustration of the MAPP-1 detector. MAPP-1 has four sections, each having 10 × 10 scintillator, each 75 cm long, making a total cross-sectional area of 1 m × 1 m. 3.1-inch PMT readouts are attached to one end of the bars. The bars are supported by high-density polyethylene (HDPE) matrices, and the structure is held together with aluminum T-bars. A veto layer encases the detector, to know whether a particle came from the outside or a decay occurred within the detector. Finally, a flame shield, for safety, wraps the complete detector.

1.2.2 MAPP-1

The new MAPP-1 detector is a state of the art scintillator detector designed to search for FIPs, such as: mCPs, with charge as small as one thousandth the electron charge, and heavy neutrinos with an anomalously large EDM. Unlike MoEDAL, MAPP is an active detector with electronic-readout and software/firmware trigger. MAPP also has sensitivity to charged and neutral LLPs. The MAPP detector represents a "Phase-1" addition to the MoEDAL program for Run-3. The MAPP upgrade has effectively created a new MoEDAL-MAPP experiment at the LHC, affording an enhanced complementary expansion of the LHC's discovery horizon by providing sensitivity to an increased number of BSM physics scenarios involving

HIPs, FIPs, and LLPs, for which the main LHC experiments are not optimized. An illustration of the MAPP-1 detector is shown in Figure 1.3.

Example of MAPP-1 Physics Scenarios

Neutrinos and Heavy Neutrinos

The original assumption that neutrinos were massless was debunked in the 1990s by the Super-Kamiokande experiment [19], which observed flavour-changing atmospheric neutrinos, due to neutrino oscillations. Such neutrino oscillations require neutrinos to have mass. When considering neutrino oscillations, the "flavour" neutrinos are linear combinations of different mass eigenstates [20], and as the neutrinos propagated in space, the quantum mechanical phases of the three mass states would advance at slightly different rates due to the slight differences in their corresponding masses [21].

Neutrinos interact with matter as flavour eigenstates ($\nu_e,\ \nu_\mu,\ \nu_\tau$), but propagate as eigenstates of the free-particle Hamiltonian ($\nu_1,\ \nu_2,\ \nu_3$) [3]. The Maki-Nakagawa-Sakata-Pontecorvo (MNSP) matrix relates these two types of eigenstates by

$$\begin{pmatrix} \nu_e \\ \nu_\mu \\ \nu_\tau \end{pmatrix} = \begin{pmatrix} U_{e1} & U_{e2} & U_{e3} \\ U_{\mu 1} & U_{\mu 2} & U_{\mu 3} \\ U_{\tau 1} & U_{\tau 2} & U_{\tau 3} \end{pmatrix} \begin{pmatrix} \nu_1 \\ \nu_2 \\ \nu_3 \end{pmatrix}, \tag{1.1}$$

where U is the mixing matrix, which can be expressed in terms of mixing angles and a phase factor [3], which in turn allows for the expression of the neutrinos produced at the sun, with an initial electron flavour, to be expressed as

$$|\nu_e\rangle = \cos(\theta_{12})\cos(\theta_{13})\,|\nu_1\rangle + \sin(\theta_{12})\cos(\theta_{13})\,|\nu_2\rangle + \sin(\theta_{13})e^{-i\delta}\,|\nu_3\rangle\,. \tag{1.2}$$

In reality, the oscillation process itself is enhanced by the Mikheyev-Smirnov-Wolfenstein (MSW) effect [20]; this is a small correction, and goes beyond the purpose of this section. The key point here is that neutrinos are not massless particles, although their actual masses are yet undetermined.

In addition, the existence of a very heavy neutrino would require a new leptonic generation. However, the Z° has a lifetime consistent with the three generations of light neutrinos (2.9841 ± 0.0083) [22, 3]. A mass of 45 GeV or more would not affect the lifetime of the Z° boson.

Nevertheless, the Higgs data rule out the addition of a fourth leptonic generation [23, 24], making the discovery of heavy neutrinos non-trivial. The solution to this problem is proposed by a model by Ishiwa and Wise, which suggests that a fourth generation of leptons would leave most of the decays of the Higgs unscathed, except by the $H \to \gamma\gamma, \gamma Z,$ and gg modes [23, 25]. These modes could be induced by gauge

boson and heavy-fermion loops, and if the heavy neutrino is light enough, then the Higgs boson would be allowed to decay into particles not currently predicted by the SM [23, 25]. Furthermore, the existence of heavy neutrinos would require parity violation. MoEDAL will carry out a search for evidence of a fourth generation using the MAPP detector.

Electric and magnetic dipole moments (EDMs and MDMs, respectively) may reflect the flavour structure of the lepton model [23], so measurements of these moments could give important information on physics BSM. This is expected to happen as even electrically neutral objects, such as neutrinos, may have EDMs and MDMs. In Chapter 5, arguments are provided to show that a moving electric dipole induces a magnetic dipole. The MAPP detector attempts to find EDMs, and if one were to encounter enourmous EDMs, in comparison to the known limits, reasonable models could explain this with the existence of a fourth lepton generation, or a generation of heavy leptons [26, 23].

MAPP proposes to obtain information on the existence of a fourth lepton generation via the detection of a large EDM [23]. An equation for the energy loss expected from the process of an EDM going through the detector's material is derived.

The detection of the heavy neutrinos by MAPP would occur through ionization processes caused by an anomalously large EDM of the neutrino. MoEDAL estimates that a heavy neutrino's EDM might lead to the production of 100 photons through ionization loss in scintillating material. Preliminary propositions assume that 10^4 photons are produced per MeV energy deposited in the scintillator [27].

Mini-charged Particles

Mini-charged particles (mCPs) are hypothetical non-SM particles that have charges that are a fraction of the known charge of the electron e. MoEDAL is studying mini-charged particles that are generated in a "model-independent" scenario [28, 29] in which a new masless $U'(1)$ Abelian gauge field and a dark photon, A'_μ, couple to $B^{\mu\nu}$, a SM hyper-charge gauge field [28]. In addition, one adds, from Dark Quantum Electrodynamics (Dark QCD), a massive dark fermion, ψ_{mCP}, which has a mini-charged mass, m_{mCP}, that couples to the dark photon gauge field, A'_μ, charged with e'. Introducing an arbitrary parameter and a redefinition of the dark photon field to $A'_\mu \Rightarrow A'_\mu + \kappa B_\mu$, one obtains the interaction Lagrangian [28]:

$$\mathcal{L} = \mathcal{L}_{\mathcal{SM}} - \frac{1}{4} A'_{\mu\nu} A'^{\mu\nu} + i\bar{\psi}\left(\partial\!\!\!/ + ie'A\!\!\!/' - i\kappa e' B\!\!\!/ + im_{mCP}\right)\psi. \tag{1.3}$$

From this equation, the fractional charge, expressed in terms of electric charge, is given by $\epsilon = \kappa e' \cos\theta_W / e$ [28, 29].

MAPP expects to find mCPs produced in pairs through Drell-Yan mechanisms

in $p - p$ collisions at an center-of-mass (CM) energy of $\sqrt{s} = 14$ at the LHC [28]. See Figure 1.4.

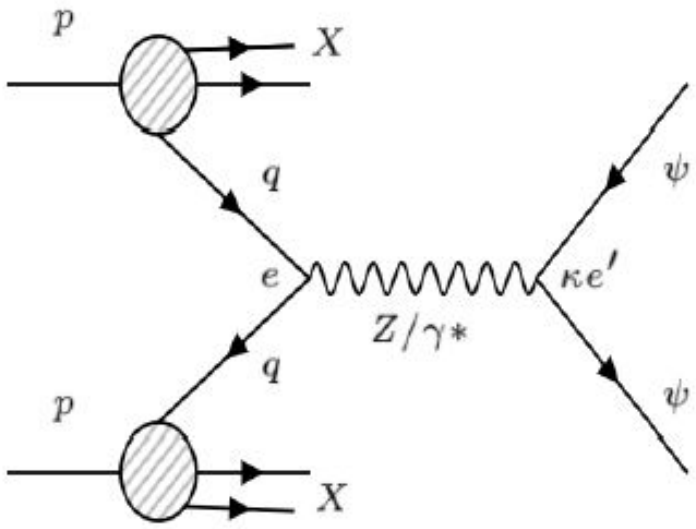

Figure 1.4: Feynman diagram for the Drell-Yan pair-production of mCPs via p-p collisions at the LHC. Taken from [28].

MAPP-1 is dedicated to the detection of these hypothetical particles (and also to HIPs). This thesis focuses on the technical part of MAPP-1, specifically on the evaluation of the performance of its components.

1.2.3 MAPP-2

The MAPP-2 detector is planned for HL-LHC. The MAPP-2 detector is essentially a monitored decay volume formed from the UGC1 gallery, a fiducial volume of some 1200 m^3. In order to achieve this, the UGC1 gallery is lined by three layers of 1.25 cm thick scintillator tiles of size ≈ 1 m^2 with embedded wavelength shifting (WLS) fibres - with a 1 cm pitch - on each face of the tile, arranged orthogonally to each other. WLS fibres are read out by Silicon Photomultipliers (SiPMs). Right now, we are studying the KETEK PM3225WB 3×3 mm^2 SiPM, which we are using to readout the MAPP-2 VETO tiles. Currently, we are planning to use the electronic readout and trigger for MAPP-2 that we developed for MAPP-1. A visual description of MAPP-2 is given in Figure 1.5.

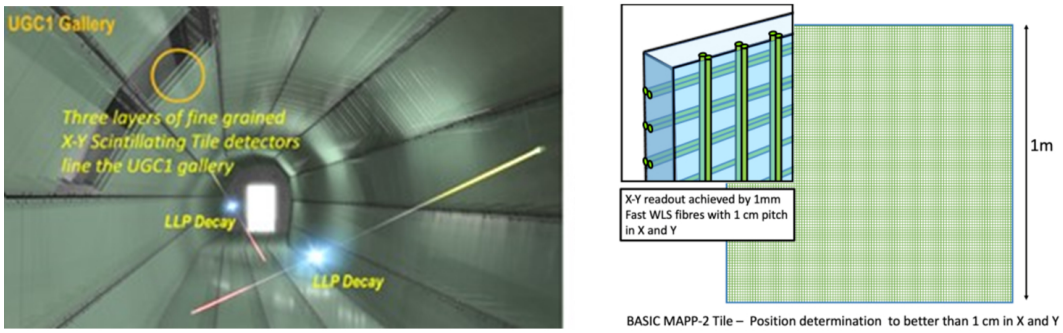

Figure 1.5: A visual description of the MAPP-2 detector.

Example of MAPP-2 Physics Scenarios

Long-Lived Particles

Long-lived particles (LLPs) in the SM are relegated to particles with small masses, 5 GeV [30]. The more massive particles are not stable enough and have shorter lifetimes in the SM. There are several theories that motivate the search for LLPs that include physics beyond the SM. Some include Supersymmetry (SUSY) considerations to the SM and some others consider the dark sector at and below the weak scale, for example [30]. Some of the limitations in current experiments in detecting LLPs are the insensitiveness to models that require one decay vertex within the detector, as is the case with ATLAS; inefficiency in the detection of LLPs in the lower mass spectrum, in CMS; and, as the case is for LHCb, there are limitations in its detection capacity by its geometry [30]. Thus the need for a detector thought for LLPs, such as MAPP-2.

Massive LLPs can occur in theories that go BSM, such as in SUSY [31]. In the SUSY scenario, MAPP-2 considers the gluino pair production from an original proton-proton collision; a gluino is then expected to decay into two quarks and a long-lived neutralino, $\tilde{\chi}_1^0$, a neutral LLP: $\tilde{g} \to q\bar{q}\tilde{\chi}_1^0$ [7]. Furthermore, it is also considered that the $\tilde{\chi}_1^0$ furhter decays into an stau and a tau lepton; the lifetime of the neutralino will depend on the mass splitting $\Delta m = m_{\tilde{\chi}_1^0} - m_{\tilde{\tau}_1} \lesssim m_\tau$, allowing a lifetime that varies from a nanosecond to a microsecond, approximately [7], which means that they can decay far from the proton-proton interaction point [30] well into the detector. This means that one way of determining the presence of LLPs is by looking at displaced SM particles within the detectors [30].

MAPP-2 is also sensitive to heavy neutral leptons, which arise on SM extensions that contain massive neutrinos [7]. In addition to the consideration of a fourth leptonic generation, the case of a gauged B-L model described in [32] is also taken into account. In this case, a new Abelian gauge field, B'_{mu}, is introduced into the

SM with three right-handed Majorana neutrinos and the Z' gauge boson. The new neutrinos could be produced from the decay of such boson, $Z' \to NN$. In turn, these neutrinos can decay as $N \to \mu^{\pm} q\bar{q}$ and $N \to \mu^{+}\mu^{-}\nu_{mu}$, products that can be detected by MAPP-2 [7].

Chapter 2

MAPP Overview

2.1 MAPP-1 - The Phase-1 MAPP Detector

The MoEDAL Apparatus for Penetrating Particles (MAPP) will be installed in two phases, as indicated in Figure 1.1 in Chapter 1. The MAPP-1 detector will be installed in the UA83 gallery for data taking during LHC's Run-3, which started in 2022. MAPP-1 is designed for the detection of FIPs such as mCPs from dark-sector models and heavy neutrinos with anomalously large EDM. MAPP-1 will also be capable of detecting neutral and charged LLP decays.

The MAPP detector is divided into four equal sections, as can be seen in Figure 2.1. Each section corresponds to a 10 $\times$ 10 array of 100 scintillator "units" that we shall refer to hereafter as "bars", each of size 10 cm $\times$ 10 cm $\times$ 75 cm, and each read out by a low noise 3.1-inch Photo-Multiplier Tube (PMT). The scintillator bars in each of the four sections of the MoEDAL-mCP detector are supported by three matrices machined out of high-density polyethylene (HDPE) plates. The scintillator bar sections constitute the main detector which is hermetically encased in a scintillator-tile veto layer. The MAPP detector and VETO layer are completely enclosed in an aluminium frame shield. The size of the shield is roughly 1.3 m $\times$ 1.5 m $\times$ 4 m. Installation of the MoEDAL detector started in December 2021.

2.1.1 Detector Location

MAPP's location in UA83, 100 m from Intersection Point 8 (IP8) at an angle of 7^o to the beam-line, was chosen to reduce the background from primary and secondary particles from the interaction point as much as possible, whilst maintaining an acceptable signal particle flux. Also, the position of the MAPP detector, roughly 110 m underground, severely reduces the backgrounds from cosmic rays [6]. Figure 2.2 indicates the various positions of the MoEDAL-MAPP detector with respect to IP8.

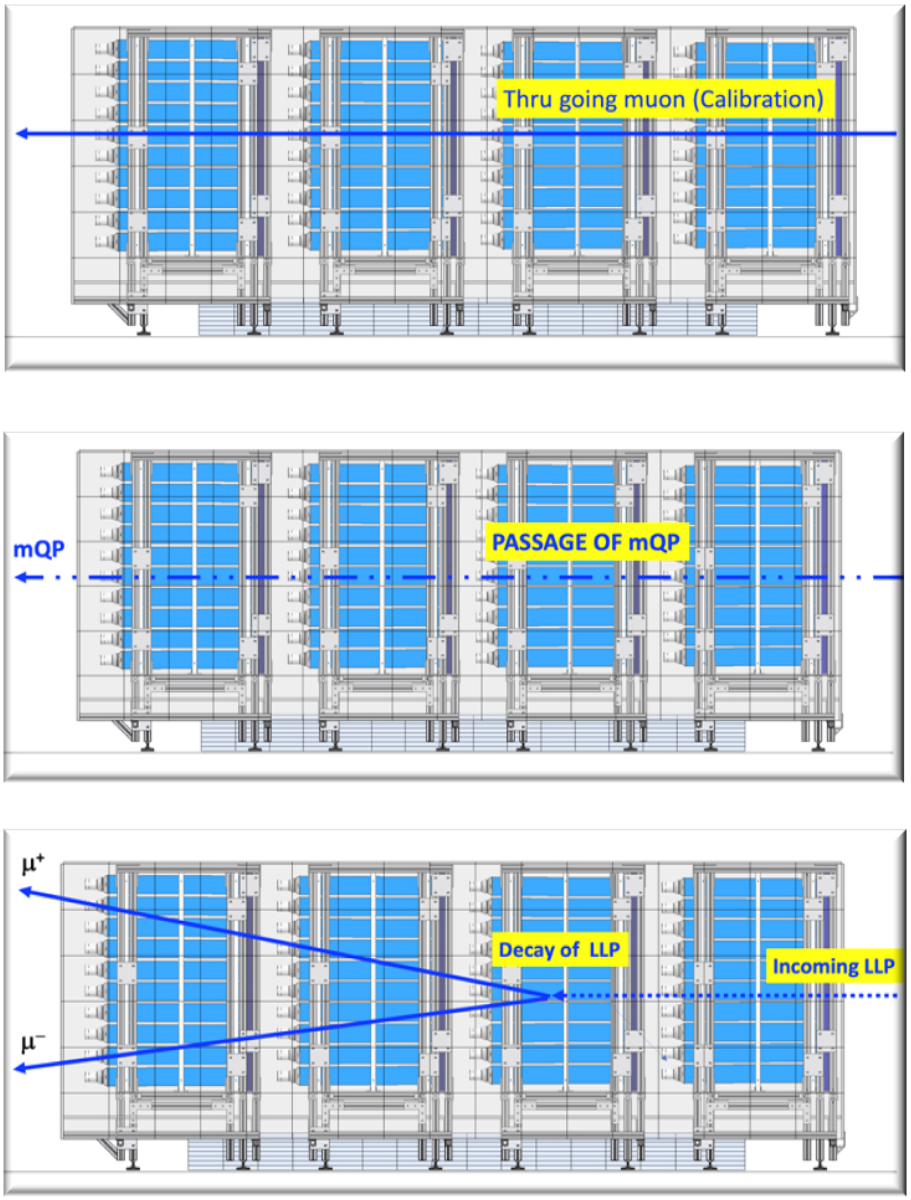

Figure 2.1: A side view of the MAPP detector for different detection scenarios: (ABOVE) a muon coming from IP8 as background noise triggers the veto. (MIDDLE) a mini-charged particle causes an ionization that goes as the square of a unit charged particle, hence the dotted line (an mCP with charge e/10 will cause 100th the ionization of a unit charge). (BELOW) a very long-lived neutral particle decays within the detector (the veto is not triggered, but an spontaneous vertex within the detector is present).

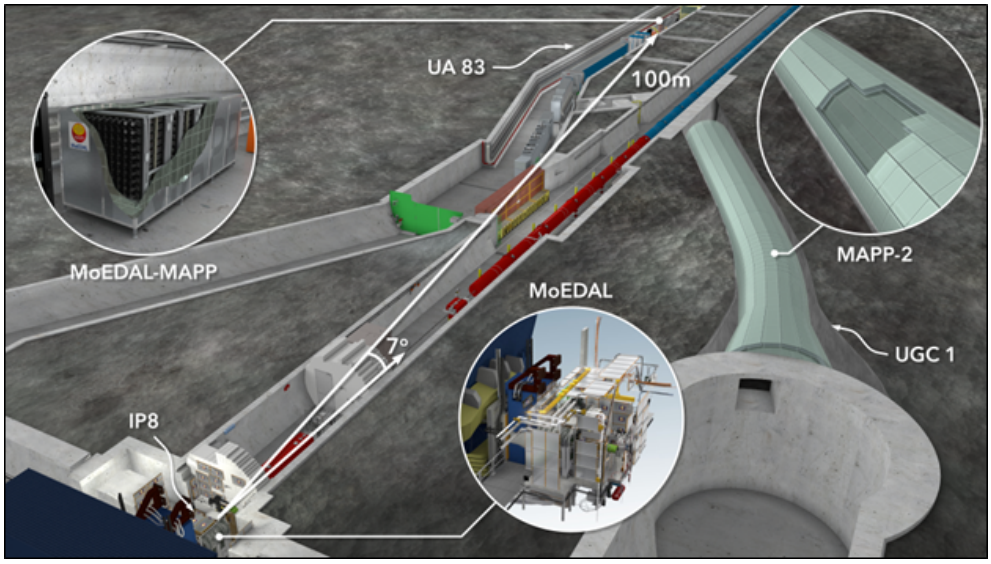

Figure 2.2: Location of the MAPP detector(s) at the LHC. MAPP is to be installed in the UA83 (Phase-1) and UGC1 (Phase-2) tunnels at the LHC, which is adjacent to the MoEDAL detector.

2.1.2 The Scintillator Elements of MAPP

The MAPP-1 Scintillator Bars and Light Guides

The compact central section of MAPP is dedicated to the search for mCPs. It is made up of four collinear sections, with cross-sectional area of roughly 1.0 m^2, each comprised of 200 $\times$ (5 cm $\times$ 10 cm) plastic scintillator bars, each 75 cm long. These bars are combined to form 100 $\times$ (10 cm $\times$ 10 cm) bars. A drawing of this basic sub-unit of the MAPP-mCP detector is shown in Figure 2.3. Each bar is read out by one low noise 3-inch PMT. The detector is arranged to point toward the IP8.

Thus, each through-going particles from the IP will encounter 3.0 m of scintillator and be registered by a coincidence of four PMTs. The 4-fold PMT coincidence essentially eliminates the background from "dark counts" in the PMTs. Additionally, the division of the detector into four bars virtually excludes all fake 4-fold coincidences due to radiogenic backgrounds in the scintillator and PMTs.

For MAPP-1 scintillator bars, we are utilizing a highly doped polystyrene scintillator with operating characteristics, essentially identical to fast high light output acrylic scintillators, but more cost effective. For the scintillator utilized in the MAPP-mCP detector, the light output of the standard composition of 0.6 % pTP (para-Terphenyl - primary fluor) and 0.05 % POPOP (secondary fluor) was improved by increading the doping to 2 % pTP, 0.05 % POPOP. This scintillator

ITEM NO.	PART NUMBER	WEIGHT (KG)	QTY.
1	Scintillator Body	7.73	1
2	PMT Cover	0.08	1
3	Light Guide	0.24	1
4	PMT	0.71	1

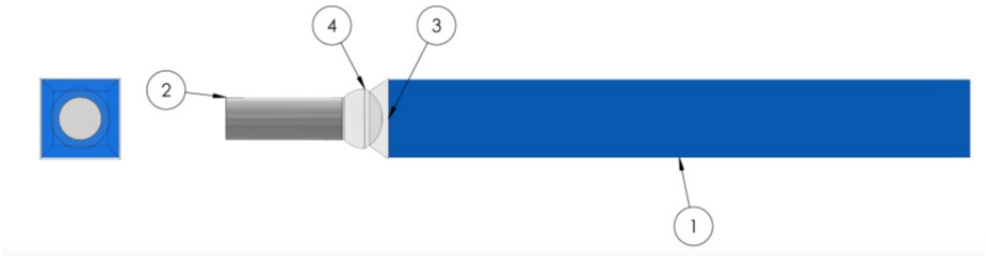

Figure 2.3: A drawing, to scale, of MAPP-1/mCP scintillator bar.

was developed by the MoEDAL group of the Czech Technical University and is now being manufactured by the Czech company, NUVIA a.s.

Scintillating materials are usually made of aromatic plastics or non-aromatic plastics that have an aromatic co-solvent; some of these materials include polystyrene (PS) and polyvinyltoluene (PVT) [33, 34]. In addition to the possibility of adding a co-solvent, these plastics are usually mixed with fluor and a spectrum shifter to calibrate the scintillating wavelength to the light spectrum at which the photodetectors to be used are most effective [33]. The basic process behind scintillation is that of de-localization of valence electrons from the plastic molecules upon being hit by incoming ionizing particles; this leads to fluorescence, which occurs from a transition from a spin singlet excited state to a singlet ground state of the valence electrons in the plastic [34].

The coupling between the scintillating material and the photo-detectors is achieved by the incorporation of light guides. The purpose of light guides is to direct as much light as possible from the scintillator bars into the PMT. For MAPP-1, Sylgard 184 sylicone is used for this purpose. The coupling between the PMT and the silicone is achieved by mechanical compression of the light guide (see Section 3.4.1). The flexible nature of the light-guide material allows a close air-gap-free junction between the scintillator and the light-guide as well as between the light-guide and the PMT.

In MAPP-2, the scintillation light is taken out of the scintillation tile walls of the detector via WLS fibres. The ends of these fibres are in contact with SiPMs, and the coupling is achieved by the application of optical gel/grease while the system is held in place via a mechanical connection that maintains a positive

contact between the fibre end and the SiPMs.

The VETO Scintillator-Tile System

The MAPP-mCP detector is completely surrounded by a scintillator veto system, shown in blue in the engineering drawing included in Figure 2.4. The MAPP-mCP detector is completely encased in a veto detector comprised of scintillator tiles of size 25 cm $\times$ 25 cm and thickness 1 cm. We will readout the tiles using two embedded wavelength shifting fibres (WLS) of diameter 1 mm readout by a SiPM (KETEK PM3225WB 3 $\times$ 3 mm^2), as shown in Figure 2.5. The prototype for testing is shown in Figure 2.6; abrupt angles are avoided in order to avoid light loss, and the two ends of the fibre meet to collect light from both from a single readout.

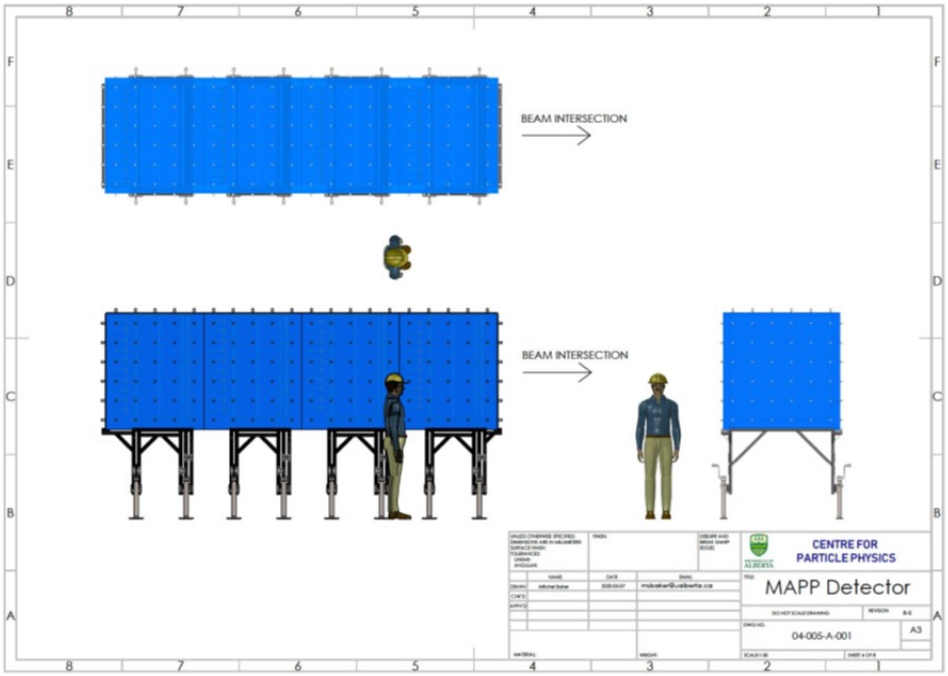

Figure 2.4: A design of the MAPP-1 veto system. The scintillator tile system is shown in blue.

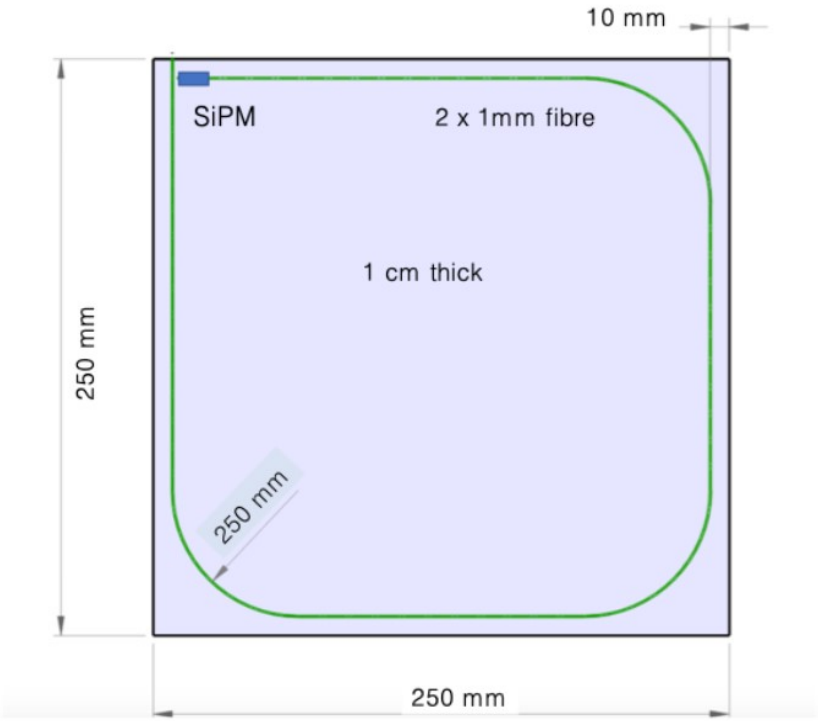

Figure 2.5: A scintillating tile basic element of the MAPP-1 veto system.

Figure 2.6: A scintillating tile prototype for testing.

According to the law of geometrical optics, light entering an optical fibre from outside the fibre must leave it. Thus, ordinary optical fibres cannot be used to collect light from scintillator plates. However, a WLS fibre containing a fluorescent material absorbs the higher frequency scintillation light from the scintillator and emits lower frequency photons. Some of these photons will be trapped in the fibre and can be transmitted to the end of the fibre by internal reflection at the fibre boundary with the lower refractive index cladding layer surrounding the core.

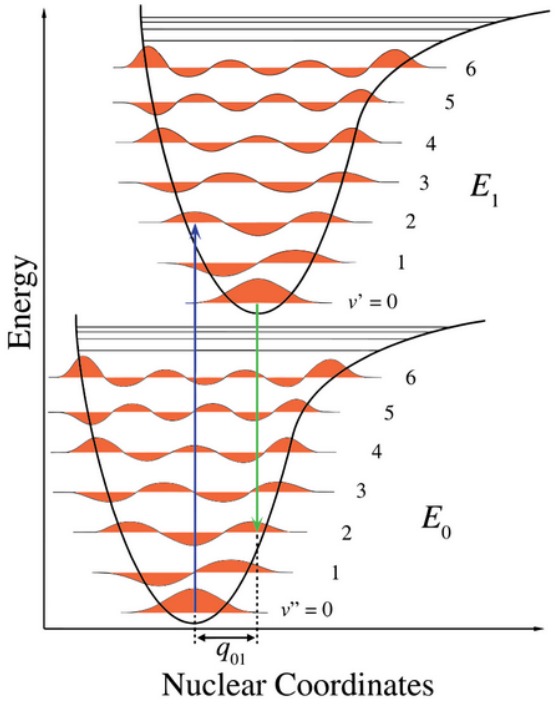

Figure 2.7: The Franck-Condon Principle of energy illustrated in a diagram. This can be summarized in three steps: 1) an absorption of a photon leads to a higher energy state of the system, 2) the fluorescence of the molecule leads to a lower energy state of the system, and 3) the shift in the nuclear coordinates caused by the photon absorption sets a new equilibrium position in the interaction potential. Taken from [35].

In more detail, when WLS fibres capture light, the excitation of their molecules leads to a new electronic configuration. The transition to this electronic configuration happens faster than the nuclei can respond, so that when the nuclei realign with respect to each other, according to the new electronic configuration, the vibrational energy of the molecule has been changed [35]. This will lead to the emission of photons that have a lower frequency than the one that was initially absorbed, as

shown in Figure 2.7. In the case of WLS fibres readout of scintillators, the small diameter of the fibers, typically around 1 mm in diameter, matches the typical size of the entry window of a SiPM. These SiPMs provide an efficient approach to light collection from WLS fibres.

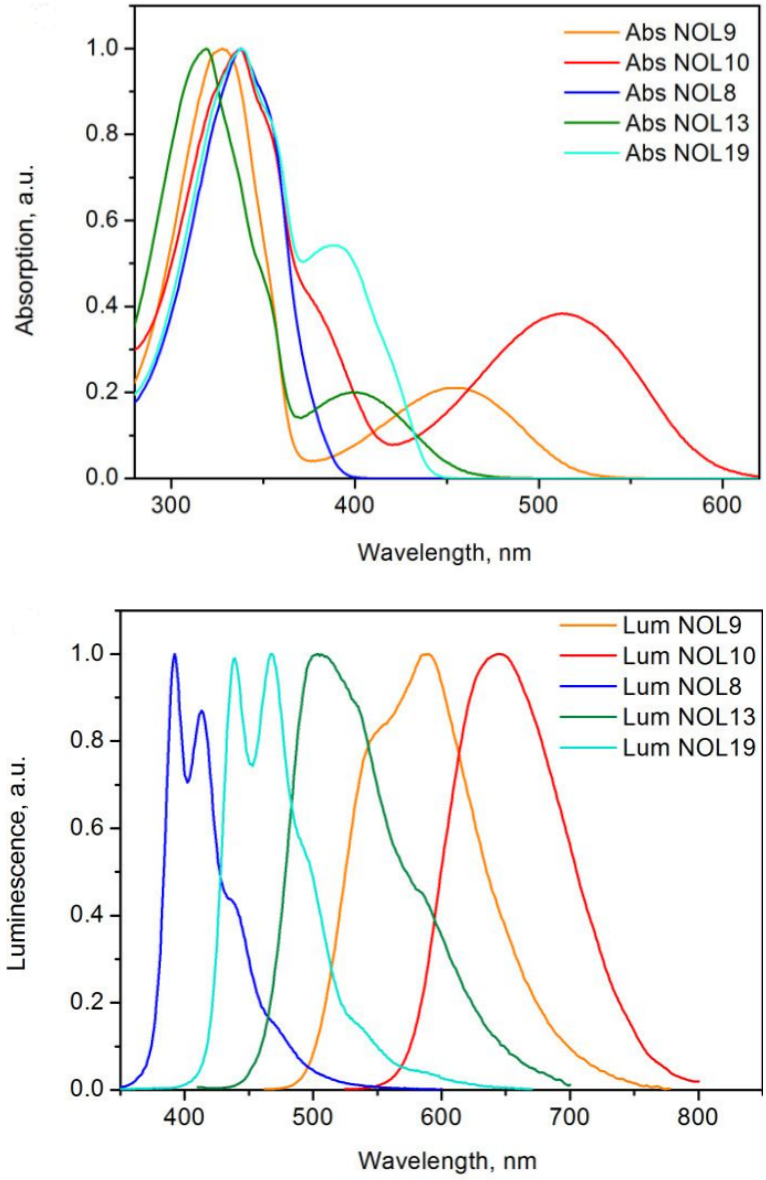

Figure 2.8: Absorption and emission/luminescence spectra for different nano-structured organosilicon luminosphores. This is a type of WLS fibre nano-fabricated to have specific absorption and emission spectra. Taken from [36].

In practice, the WLS fibre "colour" is matched to the photo-detection method employed. For SiPMs, this colour would be "green". The emission/absorption spectra for different WLS "colours" are shown in Figure 2.8.

The MAPP-1 Scintillator Calibration System

In order to check the operation of the MAPP-mCP detector, we will be installing an LED calibration system. A blue emitting LED will be inserted at the end of each "non-PMT" end of the 400 × 0.75 m scintillator bars comprising the MAPP-mCP detector. The LED pulser control/power box allows each, or all, of the LEDs embedded to be pulsed with a 15 ns pulse with a voltage that can be varied by the pulser system. This allows the simulation of either the light expected from a standard minimum ionizing particle or an mCP.

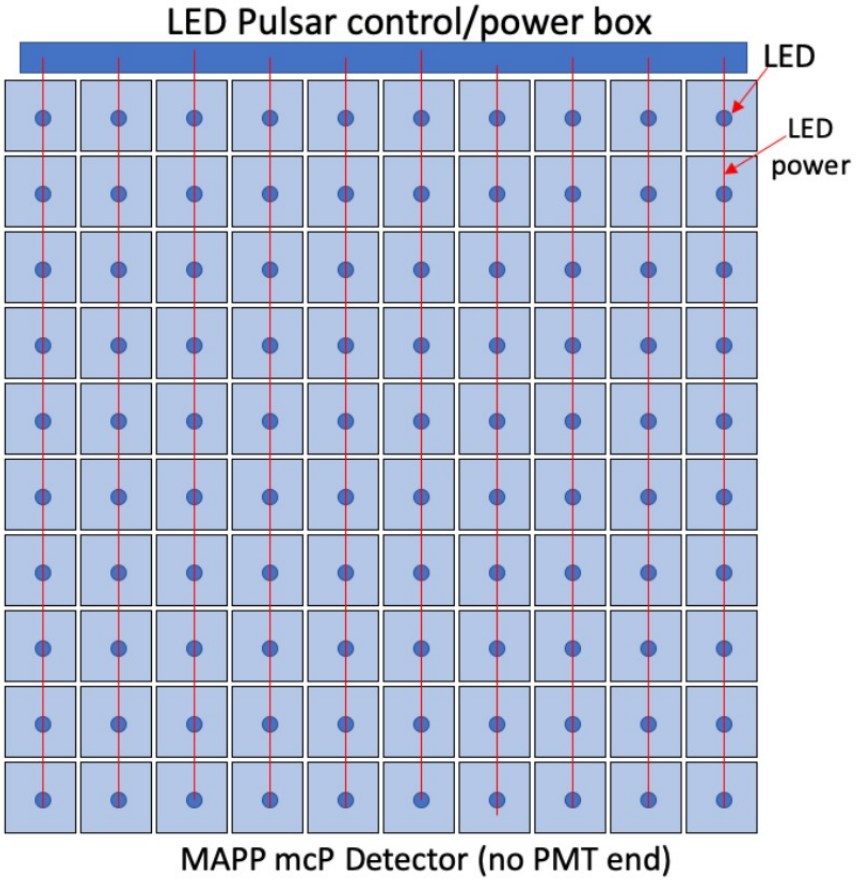

Figure 2.9: A schematic view of the MAPP-mCP pulser system.

A total of four LED pulser control calibration boxes will be required. These units

are produced in-house based on previous experience building the LED calibration system for the ATLAS LUCID detector. A sketch of the calibration system unit is shown in Figure 2.9.

2.1.3 The PMT and VETO Tile Readout

Photo-Multiplier Tubes (PMTs) are photosensitive devices used in experimental physics for the detection of particles through their production of scintillation or Cerenkov light. A PMT consists of a photo-cathode that converts incoming photons into electrons that then enter an electron multiplier region consisting of a series of dynodes, whose function is to multiply the electron signal produced at the cathode. Finally, we have the anode that serves as an electron collector, providing the output signal of the PMT [37]. See Figure 2.10 for an internal diagram of a typical PMT. All these components are held in a vacuum envelope in order to preserve the photo-cathode and avoid the noise that would be generated by electron interactions with the gas in the vessel. Figure 2.11 shows a photograph of a PMT used in the MAPP detector. Figure 2.12 shows its specifications.

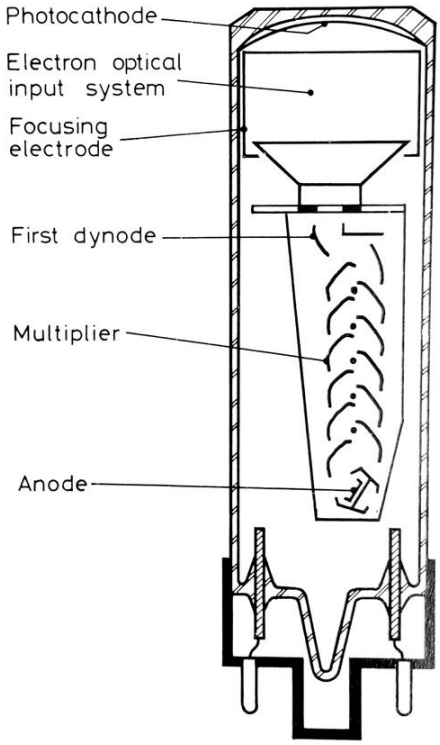

Figure 2.10: Cross-section of a typical head-on type PMT. MAPP uses head-on types PMTs. Taken from [38].

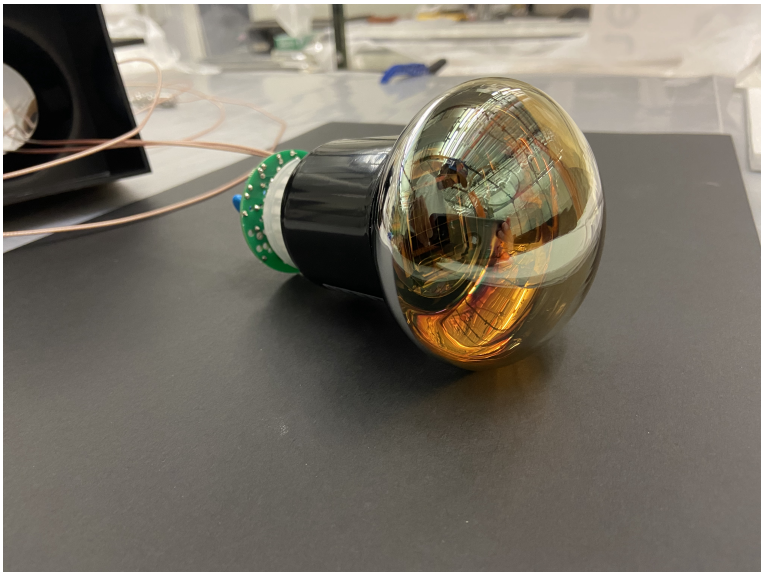

Figure 2.11: Head-on type PMT used in MAPP's main section.

Some of the main sources of noise in a PMT arise from the anode's dark current, which is a current that flows through the PMT internal system even when no light falls on the PMT photo-cathode. The dark current mainly originates from thermal electron emissions at the photo-cathode and at the dynodes. It is the main factor in determining the lower limit of light detection [37]. Among the methods that can be used to reduce the effects of dark current in the particle detection process is to place the PMTs in coincidence and to leave the PMTs in the dark previous to their use (typically 48 hours is enough). Furthermore, reducing the temperature at which the PMTs are operated to further reduce the dark current/pulses.

It is necessary to determine the voltage at which the PMT has to be operated. At values below this high voltage, one loses photo-detection signals, and at values above this voltage the noise becomes dominant over real photo-detection signals. The testing of MAPP's PMTs is a part of this thesis. The testing procedure and results are given in Chapter 3.

HZC Photonics ZP72B20 PMTs are used in MAPP-1. In this design, the photo-cathode will be at ground potential with positive high voltage applied to the anode. The signal will be capacitively coupled to the cable. The HV power supply will consist of a boost converter to convert from 48 V DC to 250 V using a coupled inductor to reduce the maximum voltage seen by the controller. Several stages of a Cockcroft-Walton multiplier will then increase this up to 2000 V. Power, signal, and control will be delivered via the same cable to reduce cabling costs. In this way, we avoid HV cables and connectors as the related safety concerns.

A block diagram of the electronic readout and the powering scheme is shown

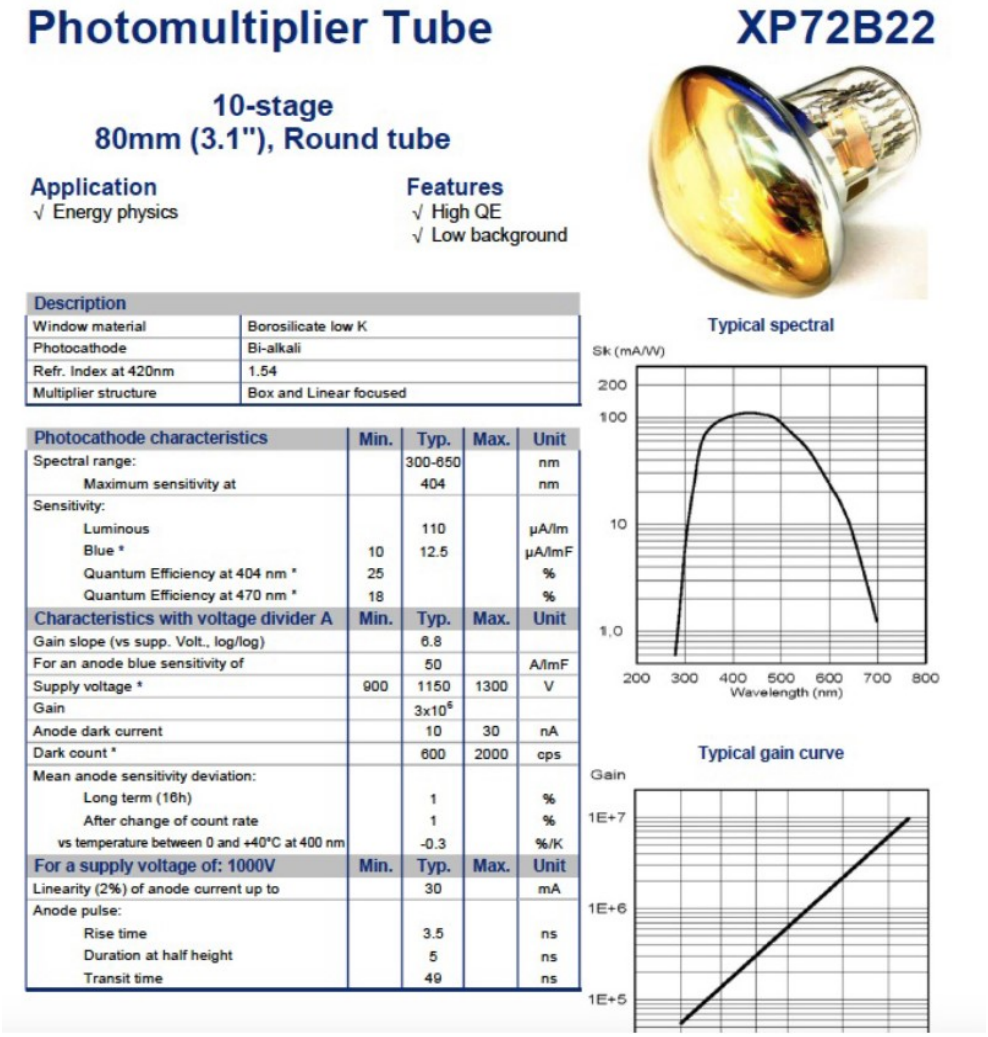

Photomultiplier Tube XP72B22

10-stage
80mm (3.1"), Round tube

Application
√ Energy physics

Features
√ High QE
√ Low background

Description	
Window material	Borosilicate low K
Photocathode	Bi-alkali
Refr. Index at 420nm	1.54
Multiplier structure	Box and Linear focused

Photocathode characteristics	Min.	Typ.	Max.	Unit
Spectral range:		300-650		nm
Maximum sensitivity at		404		nm
Sensitivity:				
Luminous		110		µA/lm
Blue *	10	12.5		µA/lmF
Quantum Efficiency at 404 nm *	25			%
Quantum Efficiency at 470 nm *	18			%
Characteristics with voltage divider A	**Min.**	**Typ.**	**Max.**	**Unit**
Gain slope (vs supp. Volt., log/log)		6.8		
For an anode blue sensitivity of		50		A/lmF
Supply voltage *	900	1150	1300	V
Gain		$3x10^6$		
Anode dark current		10	30	nA
Dark count *		600	2000	cps
Mean anode sensitivity deviation:				
Long term (16h)		1		%
After change of count rate		1		%
vs temperature between 0 and +40°C at 400 nm		-0.3		%/K
For a supply voltage of: 1000V	**Min.**	**Typ.**	**Max.**	**Unit**
Linearity (2%) of anode current up to		30		mA
Anode pulse:				
Rise time		3.5		ns
Duration at half height		5		ns
Transit time		49		ns

Figure 2.12: Specifications of the PMTs used in MAPP-1. From HZC Photonics.

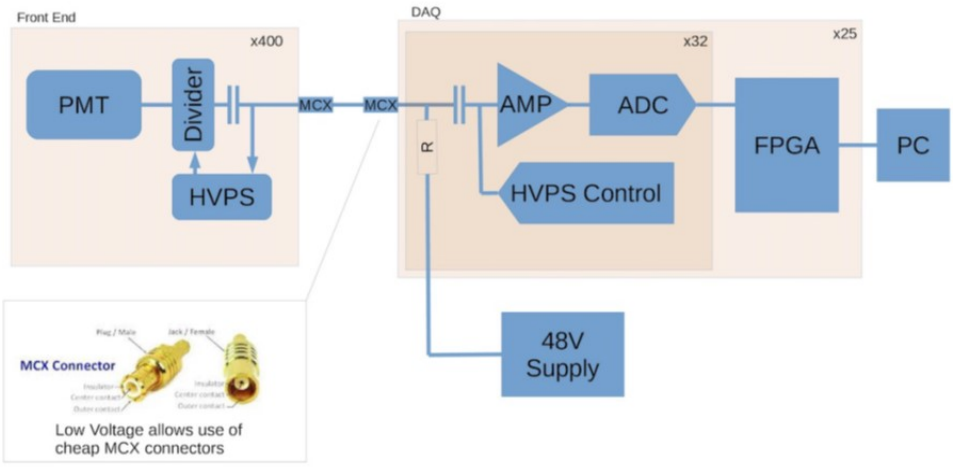

Figure 2.13: A block diagram showing the basic electronics readout structure for the MAPP-mCP detector.

in Figure 2.13. Each Data Acquisition (DAQ) board will consist of 32 identical channels. The DAQ will connect to the front end via an MCX connector. A bias tee will couple the 48 V DC supply to the signal line. Control signals for the high-voltage power supply will also be coupled capacitively to the signal line. The amplifier chain will include a programmable gain amplifier to allow tuning of the overall system gain, minimal shaping, and an anti-alias filter. The ADC will consist of a Texas Instruments ADS4249 dual channel amplifier running at 240 MHz and 14-bit readout to an Intel (formally Altera) Cyclone IV FPGA via LVDS.

The FPGA will perform discrimination, coincidence, and peak detection of the incoming signals, with inter-FPGA communication via back-plane B-LVDS. Events that pass both the software trigger and the veto will be passed for storage via Ethernet to the PC(s). The system will run synchronously to the LHC (bunch crossing) clock. The orbit clock will also veto background events from non-colliding bunches.

2.2 MAPP-2 - The Phase-2 MAPP Detector

MAPP-2 will be installed for data taking on HL-LHC that is expected to start in 2029. MAPP-2 is essentially a large monitored decay volume. It is dedicated to the improvement of MoEDAL-MAPP's sensitivity to neutral LLPs.

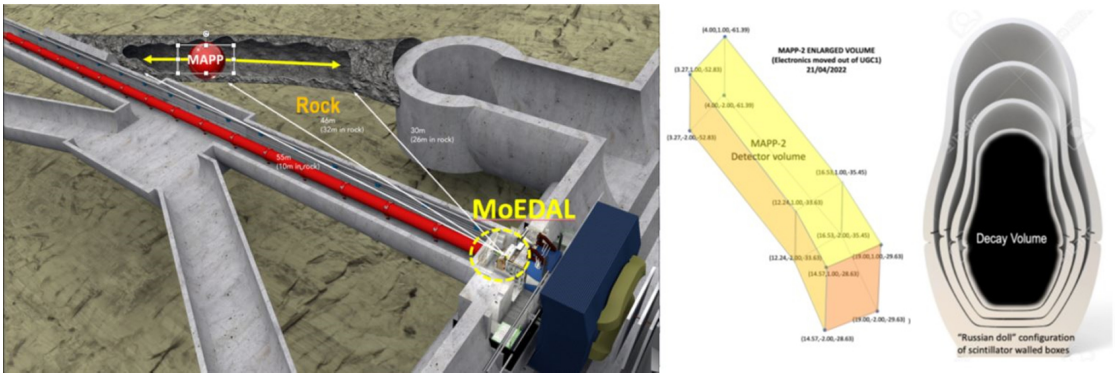

Figure 2.14: (LEFT) A graphic of the deployment of the MAPP-2 detector in the UGC1 gallery. (MIDDLE) the fiducial volume of the MAPP-2 detector. (RIGHT) The "Russian Doll" layout of the nested scintillator walls comprising the MAPP-2 detector.

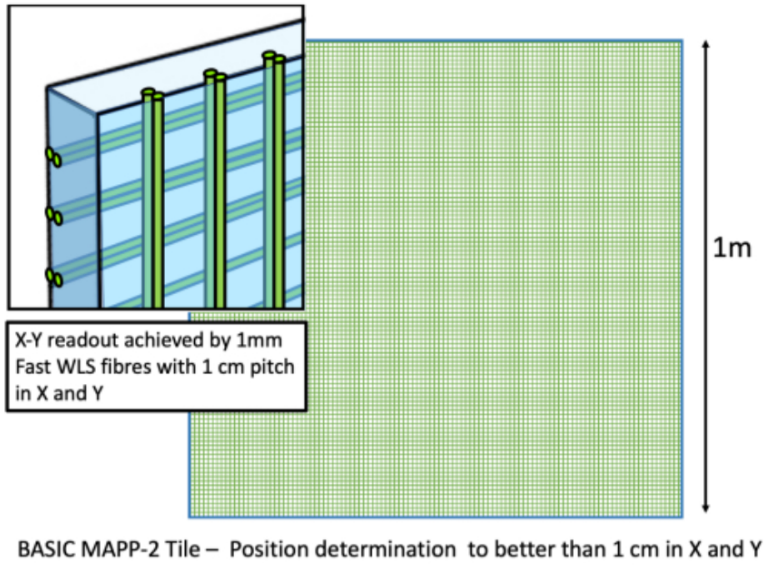

Figure 2.15: Basic diagram of the scintillator sheets, of which MAPP-2 is constructed, with embedded WLS fibres. Taken from [7].

The MAPP-2 detector is essentially a monitored decay volume formed from the UGC1 gallery, a fiducial volume of some 1200 m^3, as shown in Figure 2.14 (left and middle). In order to achieve this, the UGC1 gallery is lined by three layers of 1.25 cm thick scintillator tiles of size $\approx$ 1 m^2 with embedded WLS fibres - with a 1 cm pitch - on each face of the tile, arranged orthogonally to each other. The whole

arrangement is shown in Figure 2.15. The WLS fibres are readout by SiPMs. At this time, we are studying the KETEK PM3225WB 3 $\times$ 3 mm^2 SiPM, which we are using to readout the MAPP-2 VETO tiles. Currently, we are planning to use the electronic readout and trigger for MAPP-2 that we developed for MAPP-1.

2.2.1 Detector Location

As with MAPP-1, MAPP-2's location severely reduces the background from primary and secondary particles from the interaction point. Its location, 110 m underground, severely reduces the backgrounds from cosmic rays [6]. Figure 2.2 shows the location of MAPP-2 in the UGC1 gallery. This tunnel will be lined with three layers of scintillating sheets in a "Russian Doll" configuration, taking advantage of the entirety of the tunnel as well as its geometry and allowing the measurement of decay vertices.

2.2.2 MAPP-2's Silicon Photo-Multiplier Readout

Silicon photo-multipliers (SiPMs) are made of high-purity p- or n-type silicon with highly doped p- or n-type contacts on opposite surfaces [39]. In this application, MAPP is using Ketek PM3315-WB SiPMs (Figure 2.16), which have the advantage of being ideal for WLS fibre readout and cost-effective compared to regular PMTs. The SiPMs' photo-detection efficiency is the highest in the blue-green region, as seen in Figure 2.17, and it is if 30 % operated at 5 V at room temperature, as seen in Figures 2.17 & 2.18 The active area of the SiPMs MAPP is planning to use is 3 x 3 mm^2. The ends of the optical fibres would be in direct contact with these areas. In addition to being more economic, SiPMs have also an advantage over PMTs in that they have a higher quantum efficiency, they required a lower power consumption (compare a PMT requiring 1200 V, as an estimate, for operation versus a 5 V SiPM), they are also unaffected by the presence of external magnetic fields, and, although they are solid state devices, their relatively small sizes allows them to have a time response comparable to regular PMTs [39].

Figures 2.19 & 2.20 show a SiPM used in MAPP. A special encasing for holding the optical fibres and the SiPMs in contact was built for the testing of noise reduction of the photo-multipliers; see Figures 2.21 & 2.22. By putting SiPMs in coincidence one can lower the threshold at which noise is eliminated from the readout, as shown in Figure 2.23. The results indicate that MAPP could use two to four SiPMs in coincidence per WLS end.

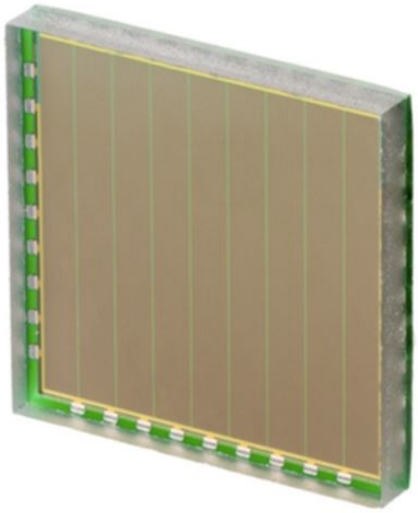

Figure 2.16: Ketek PM3315-WB SiPM. Taken from [40].

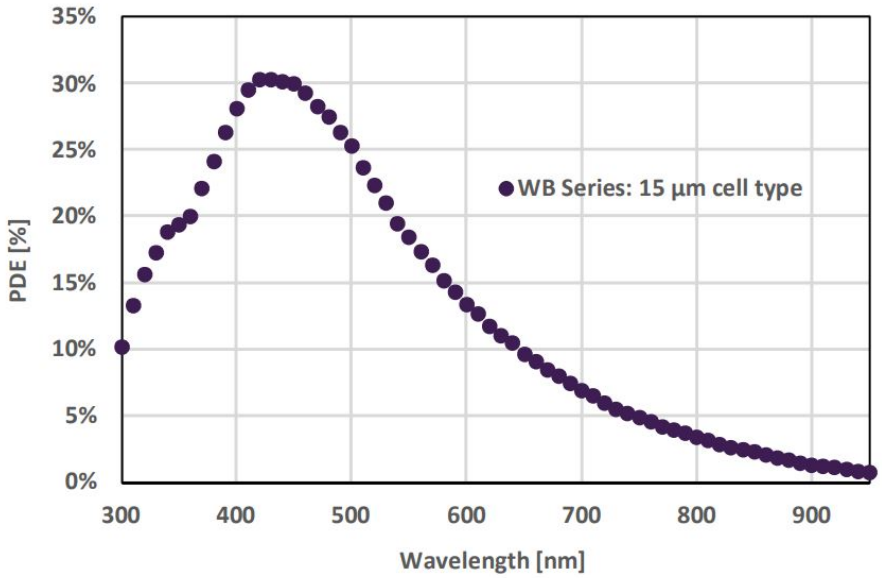

Figure 2.17: Photo-detection efficiency at 5 V over voltage (see Figure 2.18) of a Ketek PM3315-WB to be used in the detector. The SiPM is more efficient in the green 400-500 nm wavelength spectrum. Taken from [40].

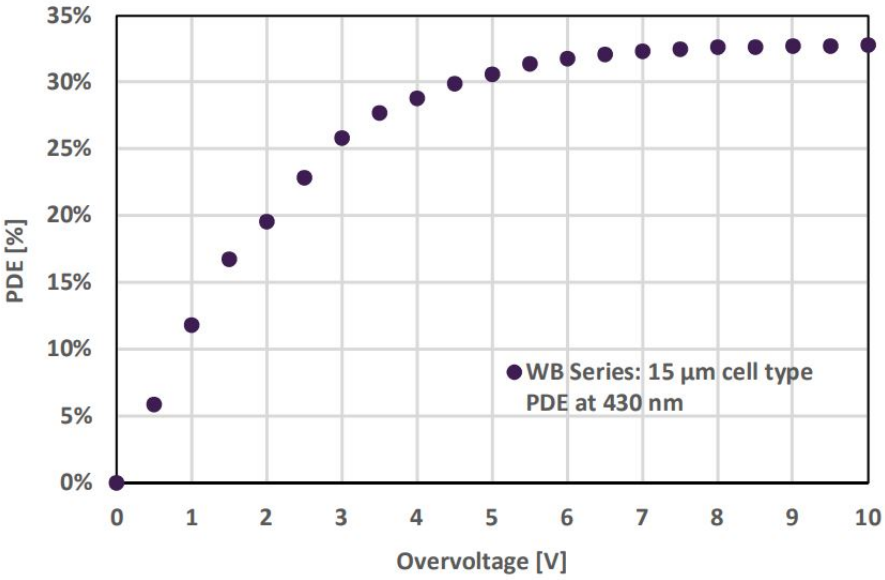

Figure 2.18: Photo-detection efficiency vs overvoltage at 21 °C of a Ketek PM3315-WB SiPM. Taken from [40].

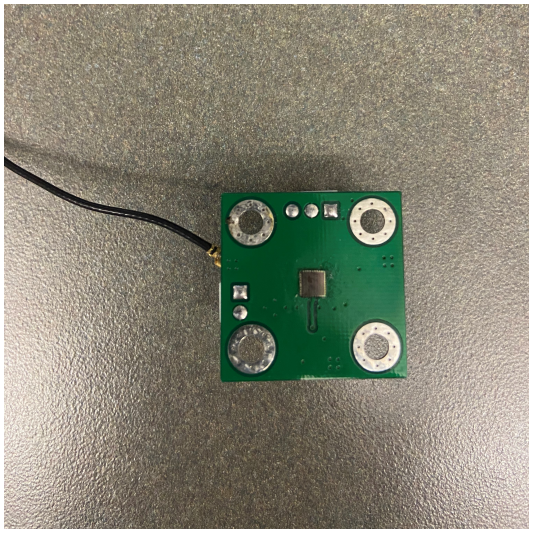

Figure 2.19: SiPM to be used in MAPP (small grey square).

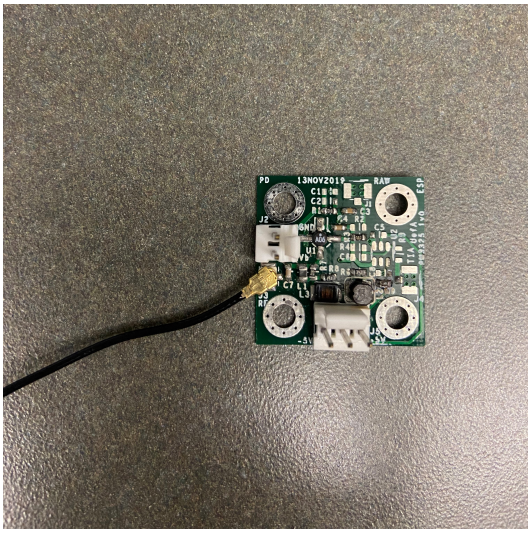

Figure 2.20: Electronic board driving the SiPM in (a).

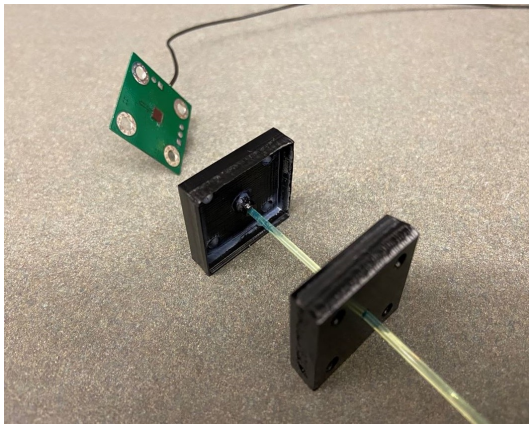

Figure 2.21: SiPM and optical fibre encasing with a two-piece Delrin plastic design.

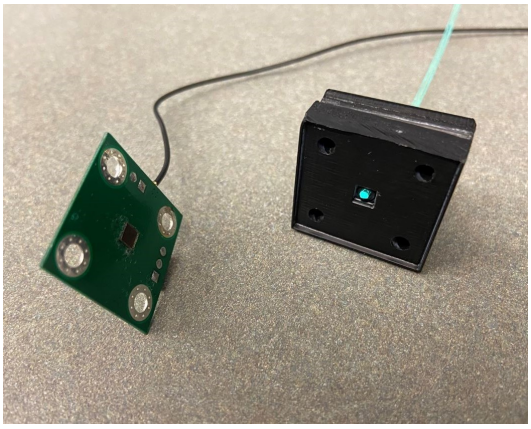

Figure 2.22: The SiPM and the optical fibre are held in place through screws that go through the SiPMs electronic board's and the two-piece Delrin encasing's holes.

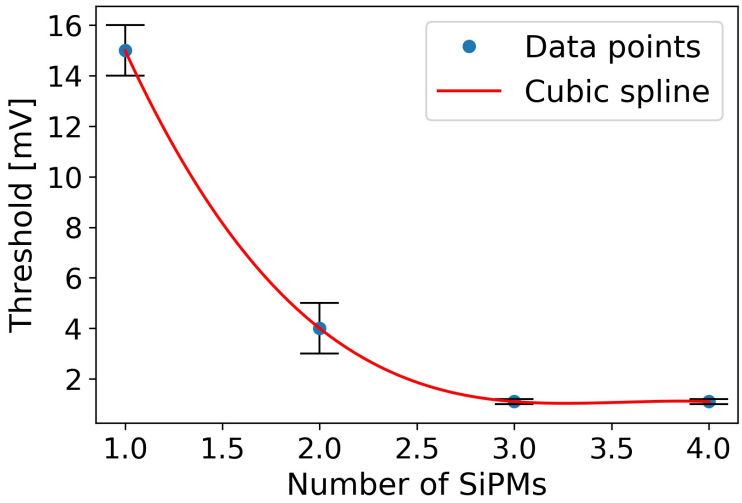

Figure 2.23: Threshold at which the noise from the SiPMs is killed per number of SiPMs put in coincidence. Taken from [41].

2.2.3 The Test Volume Used for Tracking Studies

For the purposes of testing the vertexing and tracking algorithms we consider a test volume three nested boxes, as shown in Figure 2.24. The inner box (A) has the dimensions 3 m × 3 m × 3 m. The other two external boxes have increased dimensions for 30 cm (B) and 60 cm (C), respectively. The particles that enter the box do it through one side of the box. The veto wall is located, in relation to the walls of the boxes, as shown in Figure 2.25.

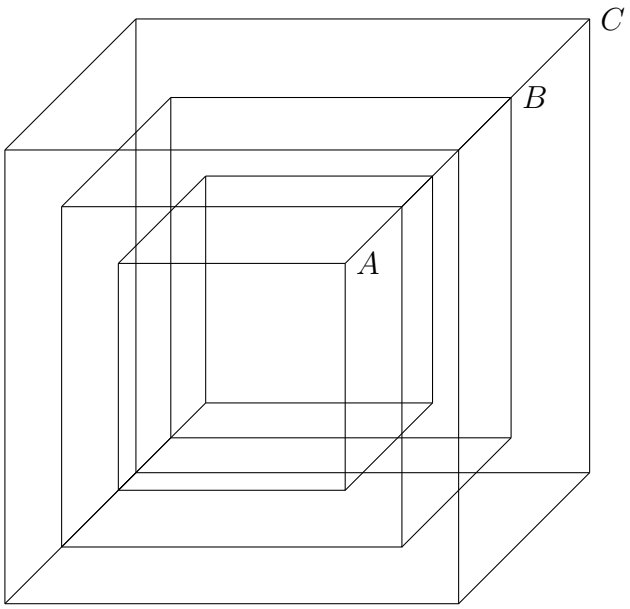

Figure 2.24: Russian doll box model. Not to scale. A cross section showing the veto wall and the dimensions of the boxes is shown in Figure 2.25.

As indicated in Figures 2.15 & 2.26, the large scintillator tiles (roughly 1 m × 1 m × 1.3 cm) making up the MAPP-2 detector walls have two orthogonal sets of embedded fibres, one set on each side, allowing an "X-Y" position to be determined. The experimental information that MAPP-2 looks to provide regarding detected particles is the reconstruction of their vertices, and this grid provides a good method to obtain the vertex at which particles decay via decay track reconstruction. Only those particles with a well-reconstructed vertex, according to the "chi-square" of the fit, are retained in the study.

The Python code generates a decay vertex within the decay volume, from which it creates two decay tracks from it. The points at which these tracks intersect with the walls of the boxes are registered in the computer program. A detailed description of the tracking and vertexing algorithms and their effect is given in Chapter 4.

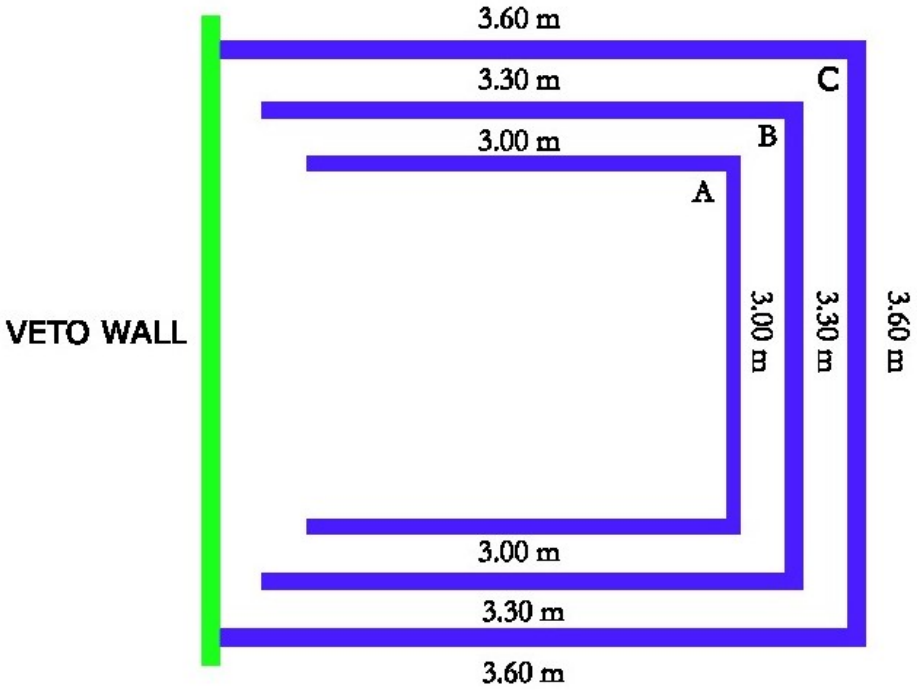

Figure 2.25: Three-box setup showing veto and dimensions.

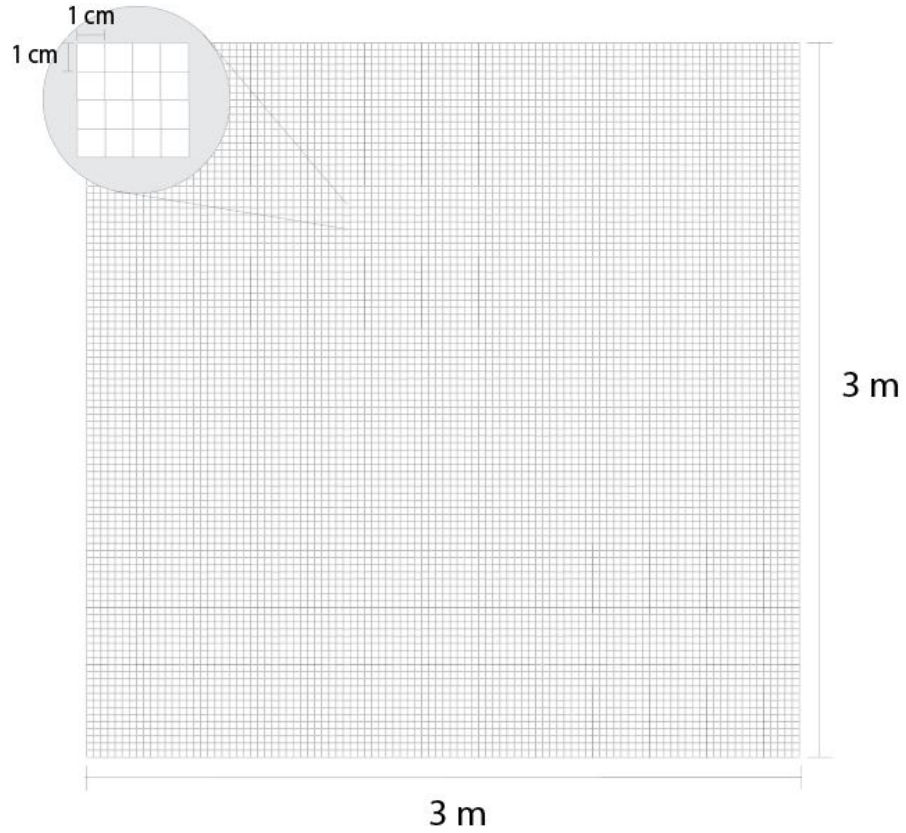

Figure 2.26: Effective 1 cm × 1 cm scintillating grid created by the two sheets of scintillating material with optical fibres embedded in them. The sheets are placed one behind the other at right angles with respect to the orientation of their optical fibers. Taken from [41].

Chapter 3

MAPP-mCP Construction

The 800 scintillator bars used in MAPP-1 are made of polyvinyl-toluene. Two bars, each 75 cm long with a cross-section of 5 cm $\times$ 5 cm, constitute a "unit" in the assembled detector. So effectively, we have bars 75 cm long with a cross-section of 10 cm $\times$ 10 cm. See Figure 3.1 for photographs of the plastic scintillators exposed to black/UV light. The preparation of the bars for installation in UA83 is reported in detail in this chapter.

Each of the 400 scintillators "units" is read out by a low noise 3.1" HZC Photonics PMT. The PMT is joined to the bar using a moulded silicon rubber light guide and held in place by a special plastic housing. A calibration LED is connected to one bar of each scintillator "unit". The design, fabrication and placement of these items, is described below. Lastly, the testing and "plateauing" of the PMTs used for the readout of MAPP is also recounted in this chapter.

3.1 Polishing and Wrapping Scintillator Bars

A small number of the scintillator bars have surface imperfections such as scratches and gouge marks. In order to minimize light loss arising from such defects the affected bars were polished to give a mirror-smooth surface. The polishing process required a few steps. First, a compound of organic liquid/aluminum oxide/water mixture polisher heavy scratch remover (sold under the name Novus #3) was utilized. Second, a compound of aqueous silica/hydrocarbon mixture fine scratch remover (sold under the name Novus #2) was used. Third, the bars were washed with distilled water (see Figures 3.2 & 3.3). For the polishing process, anti-lint wipes and a polishing machine were used.

The next step was to create a single scintillator bar "unit" from two individual scintillator bars. In order to do this, two bars were individually tightly wrapped with sheets made of high-density polyethylene fibres (sold under the name Tyvek)

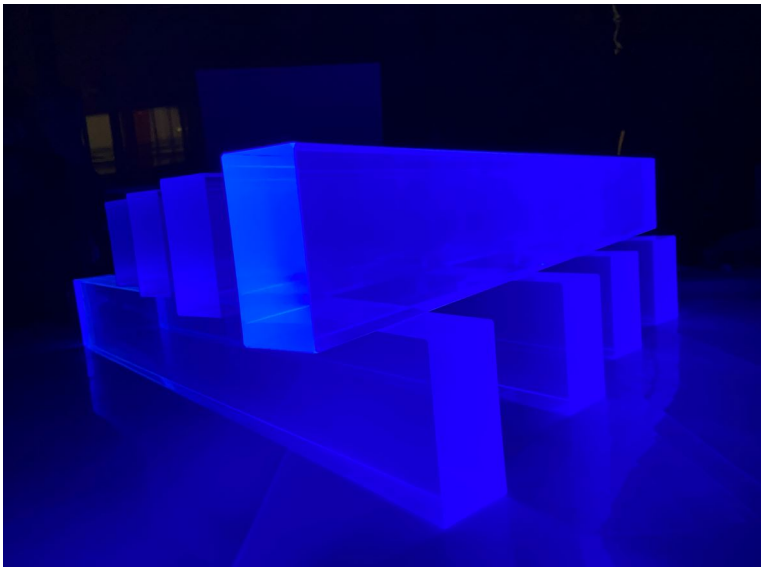

Figure 3.1: Scintillator bars exposed to UV light.

leaving about a quarter of a centimeter without wrapping at the ends of the bars (these are wrapped later on after the addition of light guides). See Figures 3.4 & 3.5.

The individual wrapped bars were then paired up. The side where the Tyvek overlaps was left facing the outside with respect to the surfaces of the individual bars put into contact; see Figure 3.6. The reason for the individual wrapping is to isolate one bar from the other so that we can, in the future, read out the individual bars if a finer granularity of detection is required.

We then pair two bars with a final layer of Tyvek, tightly held in its place by clear tape, as shown in Figure 3.7. Finally, one end of the paired scintillator bars was wrapped in a single layer of Tyvek.

The paired bars in the second layer of Tyvek were then wrapped in black paper, as part of the light exclusion wrapping of the bars, as shown in Figure 3.8. Care was taken to ensure that the black paper was NEVER in contact with the scintillator bar, to avoid light emitted within the scintillator bar being absorbed by the paper.

To provide light tightness of the scintillating environment, the paired bars wrapped in black paper were covered with (fire-proof) black tape, as shown in Figure 3.9. The black tape was overlapped by 50 % to ensure that the pairs were wrapped in, effectively, two layers of tape. It was also made sure that the tape never came into contact with the bare surface of the scintillator bar, in order to avoid degradation of the scintillating material by the deposition of the sticky component of the tape on the plastic. Finally, the end wrapped in Tyvek was covered with an effective double layer of black tape as depicted in Figure 3.10.

Figure 3.2: Plastic polishers used on the scintillator bars.

Figure 3.3: Distilled water for washing the scintillator bars.

Figure 3.4: Scintillator bar wrapped in the first layer of Tyvek.

Figure 3.5: The distance between the bar's end and the end of the first Tyvek layer is of about half a centimeter.

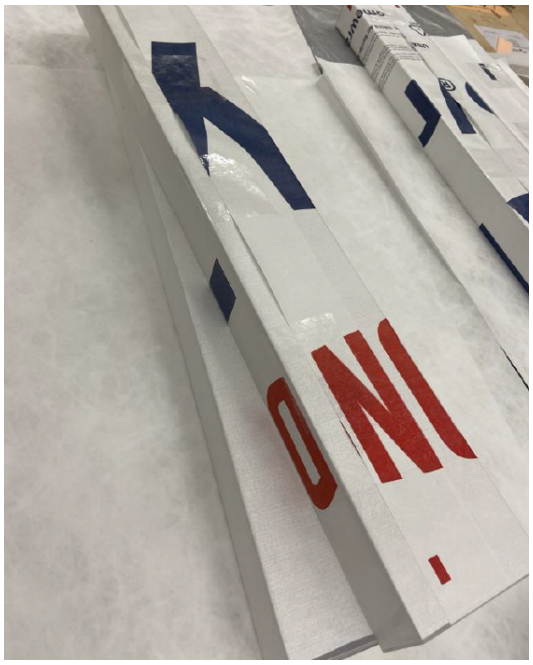

Figure 3.6: The overlapping layers of Tyvek are facing outwards.

Figure 3.7: Paired scintillator bars (already wrapped in a first layer of Tyvek) wrapped in a second layer of Tyvek.

Figure 3.8: Paired bars (previously wrapped in a second Tyvek layer) wrapped in black paper.

Figure 3.9: Paired scintillator bars wrapped in an effective double layer of black tape.

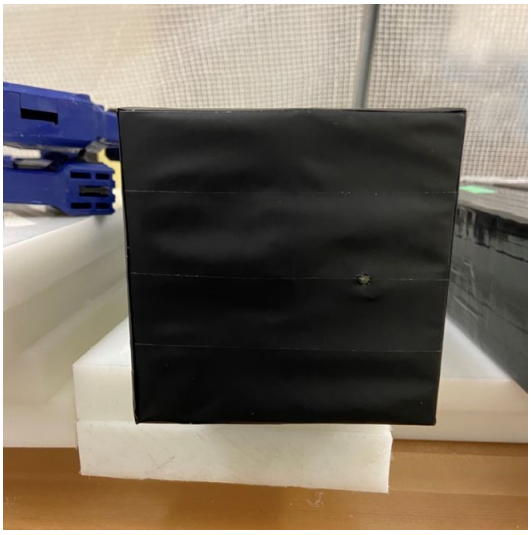

Figure 3.10: End of a fully wrapped sctintillator pair.

3.2 Installing the LED Calibration System

A mold was 3D printed to guide the drilling of the wrapped end of the paired scintillator bars. These holes are required to install the LEDs. See Figure 3.11. Only one hole of the 3D-printed mold was used to drill the bars. The mold itself was placed in such a way that the drilling happened right at the center one of the paired bars (so only one of the paired bars was drilled). See Figures 3.12. A 1/8-inch drill bit was used and it was dug into the scintillator bar to a distance of 0.75 inches deep (counting the thickness of the mold). Any remain of plastic dust in the drilled hole was removed with a sharp tool and pressurized air.

Figure 3.11: 3D-printed mold used to drill holes at one end of the scintillator units.

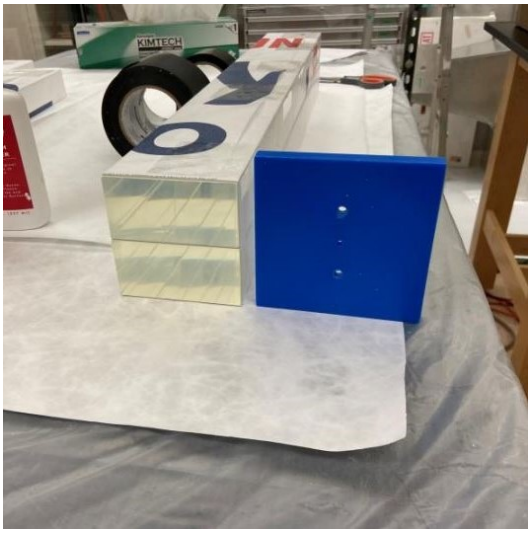

Figure 3.12: Drilling mold aligned with the bar to be drilled.

The reason for this hole is the future attachment of an LED at the end of the "unit" of paired bars. This is to simulate the detection of a particle and testing of the performance of the scintillating material. See Figures 3.13 & 3.14 for an image seeing through the bare end of otherwise wrapped scintillator bars with an LED attached to the end of the scintillator unit. The LEDs are attached to the scintillator bar with optical epoxy (this fills in any scratching left in the plastic from the drilling). The preparation of the optical epoxy is achieved with a 28:100 ratio of optical cement and optical resin, respectively.

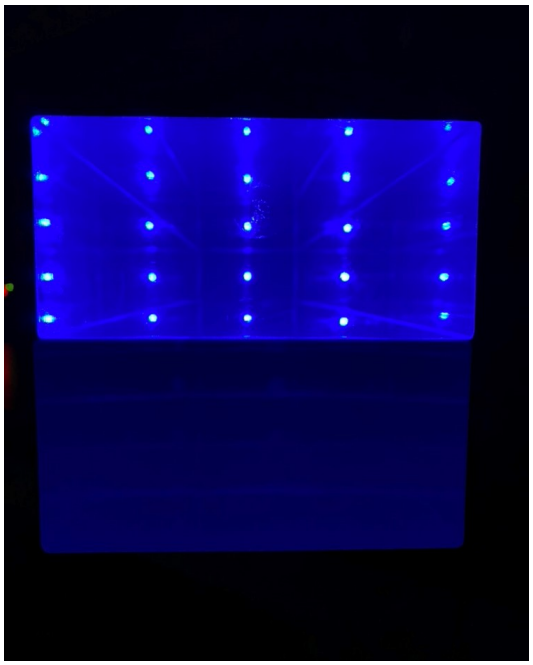

Figure 3.13: View of the end of an array of scintillating bars connected to the LED calibration system. The blue point of light arise from the individual LEDs used in the calibration system.

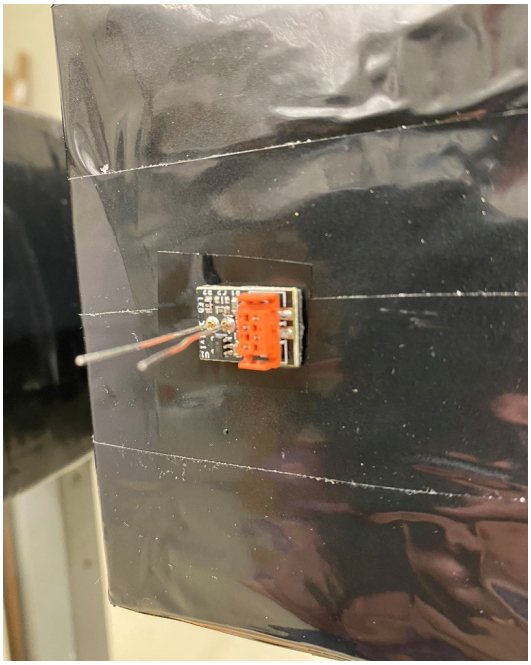

Figure 3.14: LED attached to the scintillating unit; back view of the electronic board driving it.

3.3 The MAPP Support Structure

The scintillator bars are held in place utilizing a set of grids comprised of hard, resistant plastic: HDPE 500. Three of these grids are used for each of the four scintillator sections. The frame that supports the HDPE structure of the detector's scintillator bars is made of generic T-bar extruded aluminum construction bars [42]. See Figure 3.15. The support structure is designed to point each longitudinal group of four scintillator bars so that they point to the collision vertex. Thus, each mCP impinging on the MAPP detector will pass through four scintillator bars, i.e., 3 m of scintillator, readout by four PMTs in coincidence. Figure 3.16 shows the preliminary steps of the assembly of the detector.

Figure 3.15: MAPP-mCP's HDPE 500 frame grids and sturdy aluminum frame.

Figure 3.16: Preliminary assembly of the MAPP-mCP detector at CERN.

3.4 PMT Mounting and Testing

3.4.1 PMT Mount

A PMT is mounted to each scintillator bar. The contact between the scintillator bars and the PMT is achieved through an intermediate clear, Sylgard 184 silicone light guide (see Figures 3.17 & 3.18). This light guide is also wrapped in Tyvek and black tape, to trap light all the way to the surface of the PMT, where the PMT and the light guide are in contact. The PMT is mounted on the scintillator bar using a PVC plastic mount, as shown in Figure 3.19. This mount was design on the computer and made through model injections (Figures 3.20 & 3.21). Figure 3.22 shows a view of the inside of the mount with the PMT and cushioning light guides placed together in contact.

Figure 3.17: PMT light guide.

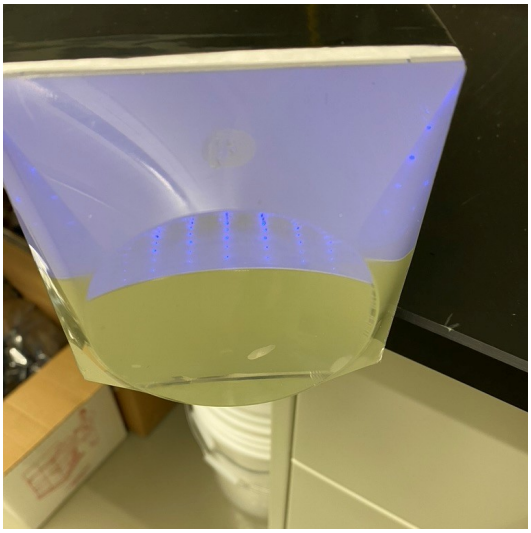

Figure 3.18: View of the light guide attached to the end of the scintillating unit.

Figure 3.19: PMT plastic mount/housing.

Figure 3.20: PMT metallic mold.

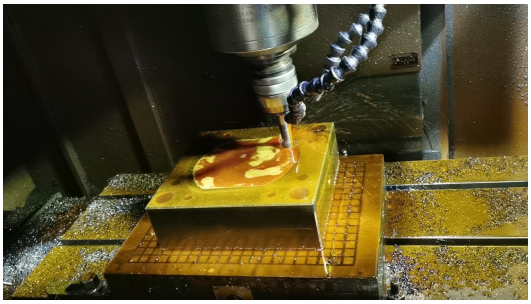

Figure 3.21: Making of the PMT metallic mold.

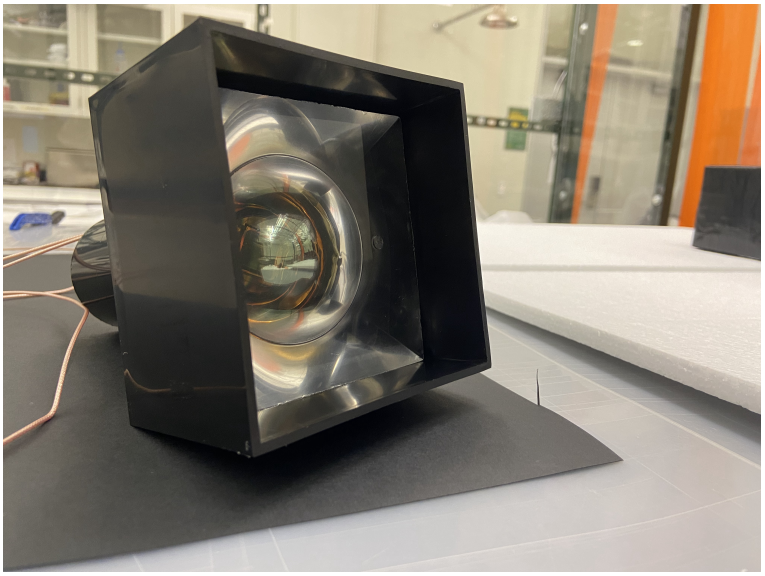

Figure 3.22: View of the contact between the cushioning light guides within the PMT housing/mount.

The silicone rubber light guides were fabricated using metallic molds. The elements of the silicone rubber mixture used in the light-guides were, for each 914 g of silicon, 740 g of base, and 74 g of curing agent. The silicone mixture was subject to degassing under vacuum and then poured into metal molds that were baked in an oven for 3 hours at 82 °C to set the material. Sylgard has desirable properties for the applications in mind, such as very good light transmission and similar refractive index to the scintillator employed (see Table 3.1). The silicon rubber also provides a tight coupling when strongly held against the end of the scintillating bars (see

Figures 3.18 & 3.23). In this way, an air-free contact between the PMT and the light guide is maintained. Figures 3.24 & 3.25 show the transmission and absorption indices of Sylgard 184 at 100 °C. According to [43], the recommended temperature range for using this material is -45 °C to 200 °C. Studies have determined that in the UA83 tunnel, part of the LHC tunnel infrastructure, the MAPP detector will be subjected to a steady room temperature that hardly varies by more than a few degrees centigrade.

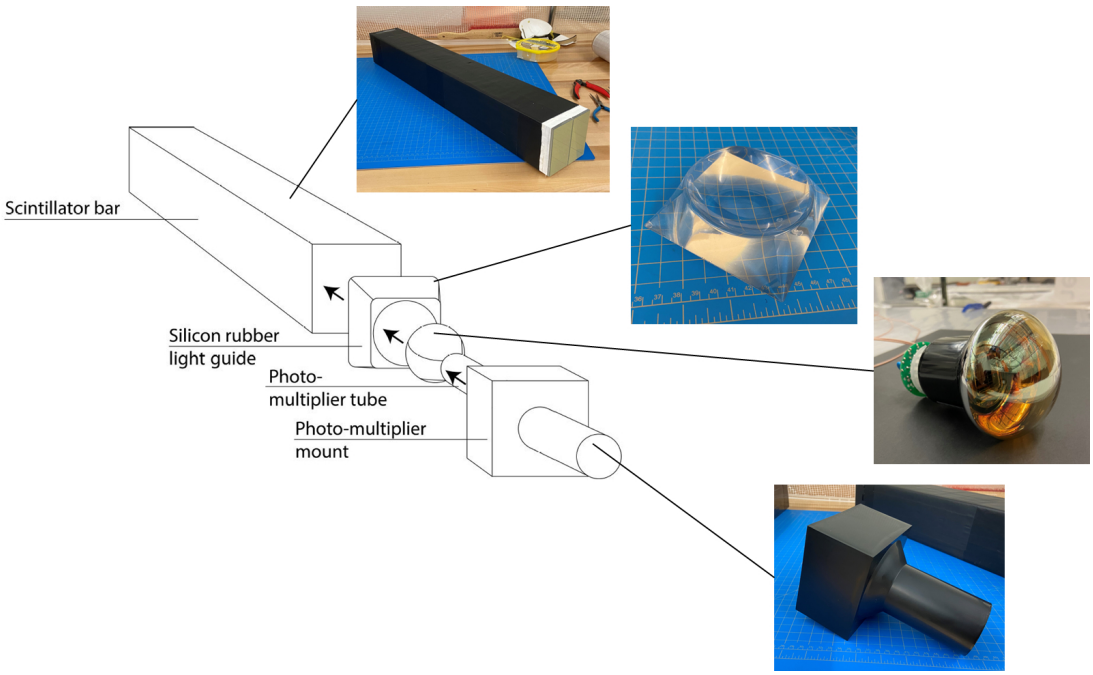

Figure 3.23: Diagram of the optical coupling between the PMT, light guide and scintillator bar, along with its assembly with the PMT mount.

Property	Unit	Result
Refractive index	@ 589nm	1.4118
=	@ 632.8nm	1.4225
=	@ 1321nm	1.4028
=	@ 1554nm	1.3997

Table 3.1: Refractive index of Sylgard 184 at different wavelengths. Taken from [43].

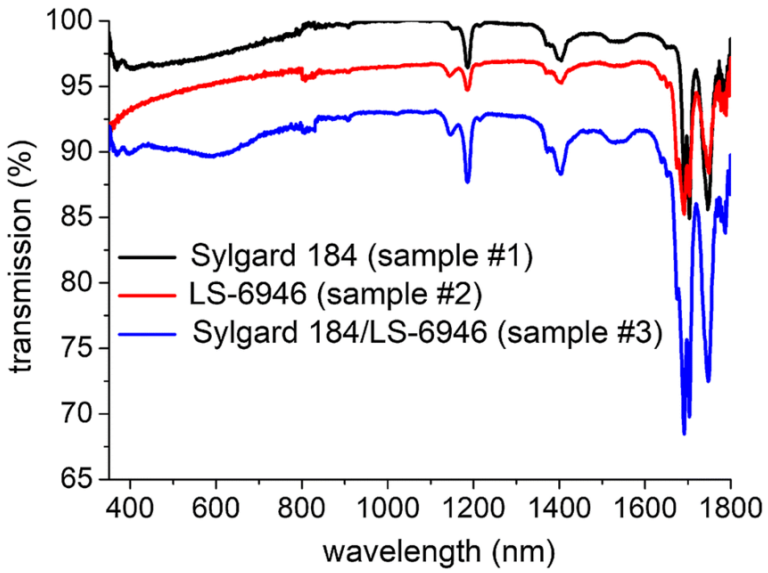

Figure 3.24: Transmission spectra of the optical elastomer Sylgard 184, LS-6946, and a mixture of Sylgard 184 with LS-6946. Taken from [44].

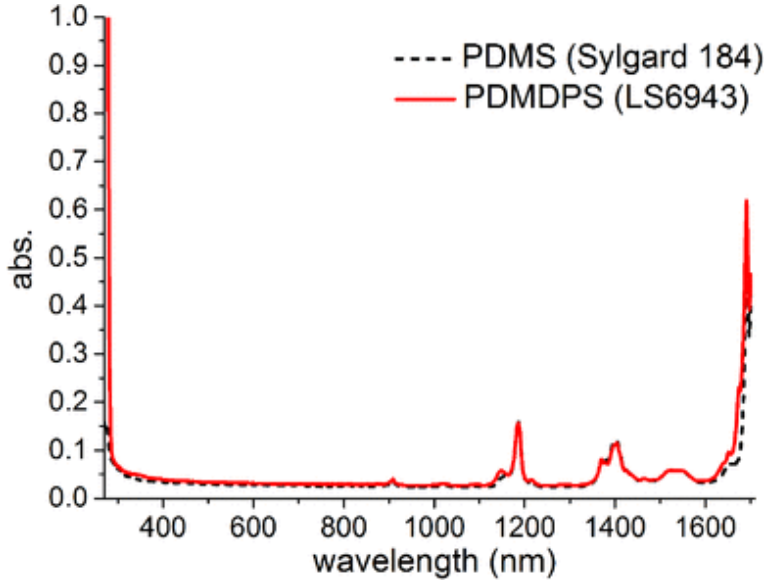

Figure 3.25: Absorption spectra of LS6945 and Sylgard 184 elastomer. Taken from [45].

3.4.2 PMT Testing

The main purpose of testing the PMTs was to determine the voltage at which the PMTs should be operated. The operating point of the PMTs was determined utilizing a laser pulsing system. The basic setup is shown in Figures 3.26 & 3.27. The laser unit was triggered using a signal generator (Figure 3.28). Square pulses at 1 kHz triggered the laser unit, as shown in Figures 3.29 and 3.30. The light was directed into a dark box via an optical fibre. The laser light was passed through a collimator and then a series of optical splitters and filters; these splitters and filters allowed for the testing of multiple PMTs in a single run. At the same time, they were selected such that about the same amount of light reached each PMT. See Figure 3.31 for details.

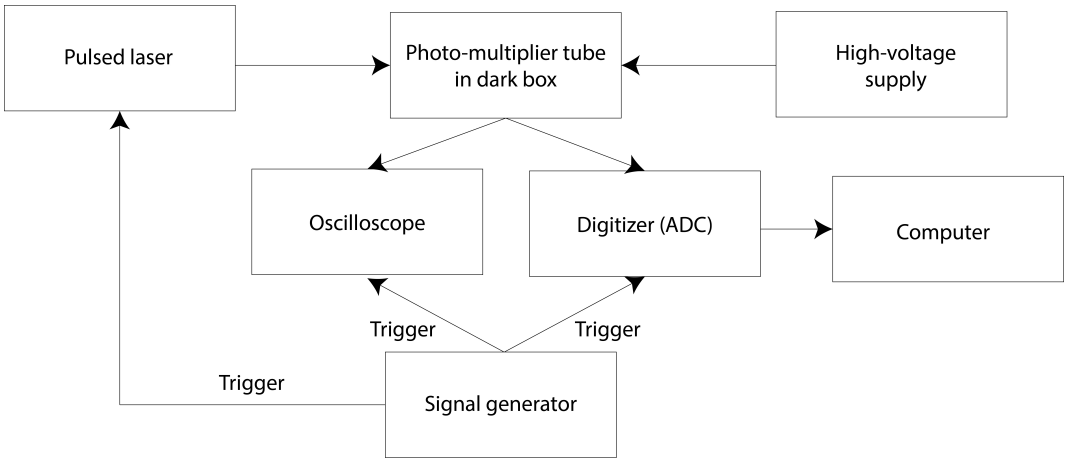

Figure 3.26: Laser pulser setup diagram for Figure 3.27. For the testing of the PMTs, the signal generator triggered the laser, digitizer (analog-to-digital converter, or ADC), and the oscilloscope at the same time. This ensured that 1) the PMT signal seen at the oscilloscope corresponded to that of the photon captures from the laser by the PMT (see Figure 3.29), and 2) that the ADC was passing data at the same rate as the laser was being triggered (see Figure 3.36), meaning that what the computer read coincided with the photon capture by the PMT.

The PMTs in the dark box were connected to a multiple-channel high-voltage supply (Figure 3.32), and their signals, when triggered by the signal generator-driven laser, were sent to a digitizer (Figure 3.33) that was also triggered by the signal generator. The digitizer's signals were sent to the computer for processing. The optical table within the dark box was setup in such a way that the amount of light reaching each PMT was roughly the same. In addition, the final light beam hitting the PMTs' cathodes was made as dim as possible, so that the signals reaching the digitizer were not too large. Care was also taken to ensure that the

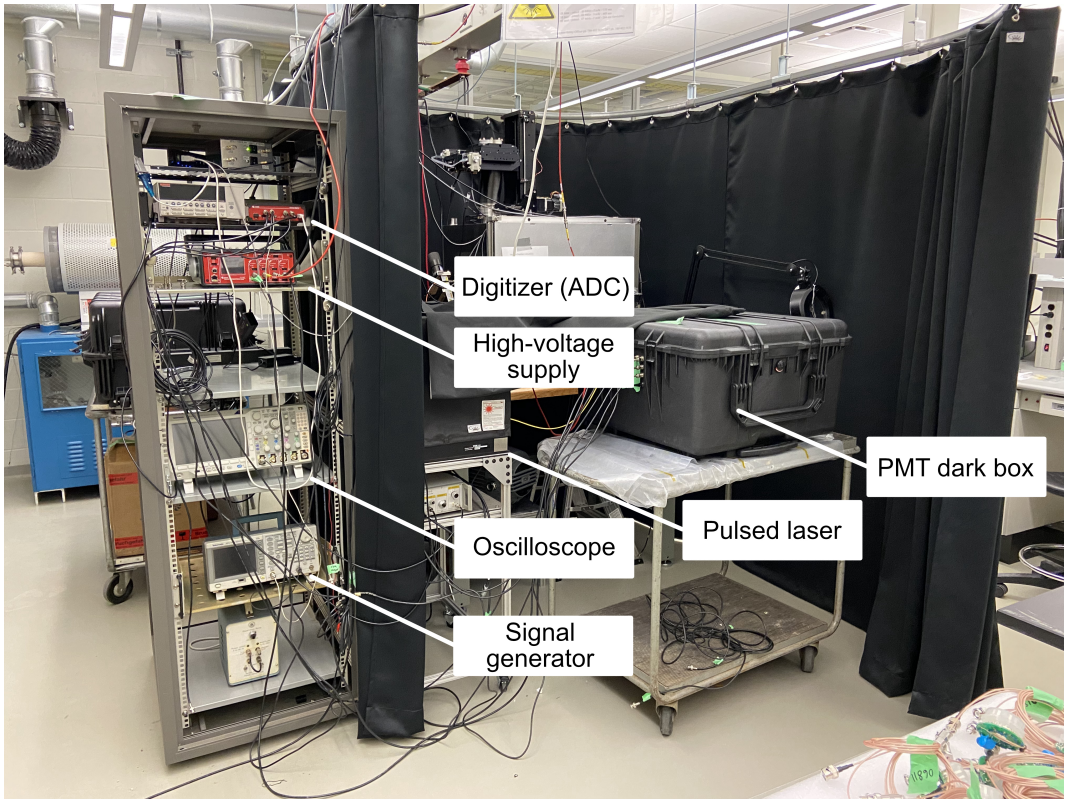

Figure 3.27: The laser pulser system used to make the measurements. The connections are made as in Figure 3.26.

signals coming from the PMT from the laser pulses were bigger in comparison to dark noise or electronic noise signals.

The data collection process consisted of increasing the voltage applied to the PMTs while leaving the lsb (least-significant bit; 1 lsb $\approx$ 0.97 mV) discriminator threshold fixed. The data collection per voltage applied was for 180 seconds or 60 seconds, from 800 V or 900 V up to possibly 1790 V (the maximum voltage tolerance of the electronic boards driving the PMTs was 1800 V). The data collection per high voltage was kept on going until a good plateau in the count rate (vs high voltage) plot was observable (see Section 3.4.3). The point at which this curve starts bending towards a plateau tells us at which voltage the PMT should be operated.

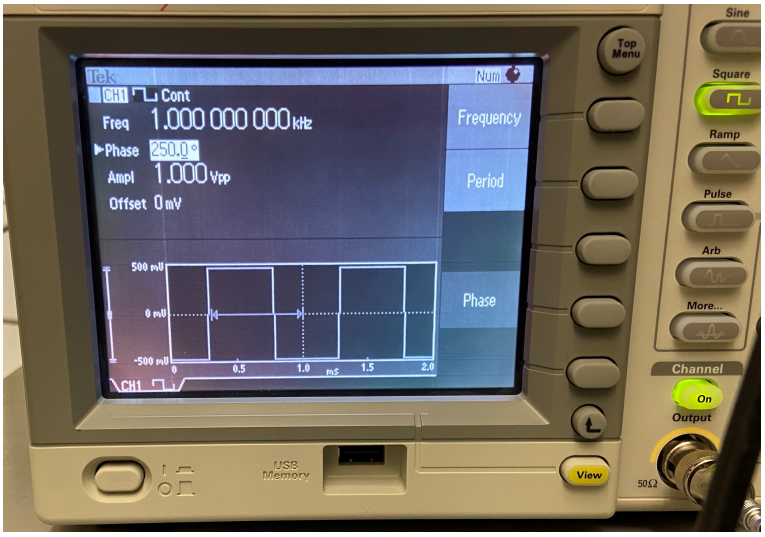

Figure 3.28: Signal generator used for driving the laser pulser. Setup: 1000 HZ square pulses, at 1 V each. The phase or, alternatively, the pulse thickness could be changed in order to match the pulsing and PMT signal timing.

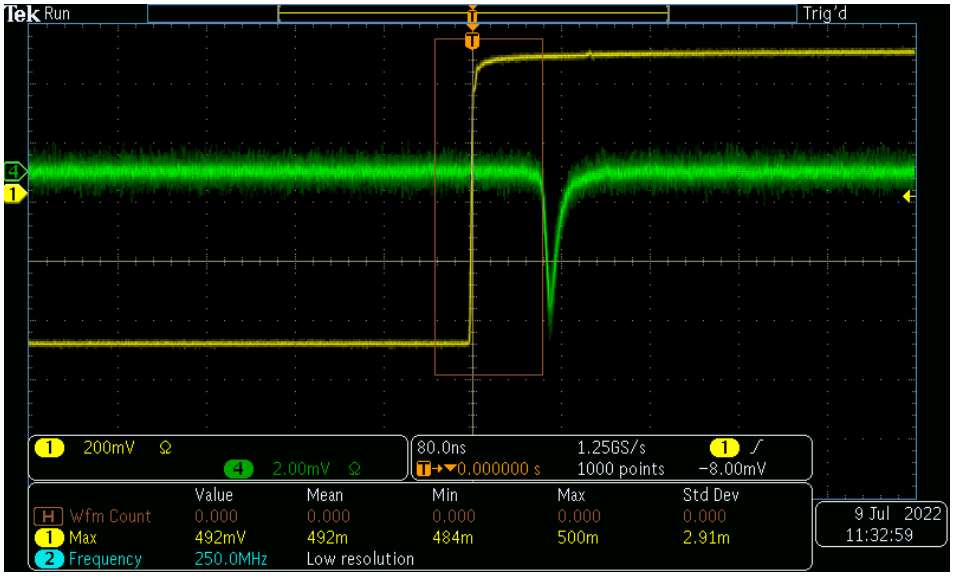

Figure 3.29: The PMT signal (green) that falls within the square pulse (yellow) produced by the signal generator (see Figure 3.30).

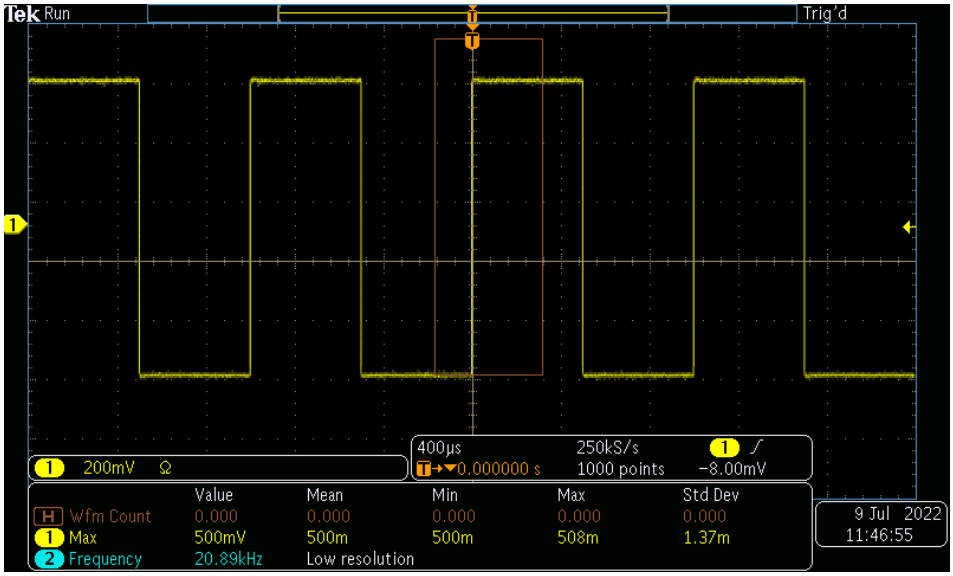

Figure 3.30: Signal generator pulses as seen on the oscilloscope. 1 kHz square pulses of 1 V amplitude.

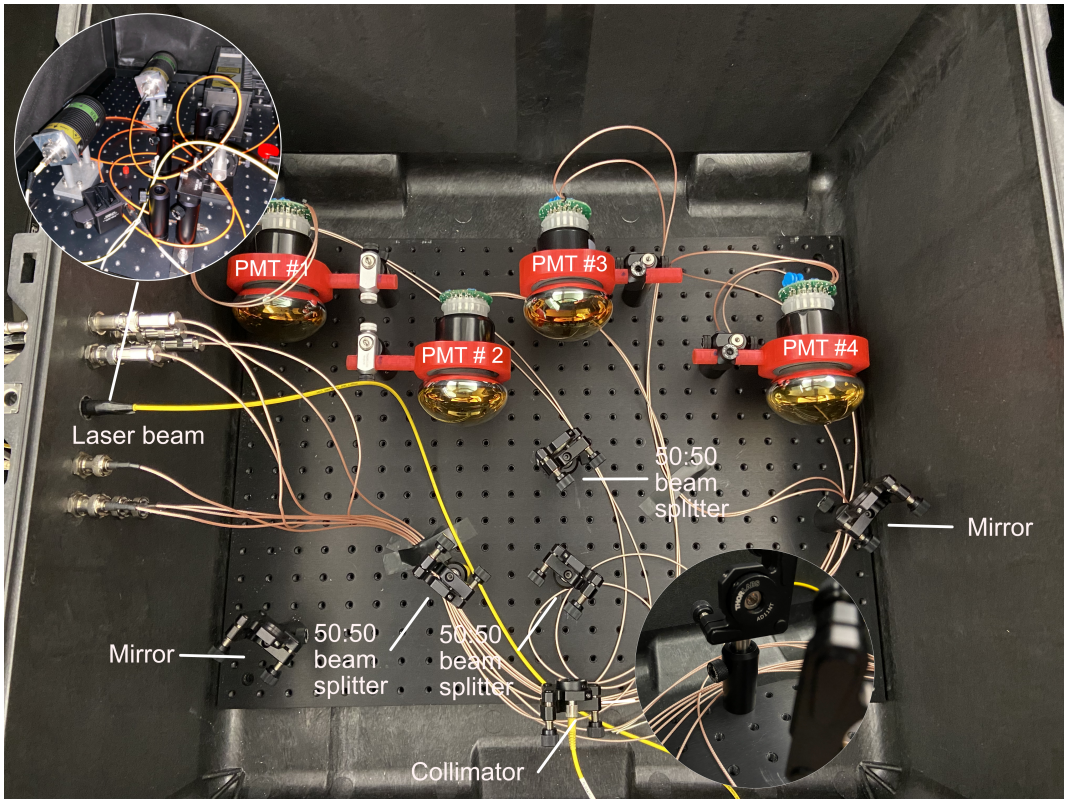

Figure 3.31: Optical table setup. The laser light travels through an optical fiber (yellow cable) which then is passed through a collimator. Before reaching PMT #1, the light passes through two 50:50 beam splitters. When reaching PMT #2, it also passes through two 50:50 beam splitters. The light reaching PMTs #3 and #4 is redirected towards them via the use of mirrors. The optical equipment was chosen so the optical wavelengths at which it works optimally match the laser's wavelength. In addition, the setup is such that about the same amount of light reaches each PMT.

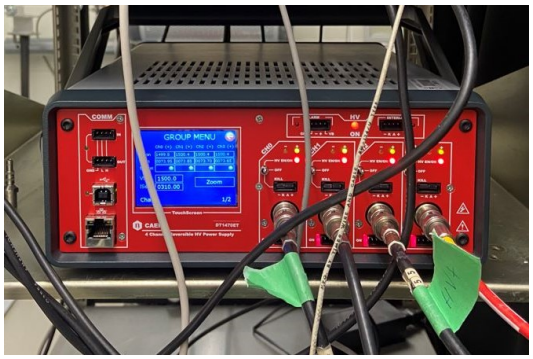

Figure 3.32: HV supply driving four channels at the same time.

Figure 3.33: Digitizer used to send incoming PMT signals to the computer.

3.4.3 Results

The PMT signals obtained from the setup described above were clean and easily identifiable. These were significantly larger than noise signals, even at relatively low voltages. Figure 3.34 shows a typical waveform of a PMT as acquired by the digitizer.

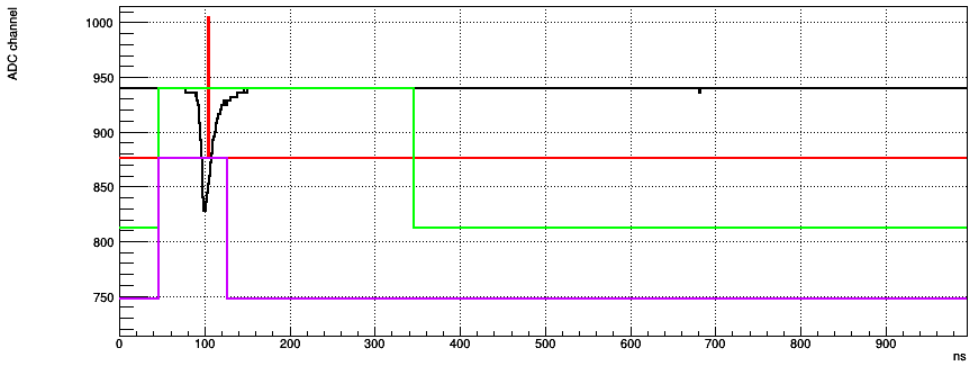

Figure 3.34: Sample wave-form of an incoming signal from a PMT (black) being tested at around the plateau region, coming from the digitizer and as filtered out by the computer software using a 300 ns long gate (green), 80 ns short gate (purple), and 5 ns trigger (red) at a 50 lsb theshold.

For the general test of the PMTs, a 50 lsb threshold and a 300 ns gate were chosen, as they gave the best results. The digitizer was triggered at 1 kHz, along with the laser pulser, by an external signal generator, and these were put in

coincidence (see Figure 3.28). For the initial tests, the PMTs were subject to the high voltage for 180 seconds first, and later, as the procedure became well established, the testing time was reduced to 60 seconds.

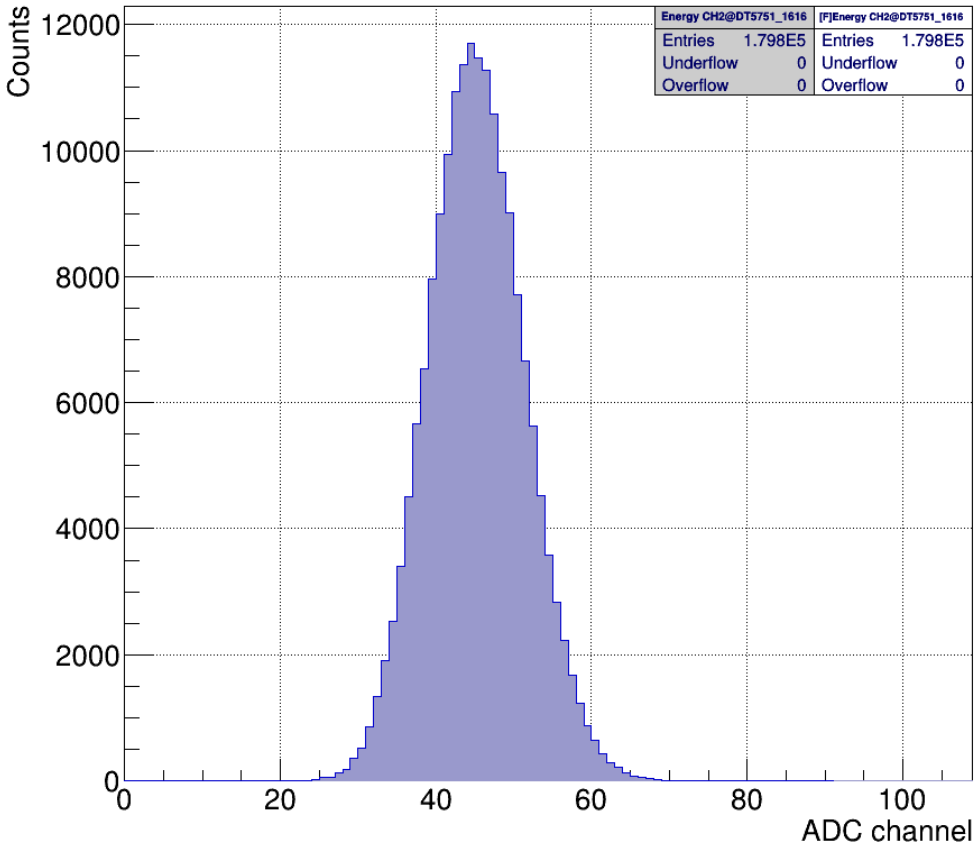

Figure 3.35: Sample histogram of a tested PMT at 1200 V, just at the beginning of the plateau region of Figure 3.38. All noise is filtered out at a 50 lsb threshold.

Figure 3.35 shows the ADC data for a PMT tested at a 1200 V, just past the plateauing threshold, for 180 seconds. The noise signals have been mitigated with the 50 lsb threshold set in the software. The data are expected to follow a Gaussian distribution. The software was seen to capture data with the event rate at the digitizer, consistent with the signal generator being set at 1 kHz, as shown in Figure 3.36. From Figure 3.37, it is easy to extract the uncertainties needed to generate a count rate vs high voltage plot, an example of which is given in Figure 3.38.

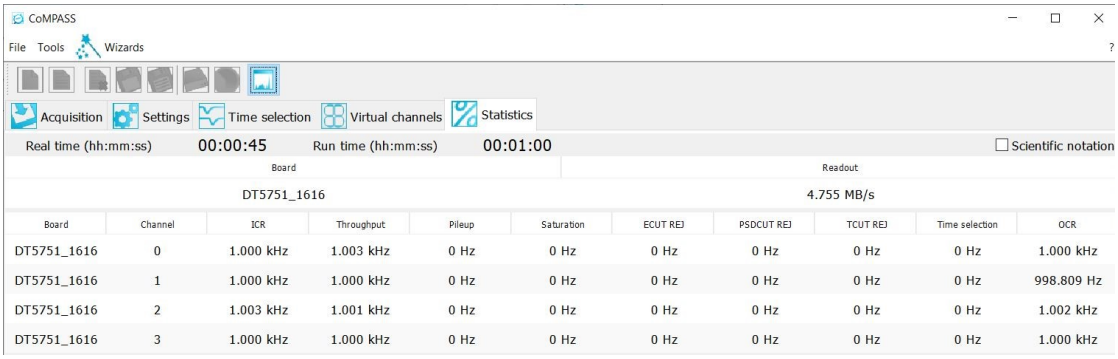

Board	Channel	ICR	Throughput	Pileup	Saturation	ECUT REJ	PSDCUT REJ	TCUT REJ	Time selection	OCR
DT5751_1616	0	1.000 kHz	1.003 kHz	0 Hz	0 Hz	0 Hz	0 Hz	0 Hz	0 Hz	1.000 kHz
DT5751_1616	1	1.000 kHz	1.000 kHz	0 Hz	0 Hz	0 Hz	0 Hz	0 Hz	0 Hz	998.809 Hz
DT5751_1616	2	1.003 kHz	1.001 kHz	0 Hz	0 Hz	0 Hz	0 Hz	0 Hz	0 Hz	1.002 kHz
DT5751_1616	3	1.000 kHz	1.000 kHz	0 Hz	0 Hz	0 Hz	0 Hz	0 Hz	0 Hz	1.000 kHz

Figure 3.36: Software collecting data from a CAEN DT5751 digitizer pulsed at 1 kHZ (ICR column showing the rate of events coming at the digitizer input) in the four different channels 0, 1, 2, and 3, connected to the PMTs 1, 2, 3, and 4, respectively, ensuring that the registered signals corresponded to the pulsed laser and subsequent photon detection by the photo-multiplier tube. The data rate from the board, or throughput, as well as the rate of evens passing the cuts/filters and filling the histogram, or OCR, are both as well at roughly 1 kHz. At higher voltages, the electronic noise in the PMT becomes noticeable in the energy histogram (Figure 3.39).

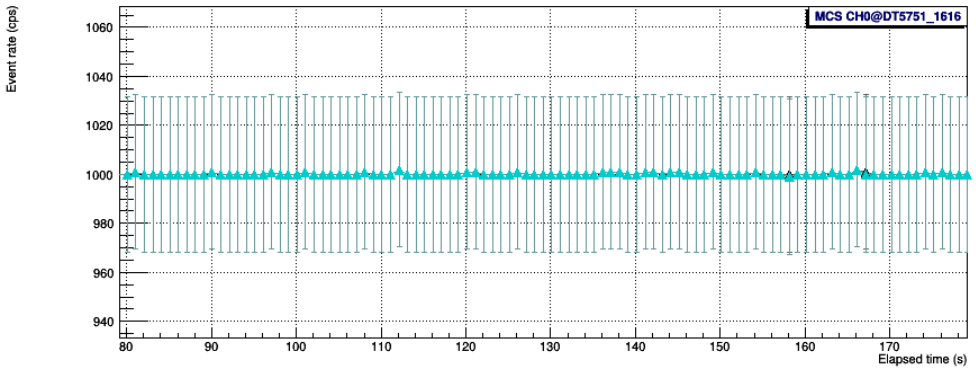

Figure 3.37: Count rate plot as determined by the software reading out the digitizer. These plots were used to determine the error bars in the count rate curve in Figure 3.38. The error bars would vary depending on the applied high voltage; for this case, voltage $= 1300V$.

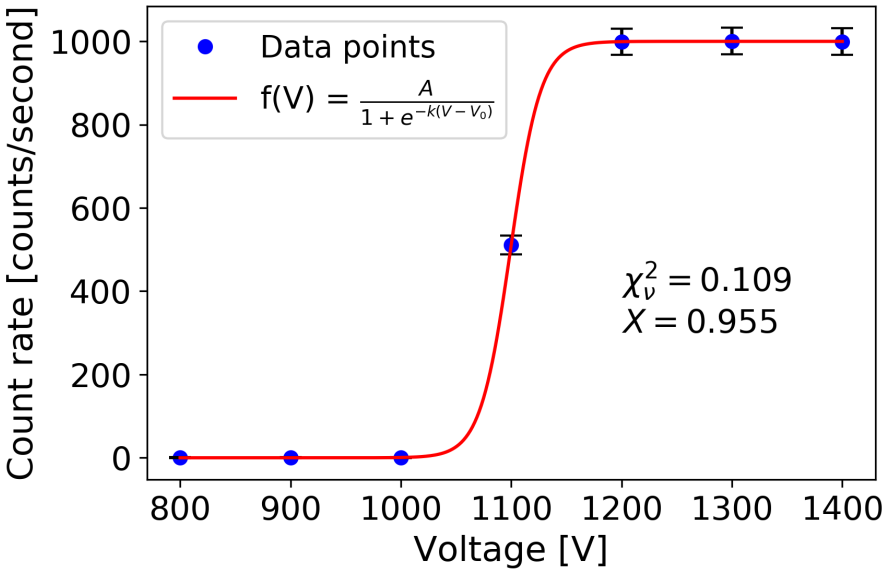

Figure 3.38: Typical count rate curve of a PMT up to the plateau region. The error bars are too small to be visible at 800 V to 1000 V; they were determined by a built-in software function (see Figure 3.37). The uncertainties come mainly from Poissonian statistics and *shot* noise.

Figure 3.38 tells at which high voltage the PMT should be operated (at about 1200 V, in this case), and that is just at the point where the plateau begins. Figure 3.34 shows the waveform of the incoming data as seen by the software after filtering out the noise at the plateau region. Plots like Figure 3.38 were generated for each PMT, from which it was found their optimal operating voltage.

As the high voltage is further increased, however, the random noise in the PMT becomes big enough to surpass the set threshold. This is shown in Figure 3.39, where the noise is becoming overwhelmingly high. At even higher voltages, the noise becomes comparable to, or even more significant, than the real PMT signal from photon captures, indicating that the data is not coming from the pulsing laser alone, but also from random, uncontrolled events.

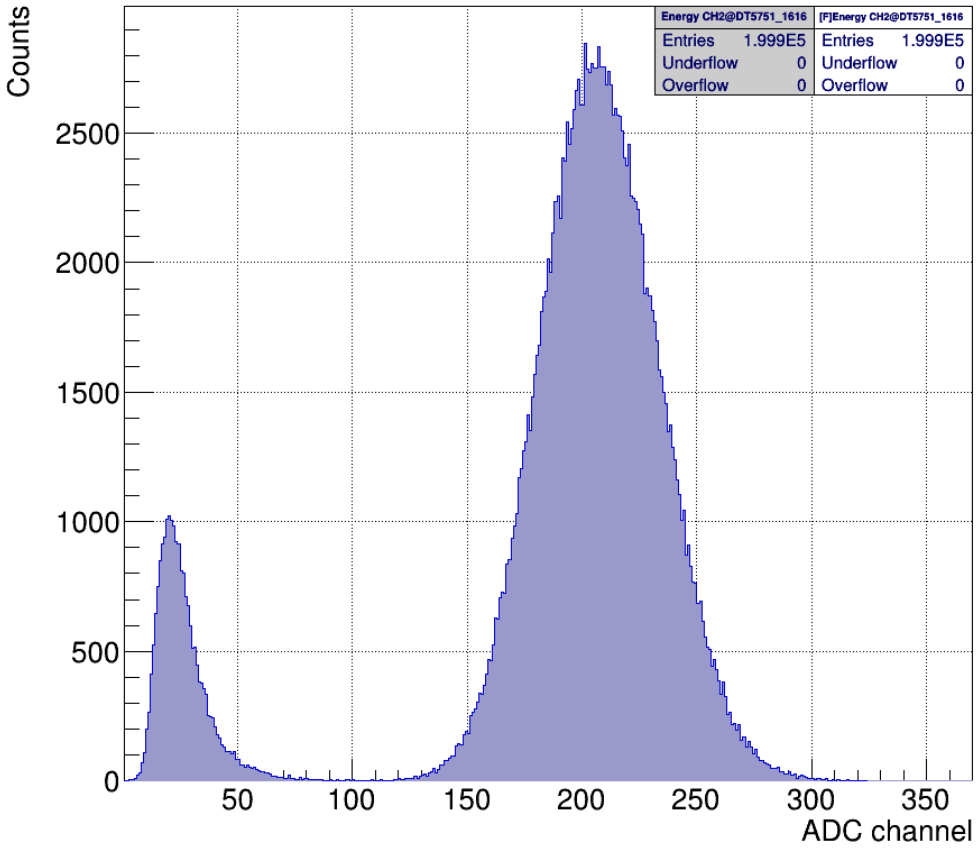

Figure 3.39: PMT tested in Figure 3.35 at 1200 V, just over the plateau break (see Figure 3.38) now tested beyond the plateau region, at 1500 V. The noise here has made it past the 50 lsb threshold and can be seen in the histogram (left pedestal); the PMT signals from photo-detection are collected in the pedestal to the right.

Chapter 4

Vertex Reconstruction Study and MAPP-2

A software model of a test decay volume "detector" was built in order to study the issue of tracking and vertexing of particles decaying within MAPP-2. This test detector consists of three boxes missing one face, one box inside the other, much like Russian dolls. Each box's face is made up of a single scintillator plate readout on each side by an "x" oriented WLS fibre array and a "y" oriented WLS fibre array; both arrays at right angles to each other, making up effectively a grid (Figure 2.15. Figure 4.1 shows the basic geometry of the detector; box C encloses box B, which encloses box A. See Figure 4.2 for a sample image of a scintillating plank with optical fibres embedded in it made for testing purposes.

The detection of light from the WLS fibres is achieved using SiPMs. These optical fibres are placed at right angles to each other, on either side of a 1.25 cm thick scintillator sheet, making up a grid of 1 cm $\times$ 1 cm scintillating "squares". A hit in one of these squares would trigger mainly four optical fibres, two per axis. This would allow the observer to estimate where the hit in the detection plane happened. By utilizing hits in each layer the first iteration of a tracking and vertexing program capable of efficiently operating in the presence of "noise" hits was created.

The approach used is that detailed in [46]: finding track candidates by drawing curves/lines that best fit the data points, and then evaluating these via a goodness-of-fit test. The chi-square test is a method of goodness of fit allowing the algorithm to evaluate tracks that are similar in length. The first step of finding track candidates is performed by subjecting fitted lines to an evaluation of the goodness of fit using a χ^2 test. This test can be misleading in the sense that a poor χ^2 value does not necessarily mean a poor fit when compared to a better fit result. This usually arises in cases in which one is comparing a shorter track to a longer track, with the shorter track exhibiting, generally, a better fit result than the longer one

[46]. This problem is ameliorated in the MAPP detector, however, by remembering that the tracks we are seeking emanate from a common vertex and are boosted in the direction of the decaying particle. Hence the detected tracks will tend to be roughly equal in length.

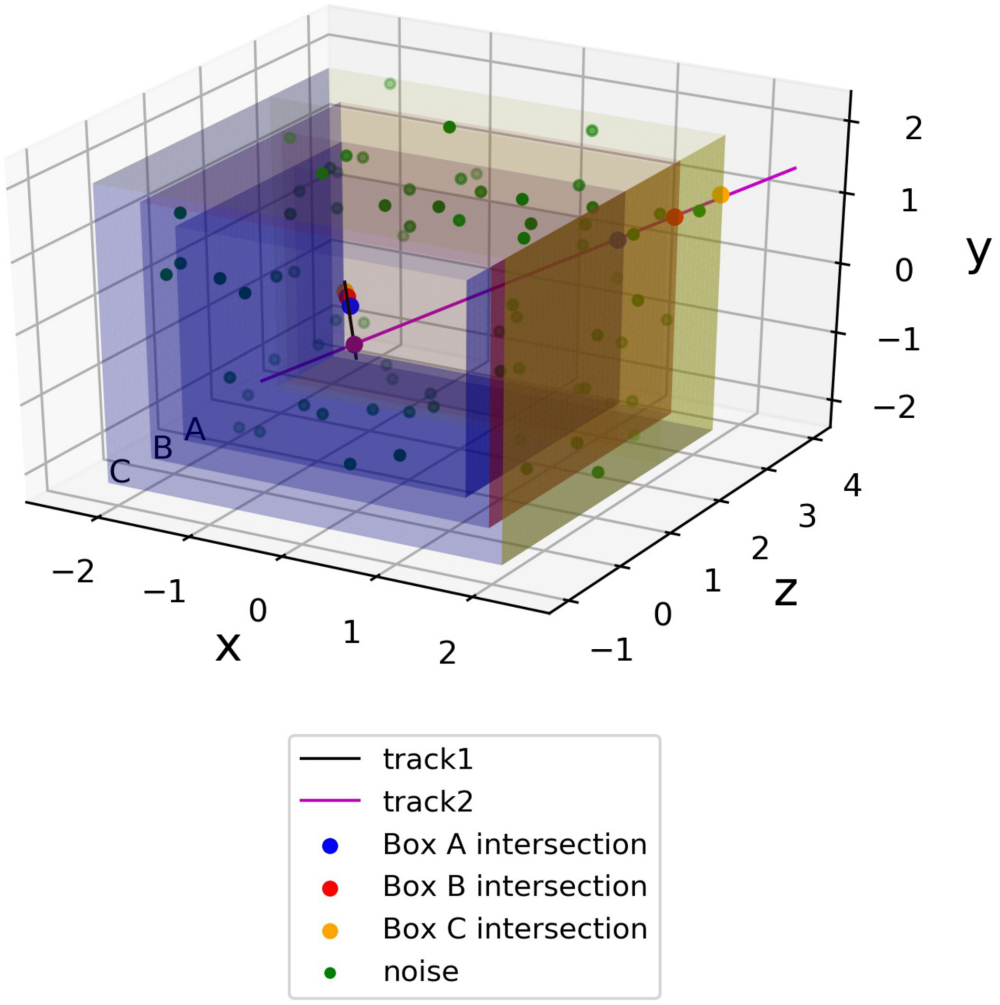

Figure 4.1: Figure of the three-box simulation real hits generation. The vertex reconstruction algorithm, however, flips the location of the back walls of the boxes to the negative z axis.

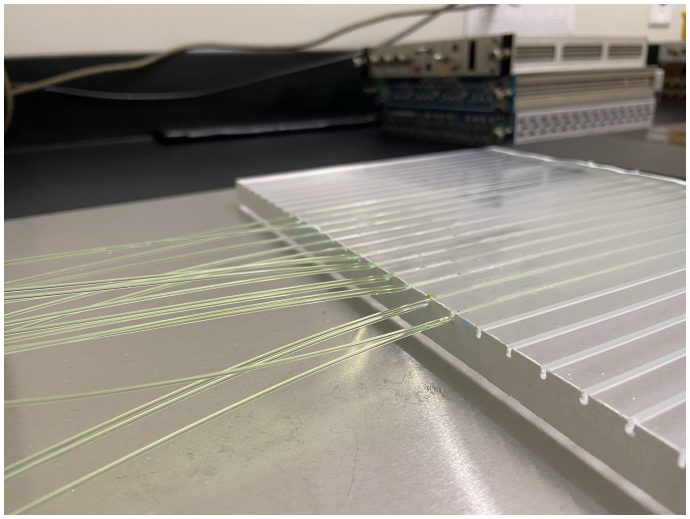

Figure 4.2: Scintillator tile with parallel optical fibres embedded in it.

Since the detector in question is a series of boxes, one enclosing the preceding one, the problem at hand can be solved in a three-step procedure: 1) finding track candidates (i.e., those tracks consisting of three points that can be fitted well enough to a line), 2) evaluating these track candidates, and 3) forming vertices using the good track candidates. We consider two types of points: the real hits in each detection wall (detection plane from now on) and noise hits (or the background).

We assume that the detected tracks originate from a decay vertex occurring somewhere in a detection volume (within the volume of the innermost box). Several different track candidates with the best χ^2 results of ≤ 0.5 are tested for a point of intersection in the volume of the test detector. The tracks will not perfectly intersect in three dimensions, but they do in two dimensions. The tracks that do NOT intersect perfectly in two dimensions within the innermost box's volume are eliminated from the track candidates, and those that do intersect perfectly in two dimensions within this volume are kept in the candidate pool. These remaining tracks will have two points in the third dimension that correspond to the point of intersection in two dimensions. The distance in the third dimension is calculated, and the two tracks that exhibit the smallest distance of closest approach are kept as the tracks originated from the real, simulated, decay.

The objective of this vertex reconstruction study is to identify a decay vertex and the tracks forming the vertex. The final results provided at the end of the section are i) the vertex finding efficiency of the detector, with the efficiency basically defined as

$$Efficiency = \frac{\#\ of\ correct\ vertex\ reconstructions}{\#\ of\ trials}, \tag{4.1}$$

and ii) the vertex reconstruction accuracy, i.e., the distance between the real (simulated) vertex to the reconstructed vertex (generated from the best track candidate method described above). In addition to this, several suggestions and preliminary analysis results of further improvements to the algorithm are proposed.

4.1 The Algorithm

4.1.1 Particle Decay and Hits Simulation

The vertexing algorithm described below was implemented through Python and Matlab, and the codes and functions can be found in Appendix A. The first step is to generate hits on the walls of the detection boxes. A set of three boxes is built, one inside the other, all of them missing the "front" wall, i.e., the one that faces the incoming particle that subsequently decays in the fiducial volume of the test detector. The walls surrounding the decay point are placed, starting from the smallest to the biggest box, at z = -2.40 m (box A), -2.90 m (box B), and -3.20 m (box C). See Figure 4.1 for the orientation of the boxes in space.

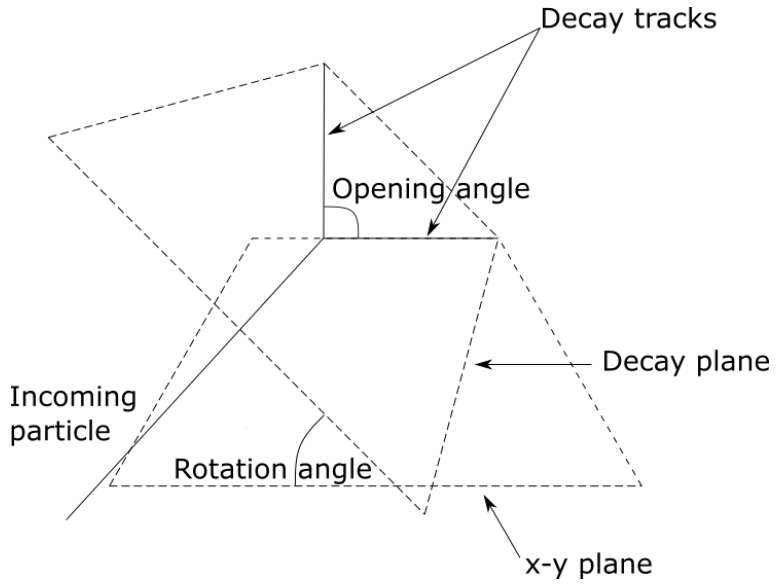

Figure 4.3: Definition of the "opening" and "rotation" angles in the vertex reconstruction algorithm.

In the algorithm, it is assumed that the incoming particle decays at the origin $(0, 0, 0)$ in 3D space. This particle is coming straight ahead towards the boxes along the z axis, in the negative direction, and its two decay products fly off at equal angles from the original direction of motion of the initial particle. The decay

products can decay at any rotation angle of the plane formed by the two tracks and the "x-z" plane. The tracks will always extend forwards towards the boxes due to conservation of momentum, as indicated in Figure 4.3. The algorithm proceeds by identifying where the decay products hit the three boxes and storing the resulting coordinates in text files. See Appendix A for further details.

At this point the computer has simulated the production of a pair of decay products that passed through specific spots on the detection walls of the boxes making up the detector. The next step is to create noise points on the detection walls of the boxes. These noise points are random coordinates generated along the walls of the the boxes. The noise hits are added to the hits arising from the passage of particles crossing the detector layers.

4.1.2 Optical Fibres and Noise Generation

As described above, WLS fibre are embedded in the scintillator planes forming the walls of the boxes. The WLS fibres define a grid of 1 cm $\times$ 1 cm squares, as depicted in Figure 2.26. It is then assumed that as the ionizing particle hits one of these squares, four optical fibres will catch most of the light produced in the particle-scintillator interaction: two fibers along say the y axis and two fibers along the x axis, as shown in Figure 4.4.

The two optical fibres enclosing the "hit" will capture some light produced by the hit's interaction with the scintillator material. Because of the design of the detector, one can only know the position of the "hit" down to the coordinates on which the optical fibre are placed. For each coordinate, "x" and "y", it is assumed that the optical fibre closer to the "hit", this is the fibre on the right to the "hit" in Figure 4.4, for instance, will transport more light than the other one. The code then substitutes the exact location of the "hit" by the coordinates where the "x" and "y" fibres are placed. The "z" coordinate remains the same, as this is the location of the wall, and this is exact.

The next step is to generate coordinates for noise points. For simplicity, an equal amount of noise points are generated per wall on all the three boxes. These points are randomly generated.

4.1.3 Data Combination and Sorting

At this point, it is important to mention that the coordinates of both the simulated real hits and the noise are organized in matrices; one matrix per axis. Care is taken to make sure that the coordinate triplets (one per box) are kept in the same rows, although these rows could be moved around. See Equation 4.2, which shows the matrix configuration of the coordinates information for the tracking algorithm: A, B, and C correspond to the three different boxes; 1 and 2 make reference to the

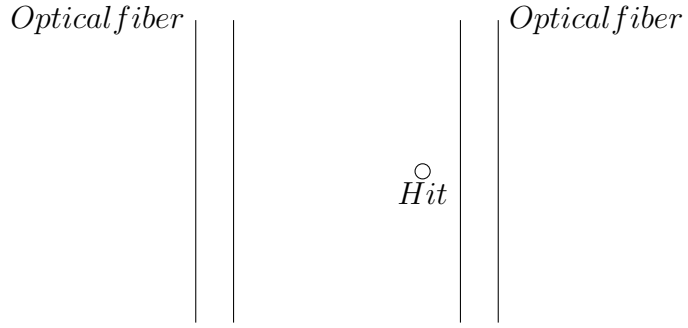

Figure 4.4: A hit in between two optical fibres means that both fibres are assumed to be hit.

two decay tracks; x, y, and z are the three different axes in Cartesian space; finally, n stands for "noise". The matrices have three columns, one per box, and these columns are not moved around at any point in the code, only the rows.

$$\begin{pmatrix} \text{A1x} & \text{B1x} & \text{C1x} \\ \text{A2x} & \text{B2x} & \text{C2x} \\ \text{Anx} & \text{Bnx} & \text{Cnx} \\ \text{...} & \text{...} & \text{...} \end{pmatrix} \leftrightarrow \begin{pmatrix} \text{A1y} & \text{B1y} & \text{C1y} \\ \text{A2y} & \text{B2y} & \text{C2y} \\ \text{Any} & \text{Bny} & \text{Cny} \\ \text{...} & \text{...} & \text{...} \end{pmatrix} \leftrightarrow \begin{pmatrix} \text{A1z} & \text{B1z} & \text{C1z} \\ \text{A2z} & \text{B2z} & \text{C2z} \\ \text{Anz} & \text{Bnz} & \text{Cnz} \\ \text{...} & \text{...} & \text{...} \end{pmatrix} \tag{4.2}$$

All the information is now mixed in a set of three matrices containing the simulated real coordinates and the noise coordinates. For future use in the testing of the code's efficiency in reconstructing the decay vertex, a second set of matrices is created, in which the coordinates of the simulated real hits are stored for the two tracks. This second set of matrices is put aside for the moment.

4.1.4 Least-Squares Fit

Working with the first set of three matrices, where the real hits and the noise points are mixed together, one does not know which coordinates correspond to the simulated real hits and which ones are noise. The algorithm then attempts to identify the simulated real hits by means of a chi-square goodness of fit after fitting a line through the boxes by means of a least-squares fit, looking at all the possible combination of points that could make a line.

The least-squares analysis extracts the best fit parameters for any possible combination of points, the *slope* and the $y_{intercept}$ in Equation 4.4. For instance, in an "$x - y$" plot one could assume a linear relationship between the "x" and "y" coordinates, and this is the case for our purposes: the decay particles are assumed to move in a straight line. However, that this relationship is linear does not necessarily

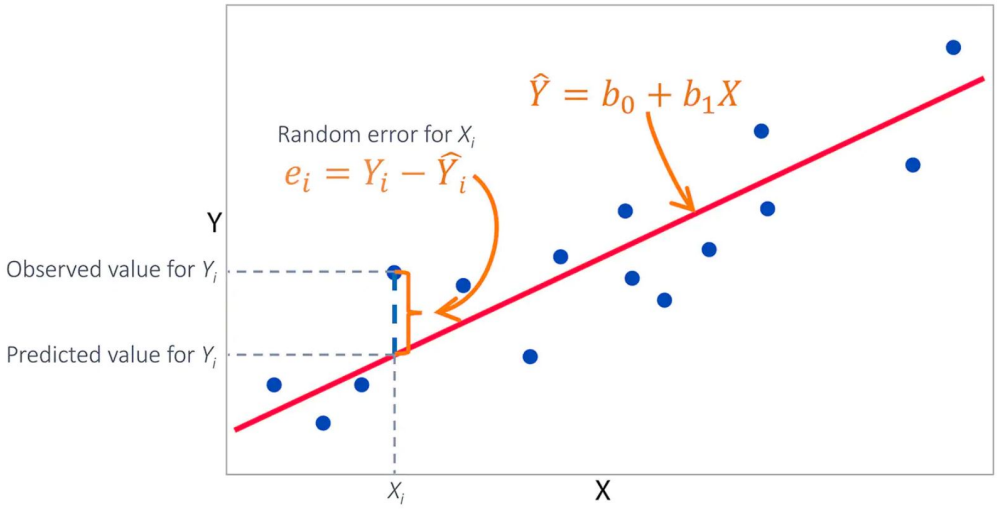

Figure 4.5: Least-squares fitting of a straight line in between "observed" data points. Taken from [47].

mean that the points fall exactly on a line, only that one could draw a straight line passing, as best as it could, in between the data points, as shown in Figure 4.5. So, making "x" the independent variable and "y" the dependent variable, one has the *observed* "y" coordinates corresponding each to an "x" coordinate. But, if one draws a line passing through the points in the plot, as in Figure 4.5, one can also have *fitted*, or *predicted*, "y" coordinates that correspond to each of the *observed* "x" coordinates. The best fit line will be the line that reduces the square difference of the $y_{observed}$ and the $y_{predicted}$ data (Equation 4.3).

$$\sum e^2_{line_j} = \sum \left(y_{observed} - y_{predicted}\right)^2 \tag{4.3}$$

$$y = slope \times x + y_{intercept} \tag{4.4}$$

The algorithm picks all combinations of hits in A, B, and C and keeps the best fits according to the following process: the computer picks a point in box C, then it proceeds to pick a point in box B, then a point in box A, and it extracts the fit parameters of a line through those three points. The code then picks another point in box A, keeping the two previously selected points in boxes B and C, and extracts the fit parameters. The algorithm does this until it has looked at all the points in box A while keeping those two previously selected points in boxes B and C. Once this is done, the algorithm picks another point in box B and proceeds, again, to look at all the points in box A. This is repeated until the code has done this with all the points in box B. Finally, the algorithm picks another point in box

C and the entire process described above is repeated until there are no more points in box C to pick.

The same least-squares concept described above for two dimensions can also be implemented for points existing in three dimensions. The extraction of the fit parameters of these points in three dimensions, however, is done in two steps: one first finds the fit parameters in two dimensions by looking at the point's coordinates in a plane, and then one adds a third dimension to the residual minimization process. In order to explain this, consider a coordinate system (l, m, n), with a decay particle moving along the n-axis. If the particle passes through three walls that parallel to the l-m plane and that are located at specific, known, n coordinates, then one knows where the hits of the particle passing through the walls in the n coordinates are *exactly*. So, one can start the least-squares fitting with the following process:

1) The code generates the best fit parameters in the l-n plane, because we know the n values exactly, and so "n" is treated as the independent variable. These "n" values, which happen to be the same for both simulated real hits and noise fitted coordinates, are just the positions of the detection walls in the n coordinate axis. One implements the best fit line, using n as the independent variable and l as the dependent one to obtain the fit parameters, slope and intercept, p_0 and p_1, respectively:

$$l_{predicted} = p_0 n_{observed} + p_1. \tag{4.5}$$

2) We repeat the process in 1) but adding a third dimension. This time, we use the fitted l and n values to generate m values according to the formula

$$m_{predicted} = c_0 n_{observed} + c_1 l_{predicted} + c_2, \tag{4.6}$$

where c_0, c_1, and c_2 are the fit parameters generated through a matrix implementation of the least-squares technique on the simulated and noise coordinates l, m, and n. The algorithm identifies the line with the c_i parameters for which

$$\sum e^2_{line_j} = \sum \left(m_o bserved - m_p redicted\right)^2 \tag{4.7}$$

is minimized.

Because it is assumed that the coordinates n are the ones where a detection plane is located, then it is needed that the algorithm identifies on which plane the hits occur. This is implemented in the code, and the algorithm is able to tell whether the point is located in the "straight ahead", "left", "right", "bottom", or "top" detection plane of a box (these labels are better understood by thinking of the direction of motion of the incoming particle *before* it decays). Whether a hit

occurs in any of these planes depends on two parameters: the opening decay angle and the rotation angle (See Figure 4.3 for a depiction of these angles, as well as Appendix A).

The procedure outlined here is made for all the permutation of points that form a line through the three boxes. The resulting fit parameters are stored in a matrix, and they are indexed according to their respective *observed* and *predicted* m coordinates.

4.1.5 Goodness of Fit Test

At this point, the algorithm has two sets of data: 1) the initial simulated and noise coordinates, which are the *observed* coordinates and 2) the fitted coordinates based on the best-fit line, which are the *predicted* coordinates. The next step would be to evaluate the degree by which the *observed* and *predicted* points agree for each line. This is done using the chi-square goodness of fit method according to the formula

$$\chi^2 = \sum_i \frac{\left(C_{predicted} - C_{observed}\right)_i^2}{\sigma^2_{observed_i}}, \tag{4.8}$$

where $C_{observed}$ is the simulated coordinate, corresponding to either a simulated real hit or a noise point; $C_{predicted}$ is the fitted coordinate from the least-squares analysis; and $\sigma_{observed}$ is the uncertainty in $C_{observed}$, which for this case it is chosen to be 0.005 m, half the side length of an effective square delimited by the optical fibres in the detection planes. The final value of a goodness of fit is determined via the integration of the chi-square density function

$$X\left(\chi^{2\prime};\nu\right) = \int_{\chi^{2\prime}=\chi^2}^{\chi^{2\prime}\to\infty} \frac{\chi^{2\prime\frac{\nu}{2}-1}\exp\left(-\chi^{2\prime}/2\right)}{2^{\nu/2}\Gamma\left(\nu/2\right)} d\chi^{2\prime}, \tag{4.9}$$

where $\nu = n - p$, with n being the number of data points and p the number of fit parameters. The value of the integration should be approximately 0.5 [48].

After performing a chi-square calculation on all the possible lines, the code picks the best of these results. These are, following [48], the ones closest to 0.5, which the algorithm takes to be those values larger than 0 and less than 0.5.

4.1.6 Point of Intersection Test and Minimal Distance Test

The algorithm assumes that the incoming particle decays at the Cartesian origin $(0, 0, 0)$, which is within the test "decay volume", the space within the concentric boxes. Once the data points with the best chi-square results have been identified, their corresponding lines are looked at closely by the code. Those lines that intersect within the decay volume are kept for further filtering.

Although these line do intersect exactly in a plane, they generally do not in all three dimensions. The algorithm then picks the two lines, among all the candidates, that provide the smallest distance between their z coordinates corresponding to the location in the $x - y$ plane at which they intersect exactly. The algorithm then assumes that the intersection point of these two lines is the middle point in between these two zs. At this point, the code stores in a set of matrices the *observed* data points that produced the best linear fit results and their point of intersection.

4.1.7 Final Test

With a chosen set of "observed" data points now available, the algorithm compares the original set with the final set. If they "match", then the reconstruction of the decay tracks and vertex is considered successful.

4.2 The Results

4.2.1 Vertex Reconstruction Resolution

Figure 4.6 shows the distances between the reconstructed vertices and the real vertices at the origin of the Cartesian space. After filtering out incorrect reconstructions, the result is that the impact parameter, or resolution, of the vertex reconstruction capacity of the algorithm is ± 2 cm.

4.2.2 Algorithm Correct Reconstruction Efficiency

The efficiency in the algorithm can be calculated with three methods discussed in [46]. The following two give the highest and lowest efficiencies, respectively:

$$Efficiency = \langle\langle f\rangle/\langle n\rangle\rangle, \tag{4.10}$$

where f is the number of correct reconstructions and n is the number of simulations run. By a correct reconstruction, of course, it is meant the finding of the correct decay vertex, which implies the correct reconstruction of two decay tracks. Equation 4.10 gives the highest efficiency, relative to other methods to determine the efficiency of the algorithm. The following gives the lowest efficiency:

$$Efficiency = f/n. \tag{4.11}$$

In order to balance the best and worst case scenarios, one can use a third method, also proposed in [46], which gives a number in between the results yielded by the two equations above. This is with the intention of being conservative about the predictions of the real detector's efficiency:

$$Efficiency = \langle f \rangle / \langle n \rangle. \tag{4.12}$$

The efficiency plot shown in Figure 4.7 was generated using Equation 4.12. The data was separated into chunks of 25 runs for 100 runs so that Equation 4.12 in reality looks like this:

$$Efficiency = \langle f \rangle / 25. \tag{4.13}$$

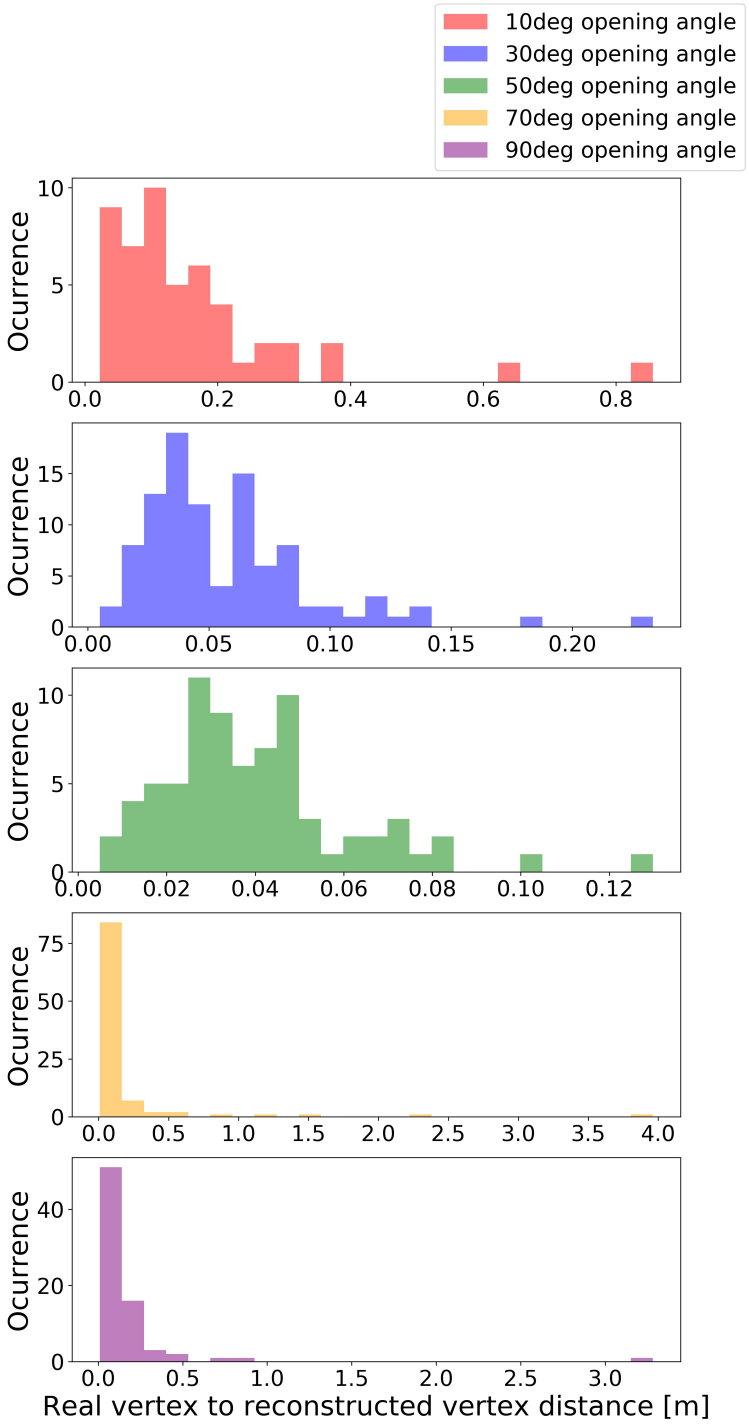

Figure 4.6: Histogram of the data generated for the distance between the reconstructed vertices to the coordinate system's origin.

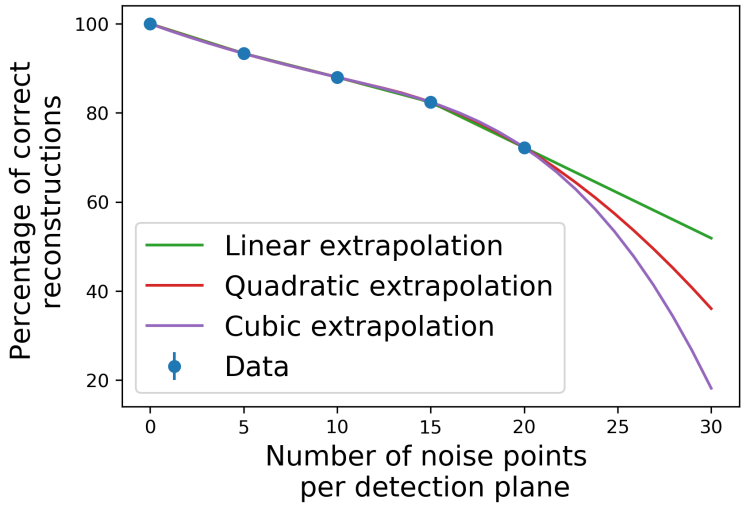

Figure 4.7: Vertex reconstruction algorithm efficiency results for 0, 5, 10, 15, and 20 noise points per plane for an opening angle of 110° and a rotation angle of 80. Three different extrapolations provided: linear, quadratic and cubic. The efficiency of the algorithm in reconstructing real vertices is at 100 % with zero noise points per detection plane, with an average of (92 ± 4) % between 0 and 10 noise points per plane, and (85 ± 5) %, on average, between 0 and 20 noise points per detection wall. The error bars in the plot are too small to be visible.

4.3 Further Work

The algorithm presented here is a test code and further work is needed to complete the studies of the tracking and vertexing algorithms described above. For example, studies need to be performed where the vertex position within the box is varied in addition to the opening angle of the decay tracks and various levels of inefficiency are also needed to be considered. Further to these additional tests, the plan for the future is to develop a final algorithm that uses the exact geometry of the MAPP-2 detector and a complete picture of the response of the detector. The final code will be the one implemented at MAPP-2, and it will incorporate the procedure that gives the best results in terms of track and vertex reconstruction accuracy and efficiency.

Chapter 5

Electric Dipole Moment Energy Loss

The MAPP detector was constructed to search for FIPs avatars of new physics. An example of such a particle is a fourth generation heavy neutrino with an anomalously large EDM [23]. The first authors to write about the possibility of detecting such particles with a scintillator detector are Sher, *et. al* [49, 26, 50]. His approach to the calculation of the energy loss of a moving EDM in matter is revised here; his results are averaged over three possible orientations of the EDM with respect to the atomic electrons in the material through which the particle with anomalously large EDM traverses. Our results include the EDM of a particle with a general orientation as well as an average of the EDM over all angles.

Frank, *et. al* [23] explore the possibility of detecting a heavy neutrino with a large EDM with the MoEDAL-MAPP detector. Because large EDMs violate parity and time-reversal symmetries, the detection of permanent EDMs of particles would be a solid evidence of physics BSM. Furthermore, their detection will allow further exploration of CP violation at the TeV scale. The values of the EDM are model dependent, and there are several models that give rise to EDMs with the inclusion of a new heavy lepton generation. Such models include, multiple-Higgs models [51], leptoquark models [52], left-right models [53, 54, 55, 56], and the minimal supersymmetric standard model (MSSM) [57]. MoEDAL has adopted the upper bound of $10^{-15}e$ cm, as in [58, 26, 50].

Experimental bounds indicate that the mass of a heavy neutrino would be larger than 45 GeV [59]. If this is true, and the heavy neutrino is part of a fourth lepton generation, then it cannot be accommodated by minimal extension to the SM, as this is ruled out by the Higgs data [24]. Other models BSM, as cited above, do allow for another fermion generation, however.

Frank, *et. al* [23] take an effective Lagrangian approach, pioneered by Sher, *et. al* [58, 26, 50]. In particular, we cast a wide net in modelling the heavy neutrinos

by using the Lagrangian

$$\mathcal{L}_N = \bar{N}\left(i\partial\!\!\!/ - M_N\right)N + ieD\bar{N}\sigma_{\mu\nu}\gamma_5 N F^{\mu\nu} \tag{5.1}$$

$$+ ieD\tan(\theta_W)\bar{N}\sigma_{\mu\nu}\gamma_5 N Z^{\mu\nu} + \frac{e}{2\cos(\theta_W)}\sin(\theta_W)Z^0_\mu \bar{N}_L\gamma^\mu N_L. \tag{5.2}$$

Here, the non-SM heavy neutrino is described by the field N, and M_N is its mass. A^μ and Z^0_μ are the photon and Z^0 fields, respectively. eD is the magnitude of the electron EDM, and it could be as large as $10^{-15}e$ cm. $F^{\mu\nu} = \partial^\mu A^\nu - \partial^\nu A^\mu$ and $Z^{\mu\nu} = \partial^\mu Z^{0\nu} - \partial^\nu Z^{0\mu}$. This model was validated by using MadGraph. Frank, *et. al* first looked at $e^+e^- \to N\bar{N}$ and considered s-channel photons only. This was done by looking at the first Lagrangian interaction term. The implementation gave excellent results compared to analytic predictions. In addition, they proceeded to validate the second Lagrangian term, which is an effective low-energy dimension-five operator involving N, by "turning off" the other interaction terms. The validation required that the heavy neutrino, being a member of an isodoublet, would have the same interaction with the Z as a regular neutrino would.

Additionally to the validation of the effective Lagrangian approach, Frank, *et. al* [23] looked at the ionization loss due to the EDM of the heavy neutrino. A neutrino with a large EDM is expected to lose energy in the MAPP detector via electromagnetic interactions. Following Sher's approach [26, 50], [23] concludes that the energy loss of the EDM passing through the detector is

$$\frac{dE}{dx} = \pi N Z \frac{e^2}{4\pi\epsilon_0} D\gamma, \tag{5.3}$$

where Z is the nuclear charge and N is the neutron number. γ is the relativistic factor. This result, however, as discussed above, is not completely right; it is averaged over three possible orientations of the EDM with respect to the atomic electrons in the material with which the EDM interacts. This result is revised here by including the EDM of a particle with a general orientation as well as an average of the EDM over all angles.

We conclude, as shown in Appendix B, that the energy loss rate of the EDM passing through the material is

$$-\frac{dE}{dx} = \left(\frac{ke^2p^2\pi^3 n_e}{2v^2 m_e}\right)\left(4\pi\epsilon_0\frac{2m_e\gamma v^2}{\pi ep} - \frac{\langle\omega\rangle^2}{\gamma^2 v^2}\right), \tag{5.4}$$

where $k \equiv \frac{1}{4\pi\epsilon_0}$ and q was substituted by e, the unit charge. This equation can be expressed as

$$-\frac{dE_M}{dx} = \frac{\pi^2 epn_e\gamma}{4\pi\epsilon_0}\left(1 - \frac{1}{4\pi\epsilon_0}\frac{\pi ep}{2m_e}\frac{\langle\omega\rangle^2}{\gamma^3 v^4}\right). \tag{5.5}$$

This can be compared to Sher's results,

$$-\frac{dE_S}{dx} = \frac{\pi e p \gamma n_e}{4\pi\epsilon_0}, \tag{5.6}$$

by taking their ratio. This gives, substituting $p = vm/c$:

$$\frac{\frac{dE_M}{dx}}{\frac{dE_S}{dx}} = \pi\left(1 - \frac{1}{4\pi\epsilon_0}\frac{\pi e m}{2m_e c}\frac{\langle w\rangle^2}{\gamma^3 v^3}\right). \tag{5.7}$$

We consider two regimes: 1) high velocity regime and 2) low velocity regime. In the first case, as $v \to c$, $\gamma \to \infty$ and $\frac{1}{\gamma^3 v^3} \to 0$, which implies that the ratio simplifies to

$$\frac{-\frac{dE_A}{dx}}{-\frac{dE_S}{dx}} = \pi. \tag{5.8}$$

The reason for this result, a factor of π, is that Sher averages his result over three possible orientations of the EDM. The result that we provide here is a more general case. In the second case, after substituting $e = 1.6 \times 10^{-19}$ C, $\epsilon_0 = 8.85 \times 10^{-12}$ F·m, $m_e = 9.11 \times 10^{-31}$ kg into Equation 5.7, one obtains

$$\frac{-\frac{dE_A}{dx}}{-\frac{dE_S}{dx}} = \pi\left(1 - 8.2689 \times 10^{12}\frac{m\langle\omega\rangle^2}{\gamma^3 v^3}\right). \tag{5.9}$$

Normally it is assumed that one can only register the presence of a neutral particle by its "missing energy-momentum", even if the particle has an anomalously large EDM [49]. However, we have shown that by using a dedicated detector like MAPP-1, with 3 m of scintillator readout by four PMTs as the sensitive element, an anomalously large EDM might be detected by its ionization signal as it passes through the detector if it gives rise to 100 photons or more in each of the 4 sections of the MAPP-1 detector [23]. A rough order-of-magnitude estimate tells us that 10^4 photons are produced per MeV of energy deposited in the plastic scintillator [59, 23, 60], meaning that if a unit charge produces 10^4 photons, an mCP with a charge of $e/10$ will produce 100 photons, for instance. Figure 5.1 shows the reach of EDM detection by MAPP compared to the Large Electron-Positron (LEP) collider in an EDM size vs the mass of a heavy neutrino. Further studies, using full simulation, on MAPP's ability to observe a neutral particle with an anomalously large EDM interaction with the plastic, are currently underway (Chapter 4).

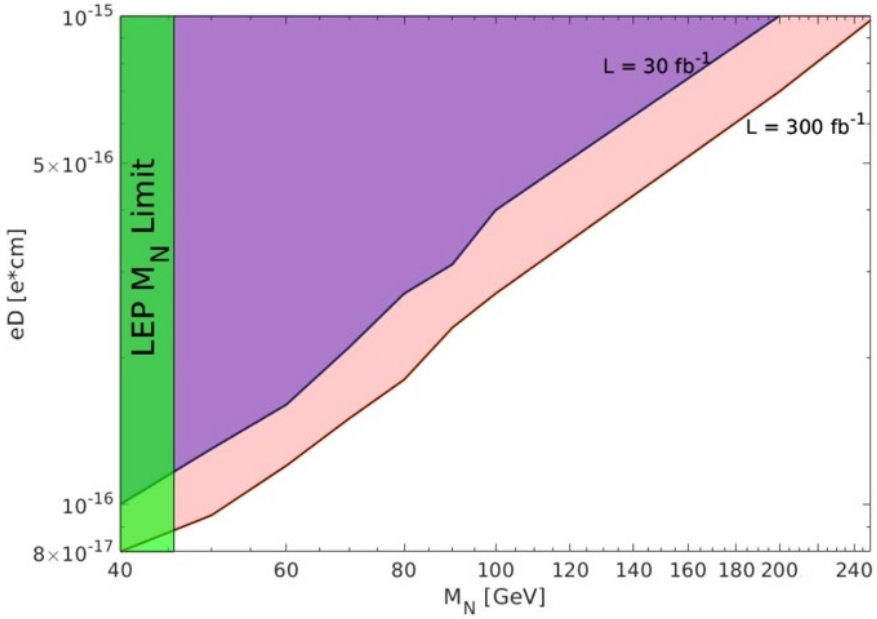

Figure 5.1: The reach for EDM detection at MoEDAL's MAPP detector at $\sqrt{s} = 14$ TeV, with 3 or more events observed at 95 % C.L., and 30 fb^1 and 300 fb^1 of integrated luminosity. The vertical axis has the value of the EDM and the horizontal axis, the mass of a heavy neutrino. Taken from [23].

Chapter 6

Conclusion

MoEDAL was the first dedicated detector to be installed at the LHC. It is designed to search for HIP avatars of BSM Physics. The purpose of the MAPP addition to the MoEDAL experiment is to expand MoEDAL's physics reach to include the search for FIP and LLP messengers of new physics. MAPP's phase 1 incarnation, or MAPP-1, is dedicated to the quest for mCPs and other FIPs, such as particles with an anomalously large EDM. MAPP-1 also has some sensitivity to neutral LLPs. During Run-3, MAPP-1 will also be used to monitor MoEDAL trapping volumes for the presence of trapped very Long-Lived electrically Charged Particles (LLCPs). It is envisaged that MAPP-1 will be able to detect trapped LLCPs with lifetimes in excess of 10 years. MAPP-2, the second phase of the MAPP detector, will be installed in the next long LHC shutdown preceding the envisaged startup of the high-luminosity LHC, in 2029. MAPP-2 is designed to greatly expand MoEDAL-MAPP's sensitivity to LLPs.

This thesis is divided into two main parts describing: 1) the work I performed in the construction and testing of the MAPP-1 detector, as well as potential physics topics for MAPP-1 and 2) the studies I performed on the tracking of charged particles in the MAPP-2 detector. I began my work on MAPP-1 by planning the procedures for the light-tight wrapping of the 400 scintillator bars comprising the MAPP-1 detector. I then took part in the inspection, re-polishing (if needed), and wrapping of the bars. In addition, I designed the coupling of the bar and light-guide to the PMT. This was achieved mechanically using a mount that keeps the PMT and light guide fixed in place. Furthermore, I outlined the procedures for the installation of the LED calibration system for MAPP-1. This included installing a blue LED and accompanying circuit board attached to the "non-PMT" end of each scintillator bar. The installation of these LEDs allows for the calibration of each bar for standard ionizing particles and for mCPs. Lastly, I participated in the fabrication of the prototype MAPP-1 veto-system scintillator-tiles for testing.

An important part of my commitment to the preparation for MAPP-1 for data

taking at LHC's Run-3 was the HV testing of 300 of the 400 3.1" PMTs needed to read out the detector. The shortfall of 100 PMTs was due to our supplier HZC Photonics shutting down operations due to Covid-related financial problems. In order to perform the tests, I adapted an existing laser test bed by designing an optical table, allowing the laser beam to be used to test four PMTs at a time. I also prepared the DAQ system in which all the data that I collected was via a digital-to-analog converter. I used this system to "plateau" each PMT allowing us to find their optimum HV operating point. During testing, I identified 14 PMT systems with malfunctioning electronic bases that have since been repaired.

Moving to MAPP-2, I developed a preliminary version of the tracking and vertexing software for the MAPP-2 detector. In order to do this, I utilized as a model a smaller test detector which is based on a "Russian-doll" model of concentric boxes to be used in the full detector design. I used this model detector to test our ability to determine the vertex of particles decaying in flight within the decay volume. The results obtained indicate that a reconstruction of the decay vertex can be known to a resolution of the order of 1 cm. In addition, the efficiency of the algorithm is expected to be in excess of 92% with ten noise points per detection plane, rising to 100% with no noise points.

Turning now to our ongoing investigations of FIPs, in the form of neutral particles with anomalously large EDM, I took part in an investigation regarding the expected energy loss of such particles in MAPP-1 scintillators. In this case, we hypothesized a heavy neutrino, a member of a fourth-generation lepton doublet, with an anomalously large electric dipole moment (EDM). In this model the heavy neutrino is produced in association with a heavy lepton [23]. The energy loss by ionization of such a particle does not follow the Bethe-Bloch formalism [49, 26, 58]. I took part in a re-calculation of the energy loss of a neutral particle with an EDM in order to properly take into account the effect of the orientation of the EDM with respect to the electron with which it interacts. This was done by taking an average over all angles of incidence. We expect our result to lead to a new publication re-assessing the sensitivity of MAPP to the heavy neutrino hypothesized in our paper.

The MoEDAL-MAPP detector is the only dedicated search detector with competitive sensitivity to all three types of new particles: HIPs, FIPs, and LLPs, which the main general-purpose LHC detectors (ATLAS and CMS) are not optimized to detect. The work described here will be utilized and developed during Phase-1 (Run-3) and Phase-2 (Run-4 and beyond) of the MoEDAL-MAPP project, with the aim of maximizing the discovery potential of the LHC.

Bibliography

[1] G. Aad and et al. "Observation of a new particle in the search for the Standard Model Higgs boson with the ATLAS detector at the LHC". In: *Physics Letters B* 716.1 (2012), pp. 1–29. ISSN: 0370-2693. DOI: 10.1016/j.physletb.2012.08.020. URL: https://www.sciencedirect.com/science/article/pii/S037026931200857X (cit. on p. 1).

[2] S. Chatrchyan and et al. "Observation of a new boson at a mass of 125 GeV with the CMS experiment at the LHC". In: *Physics Letters B* 716.1 (2012), pp. 30–61. ISSN: 0370-2693. DOI: 10.1016/j.physletb.2012.08.021. URL: https://www.sciencedirect.com/science/article/pii/S0370269312008581 (cit. on p. 1).

[3] D. Griffiths. *Introduction to Elementary Particles*. 2nd, revised ed. Wiley-VCH, 2008 (cit. on pp. 1, 5).

[4] CERN. *MoEDAL-MAPP*. URL: https://home.cern/science/experiments/moedal-mapp (cit. on p. 1).

[5] Wikipedia. *MoEDAL Experiment*. URL: https://en.wikipedia.org/wiki/MoEDAL_experiment (cit. on p. 1).

[6] J.L. Pinfold. "The MoEDAL Experiment: A New Light on the High Energy Frontier". In: *Phil. Trans. R. Soc. A. 377* (). DOI: 10.1098/rsta.2019.0382. URL: http://doi.org/10.1098/rsta.2019.0382 (cit. on pp. 1–3, 10, 24).

[7] J.L. Pinfold and et al. "MoEDAL-MAPP, an LHC Dedicated Detector Search Facility". In: (2022). DOI: 10.48550/ARXIV.2209.03988. URL: https://arxiv.org/abs/2209.03988 (cit. on pp. 2, 8, 9, 23).

[8] B. Acharya and et al. "The physics programme of the MoEDAL experiment at the LHC". In: *International Journal of Modern Physics A* 29.23 (Sept. 2014), p. 1430050. DOI: 10.1142/s0217751x14300506. URL: https://doi.org/10.1142%5C%2Fs0217751x14300506 (cit. on p. 2).

[9] B. Acharya and et al. "Search for magnetic monopoles with the MoEDAL forward trapping detector in 2.11 fb 1 of 13 TeV proton-proton collisions at the LHC". In: *Physics Letters B* 782 (May 2018). DOI: 10.1016/j.physletb.2018.05.069 (cit. on p. 2).

[10] B. Acharya and et al. "Search for magnetic monopoles with the MoEDAL prototype trapping detector in 8 TeV proton-proton collisions at the LHC". In: *Journal of High Energy Physics* 2016.8 (Aug. 2016). DOI: 10.1007/jhep08(2016)067. URL: https://doi.org/10.1007%5C%2Fjhep08%5C%282016%5C%29067 (cit. on p. 2).

[11] B. Acharya and et al. "Search for Magnetic Monopoles with the MoEDAL Forward Trapping Detector in 13 TeV Proton-Proton Collisions at the LHC". In: *Physical Review Letters* 118.6 (Feb. 2017). DOI: 10.1103/physrevlett.118.061801. URL: https://doi.org/10.1103%5C%2Fphysrevlett.118.061801 (cit. on p. 2).

[12] J. Ellis and et al. "The price of an electroweak monopole". In: *Physics Letters B* 756 (May 2016), pp. 29–35. DOI: 10.1016/j.physletb.2016.02.048. URL: https://doi.org/10.1016%5C%2Fj.physletb.2016.02.048 (cit. on p. 2).

[13] S. Baines and et al. "Monopole production via photon fusion and Drell–Yan processes: MadGraph implementation and perturbativity via velocity-dependent coupling and magnetic moment as novel features". In: *The European Physical Journal C* 78.11 (Nov. 2018). DOI: 10.1140/epjc/s10052-018-6440-6. URL: https://doi.org/10.1140%5C%2Fepjc%5C%2Fs10052-018-6440-6 (cit. on p. 2).

[14] B. Acharya and et al. "Magnetic Monopole Search with the Full MoEDAL Trapping Detector in 13 TeV *pp* Collisions Interpreted in Photon-Fusion and Drell-Yan Production". In: *Physical Review Letters* 123.2 (July 2019). DOI: 10.1103/physrevlett.123.021802. URL: https://doi.org/10.1103%5C%2Fphysrevlett.123.021802 (cit. on p. 2).

[15] B. Acharya and et al. "Search for highly-ionizing particles in *pp* collisions at the LHC's Run-1 using the prototype MoEDAL detector". In: *Eur. Phys. J. C* 82.8 (2022), p. 694. DOI: 10.1140/epjc/s10052-022-10608-2. arXiv: 2112.05806 [hep-ex] (cit. on p. 2).

[16] B. Acharya and et al. "First Search for Dyons with the Full MoEDAL Trapping Detector in 13 TeV *pp* Collisions". In: *Physical Review Letters* 126.7 (Feb. 2021). DOI: 10.1103/physrevlett.126.071801. URL: https://doi.org/10.1103%5C%2Fphysrevlett.126.071801 (cit. on p. 2).

[17] B. Acharya and et al. “Search for magnetic monopoles produced via the Schwinger mechanism”. In: *Nature* 602.7895 (2022). DOI: 10.1038/s41586-021-04298-1. eprint: 2106.11933[hep-ex] (cit. on p. 2).

[18] O. Gould and et al. “Towards Schwinger production of magnetic monopoles in heavy-ion collisions”. In: *Phys. Rev. D* 100 (1 July 2019), p. 015041. DOI: 10.1103/PhysRevD.100.015041. URL: https://link.aps.org/doi/10.1103/PhysRevD.100.015041 (cit. on p. 2).

[19] Y. Fukuda and et al. “Evidence for Oscillation of Atmospheric Neutrinos”. In: *Phys. Rev. Lett.* 81 (8 Aug. 1998), pp. 1562–1567. DOI: 10.1103/PhysRevLett.81.1562. URL: https://link.aps.org/doi/10.1103/PhysRevLett.81.1562 (cit. on p. 5).

[20] J.-L. Basdevant and J. Dalibard. *The Quantum Mechanics Solver: How to Apply Quantum Theory to Modern Physics*. 3rd. ed. Springer, 2019 (cit. on p. 5).

[21] Wikipedia. *Neutrino Oscillations*. October 17, 2020. URL: https://en.wikipedia.org/wiki/Neutrino%20oscillation#cite%20note-16 (cit. on p. 5).

[22] A. Blondel. “The number of neutrinos and the Z line shape”. In: *Comptes Rendus Physique* 3.9 (2002), pp. 1155–1164. ISSN: 1631-0705. DOI: 10.1016/S1631-0705(02)01393-2. URL: https://www.sciencedirect.com/science/article/pii/S1631070502013932 (cit. on p. 5).

[23] M. Frank, M. de Montigny, P.-P. A. Ouimet, J.L. Pinfold, A. Shaa, and M. Staelens. “Searching for heavy neutrinos with the MoEDAL-MAPP detector at the LHC”. In: *Physics Letters B* 802 (2020), p. 135204. ISSN: 0370-2693. DOI: https://doi.org/10.1016/j.physletb.2020.135204. URL: https://www.sciencedirect.com/science/article/pii/S0370269320300083 (cit. on pp. 5, 6, 66–69, 71).

[24] P.P. Giardino, K. Kannike, I. Masina, M. Raidal, and A. Strumia. “The universal Higgs fit”. In: *Journal of High Energy Physics* 2014.5 (May 2014). DOI: 10.1007/jhep05(2014)046. URL: https://doi.org/10.1007%5C%2Fjhep05%5C%282014%5C%29046 (cit. on pp. 5, 66).

[25] K. Ishiwata and M.B. Wise. “Higgs Properties and Fourth Generation Leptons”. In: *American Physical Society* 84(5) (2011). DOI: 10.1103/PhysRevD.84.055025 (cit. on pp. 5, 6).

[26] M. Sher and S. Nie. “Large Electric Dipole Moments of Heavy Neutrinos”. In: *Physical Review D* 65(093018) (May 21, 2002). DOI: 10.1103/physrevd.65.093018. URL: https://doi.org/10.1103%5C%2Fphysrevd.65.093018 (cit. on pp. 6, 66, 67, 71).

[27] J.L. Pinfold. "The MoEDAL Experiment at the LHC—A Progress Report". In: *Universe* 5.2 (2019). ISSN: 2218-1997. DOI: 10.3390/universe5020047. URL: https://www.mdpi.com/2218-1997/5/2/47 (cit. on p. 6).

[28] M. Staelens. *The Search for New Physics at the LHC with the MoEDAL-MAPP Detector and an Investigation of Emergent Magnetic Monopole Like Excitations in an Exotic Condensed Matter System*. PhD thesis, University of Alberta, 2021 (cit. on pp. 6, 7).

[29] A. Haas, C.S. Hill, E. Izaguirre, and I. Yavin. "Looking for milli-charged particles with a new experiment at the LHC". English (US). In: *Physics Letters, Section B: Nuclear, Elementary Particle and High-Energy Physics* 746 (June 2015), pp. 117–120. ISSN: 0370-2693. DOI: 10.1016/j.physletb.2015.04.062 (cit. on p. 6).

[30] J. Alimena and et al. "Searching for long-lived particles beyond the Standard Model at the Large Hadron Collider". In: *Journal of Physics G: Nuclear and Particle Physics* 47.9 (Sept. 2020), p. 090501. DOI: 10.1088/1361-6471/ab4574. URL: https://doi.org/10.1088%5C%2F1361-6471%5C%2Fab4574 (cit. on p. 8).

[31] CERN. "ATLAS Sets New Limits on Exotic Types of Long-Lived Particles". In: (2020). URL: https://home.cern/news/news/physics/atlas-sets-new-limits-exotic-types-long-lived-particles#:~:text=Long%5C%2Dlived%5C%20particles%5C%20are%5C%20a,manifestations%5C%20is%5C%20supersymmetry%5C%20(SUSY) (cit. on p. 8).

[32] F. Deppisch, S. Kulkarni, and W. Liu. "Heavy neutrino production via Z at the lifetime frontier". In: *Physical review D: Particles and fields* 100 (Aug. 2019), p. 035005. DOI: 10.1103/PhysRevD.100.035005 (cit. on p. 8).

[33] S.W. Moser, W.F. Harder, C.R. Hurlbut, and M.R. Kusner. "Principles and practice of plastic scintillator design". In: *Radiation Physics and Chemistry* 41.1 (1993), pp. 31–36. ISSN: 0969-806X. DOI: 10.1016/0969-806X(93)90039-W. URL: https://www.sciencedirect.com/science/article/pii/0969806X9390039W (cit. on p. 13).

[34] A.J. Davis and et al. "Scintillating Opritcal Fiber Trajectory Detectors". In: *Nuclear Instruments and Methods in Physics Research Section A: Accelerators, Spectrometers, Detectors and Associated Equipment* 276(1-2) (1989). ISSN: 0168-9002. DOI: 10.1016/0168-9002(89)90651-7 (cit. on p. 13).

[35] M. Ziering and S. Franzen. "The Franck-Condon Principle". In: *ChemistryLibreTexts* (2020). URL: https://chem.libretexts.%20org/Courses/Pacific_Union_College/Quantum_Chemistry/13%5C%3A_Molecular_

Spectroscopy/13.07%5C%3A_The_Franck-Condon_Principle (cit. on p. 16).

[36] O.V. Borshchev, N.M. Surin, and S.A. Pnomarenk. "Highly Efficient Wavelength Shifters: Design, Properties, and Applications". In: *Enikolopoc Institute of Synthetic Polymeric Materials, Russian Academy of Sciences* (2019). URL: http://ineosopen.%20org/io1916r (cit. on p. 17).

[37] Hamamatsu Photonics K.K. "Photomultiplier Tibes - Photomultiplier Tubes and Related Products". In: (2016). URL: https://www.optixs.cz/data/ke-stazeni/fotonasobice---katalog-d687.pdf (cit. on pp. 19, 20).

[38] W.R. Leo. *Techniques for Nuclear and Particle Physics Experiments - A How-to Approach*. 2nd revised ed. Springer-Verlag, 1994 (cit. on p. 19).

[39] G.F. Knoll. *Radiation Detection and Measurement*. 3rd. Wiley, 200 (cit. on p. 24).

[40] Ketek. *SiPM - Silicon Photomultiplier PM3315-WB-C0 - Produc Data Sheet*. URL: https://www.ketek.net/wp-content/uploads/KETEK-PM3315-WB-C0-Datasheet.pdf (cit. on pp. 25, 26).

[41] A.A. Salazar. "MoEDAL MAPP Detector for Detection of Physics Beyond the Standard Model at the LHC - Progress Report". In: (2020) (cit. on pp. 27, 30).

[42] B. Acharya and et al. "MAPP Phase-1 Technical Proposal". In: *CERN Document Server* (2021). URL: https://cds.cern.ch/record/2791293/files/LHCC-P-022.pdf (cit. on p. 37).

[43] The Dow Chemical Company. *Sylgard 184 Silicone Elastomer - Technical Data Sheet*. 2017. URL: https://www.dow.com/content/dam/dcc/documents/en-us/productdatasheet/11/11-31/11-3184-sylgard-184-elastomer.pdf (cit. on p. 41).

[44] V. Prajzler, M. Neruda, and M. Květoň. "Flexible multimode optical elastomer waveguides". In: *Journal of Materials Science: Materials in Electronics* 30 (Sept. 2019). DOI: 10.1007/s10854-019-02087-1 (cit. on p. 42).

[45] V. Prajzler, M. Neruda, and P. Nekvindová. "Flexible multimode polydimethyl-diphenylsiloxane optical planar waveguides". In: *Journal of Materials Science: Materials in Electronics* 29 (Apr. 2018), pp. 1–7. DOI: 10.1007/s10854-018-8560-z (cit. on p. 42).

[46] R.K. Bock, H. Grote, D. Notz, and M. Regler. *Data Analysis Techniques for High-Energy Physics Experiments*. Cambridge Univeristy Press, 1990 (cit. on pp. 53, 54, 62).

[47] JMP Statistical Discovery. *The Method of the Least Squares*. URL: https://www.jmp.com/en_ca/statistics-knowledge-portal/what-is-regression/the-method-of-least-squares.html (cit. on p. 59).

[48] I.G. Hughes and T.P.A. Hase. *Measurements and their Uncertainties - A Practical Guide to Modern Error Analysis*. Oxford University Press, 2010 (cit. on p. 61).

[49] M. Sher and J.R. Stevens. "Detecting a Heavy Neutrino Electric Dipole Moment at the LHC". In: *ArXiV* (December 12, 2017). DOI: 10.48550/arXiv.1710.06894. URL: https://doi.org/10.1016%5C%2Fj.physletb.2017.12.022 (cit. on pp. 66, 68, 71).

[50] M. Sher and J.R. Stevens. "Detecting a heavy neutrino electric dipole moment at the LHC". In: *Physics Letters B* 777 (2018), pp. 246–249. ISSN: 0370-2693. DOI: https://doi.org/10.1016/j.physletb.2017.12.022. URL: https://www.sciencedirect.com/science/article/pii/S0370269317309991 (cit. on pp. 66, 67).

[51] V. Barger, A. Das, and C. Kao. "Electric dipole moment of the muon in a two Higgs doublet model". In: *Phys. Rev. D* 55 (11 June 1997), pp. 7099–7106. DOI: 10.1103/PhysRevD.55.7099. URL: https://link.aps.org/doi/10.1103/PhysRevD.55.7099 (cit. on p. 66).

[52] W. Bernreuther, A. Brandenburg, and P. Overmann. "CP violation beyond the standard model and tau pair production in e+e collisions". In: *Physics Letters B* 391.3 (1997), pp. 413–419. ISSN: 0370-2693. DOI: https://doi.org/10.1016/S0370-2693(96)01501-8. URL: https://www.sciencedirect.com/science/article/pii/S0370269396015018 (cit. on p. 66).

[53] J.F. Nieves, D. Chang, and P.B. Pal. "Electric dipole moment of the electron in left-right-symmetric theories". In: *Phys. Rev. D* 33 (11 June 1986), pp. 3324–3328. DOI: 10.1103/PhysRevD.33.3324. URL: https://link.aps.org/doi/10.1103/PhysRevD.33.3324 (cit. on p. 66).

[54] J.W.F. Valle. "Leptonic CP violation and left-right symmetry". In: *Physics Letters B* 138.1 (1984), pp. 155–158. ISSN: 0370-2693. DOI: https://doi.org/10.1016/0370-2693(84)91891-4. URL: https://www.sciencedirect.com/science/article/pii/0370269384918914 (cit. on p. 66).

[55] H.-Y. Cheng. "Kobayashi-Maskawa type of hard-CP-violation model with three-generation Majorana neutrinos". In: *Phys. Rev. D* 34 (9 Nov. 1986), pp. 2794–2802. DOI: 10.1103/PhysRevD.34.2794. URL: https://link.aps.org/doi/10.1103/PhysRevD.34.2794 (cit. on p. 66).

[56] K.S. Babu and R.N. Mohapatra. "Enhanced electric dipole moment of the muon in the presence of large neutrino mixing". In: *Phys Rev Lett* 85 (24 2000). DOI: 10.1103/PhysRevLett.85.5064 (cit. on p. 66).

[57] F. del Águila, M.B. Gavela, J.A. Grifols, and A. Méndez. "Specifically supersymmetric contribution to electric dipole moments". In: *Physics Letters B* 126.1 (1983), pp. 71–73. ISSN: 0370-2693. DOI: https://doi.org/10.1016/0370-2693(83)90018-7. URL: https://www.sciencedirect.com/science/article/pii/0370269383900187 (cit. on p. 66).

[58] M. Sher. "Large Electric Dipole Moments of Heavy Leptons". In: *Physical Review Letters* 87(161801) (October 1, 2001). DOI: 10.1103/PhysRevLett.87.161801 (cit. on pp. 66, 71).

[59] J. Bailey and et. al. "New limits on the electric dipole moment of positive and negative muons". In: *Journal of Physics G: Nuclear Physics* 4.3 (Mar. 1978), p. 345. DOI: 10.1088/0305-4616/4/3/010. URL: https://dx.doi.org/10.1088/0305-4616/4/3/010 (cit. on pp. 66, 68).

[60] M. Tabanashi and et al. "Review of Particle Physics". In: *Phys. Rev. D* 98 (3 Aug. 2018), p. 030001. DOI: 10.1103/PhysRevD.98.030001. URL: https://link.aps.org/doi/10.1103/PhysRevD.98.030001 (cit. on p. 68).

[61] J.D. Jackson. *Classical Electrodynamics*. 3rd ed. Wiley, 1999 (cit. on pp. 80, 88).

[62] G.P. Fischer. "The Electric Dipole Moment of a Moving Magnetic Dipole". In: *American Journal of Physics* 39(1528) (1971). DOI: 10.1119/1.1976708 (cit. on p. 80).

[63] J. Franklin. "Complete Lorentz Transformation of a Charge-Current Density". In: *ArXiV* (2016). DOI: 10.48550/arXiv.1603.02912 (cit. on p. 80).

Appendix A

Vertex Reconstruction Algorithm

The vertex reconstruction algorithm described in this thesis can be found in the GitHub repository: `https://github.com/aasalaza/MAPP-2-Test-Detector-Vertex-Reconstruction-Algorithm.git`.

Appendix B

Electric Dipole Moment Energy Loss Calculations

The problem arises from Jackson's Classical Electrodynamics [61] (Problem 11.27):

(a) A charge density of ρ' of zero total charge, but with a dipole moment $\mathbf{p}$, exists in reference frame K'. There is no current density in K'. The frame K' moves with a velocity $\mathbf{v} = \beta c$ in the frame K. Find the charge and current densities ρ and $\mathbf{J}$ in the frame K and show that there is a magnetic dipole moment, $\mathbf{m} = (\mathbf{p} \times \beta)/2$, correct to first order in β. What is the electric dipole moment in K to the same order in β?

(b) Instead of the charge density, but no current density, in K', consider no charge density, but a current density $\mathbf{J}'$ that has a magnetic dipole moment $\mathbf{m}$. Find the charge and current densities in K and show that to first order in β there is an electric dipole moment $\mathbf{p} = \beta \times \mathbf{m}$ in addition to the magnetic dipole moment.

We focus on part (b) of the problem, and provide an answer to the question of whether a moving magnetic dipole induces an electric dipole moment. In doing so, we revise the conclusion made by Fischer [62] in that indeed, a moving magnetic dipole induces an electric dipole moment. We expand on his method of derivation as per Franklin's argument that Fischer's derivation is incomplete [63]. We disagree with Franklin, however, in that Fischer's conclusion is false. Finally, we look at what the EDM is like for neutrons occurring at MAPP.

B.1 Physics of a Moving Electric Dipole

Let K be the rest frame of the moving electric dipole, and let K' be the lab frame. In addition, let K' be moving with a velocity $\mathbf{v} = \beta c$ with respect to K.

We assume that the charge density is time independent:

$$\rho = \rho(\vec{x}); \tag{B.1}$$

we also have, by definition, and by the problem conditions, that

$$q \equiv \int \rho d^3x = 0. \tag{B.2}$$

From Jackson, Eq. 4.8, we have that the electric dipole is defined as

$$\vec{p} \equiv \int \vec{x}\rho d^3x, \tag{B.3}$$

and the magnetic dipole is, from Jackson, Eq. 5.54,

$$\vec{m} = \frac{1}{2c}\int \vec{x} \times \vec{J} d^3x. \tag{B.4}$$

We construct the 4-current in the rest frame K. We have

$$J^\mu = (c\rho, 0). \tag{B.5}$$

And boosting in the lab frame, K',

$$J'^\mu = \left(c\rho, \gamma\vec{\beta}c\rho\right). \tag{B.6}$$

The Lorentz Transformations relate the coordinates in both reference frames as follows (Jackson, Eq. 11.19):

$$x'^0 = \gamma\left(x^0 - \vec{\beta}\cdot\vec{v}\right), \tag{B.7}$$

and

$$\vec{x}' = \vec{x} + \frac{\gamma - 1}{\beta^2}\vec{\beta}\left(\vec{\beta}\cdot\vec{x}\right) - \gamma\vec{\beta}x^0. \tag{B.8}$$

In addition, in the lab frame K', the charge density is

$$\rho'\left(x'^0, \vec{x}'\right) = \gamma\rho(\vec{x}), \tag{B.9}$$

and the current density is

$$\vec{J}\left(x'^0, \vec{x}'\right) = \gamma\beta c\rho(\vec{c}). \tag{B.10}$$

Equations B.3 & B.4 define the electric and magnetic dipoles, respectively, as integrations over the source densities at a fixed time x'^0 in the lab frame. This is true at any time, so we can simplify things by setting the time in the lab frame to zero: $x'^0 = 0$. Therefore, from Eq. B.7, we obtain

$$x'^0 = \gamma\left(x^0 - \vec{\beta}\cdot\vec{x}\right) = 0$$

$$\Rightarrow x^0 = \vec{\beta}\cdot\vec{x}. \tag{B.11}$$

From Eq. B.8, we have

$$\begin{aligned}
\vec{x}' &= \vec{x} + \frac{\gamma-1}{\beta^2}\vec{\beta}\left(\vec{\beta}\cdot\vec{x}\right) - \gamma\vec{\beta}\left(\vec{\beta}\cdot\vec{x}\right) \\
&= \vec{x} + \frac{\gamma-1}{\beta^2}\cdot\frac{\gamma+1}{\gamma+1}\vec{\beta}\left(\vec{\beta}\cdot\vec{x}\right) - \gamma\vec{\beta}\left(\vec{\beta}-\vec{x}\right) \\
&= \vec{x} + \frac{\gamma^2-1}{\beta^2\left(\gamma+1\right)}\vec{\beta}\left(\vec{\beta}\cdot\vec{x}\right) - \gamma\vec{\beta}\left(\vec{\beta}\cdot\vec{x}\right) \\
&= \vec{x} + \frac{\frac{1}{1-\beta^2}-1}{\beta^2\left(\gamma+1\right)}\vec{\beta}\left(\vec{\beta}\cdot\vec{x}\right) - \gamma\vec{\beta}\left(\vec{\beta}\cdot\vec{x}\right) \\
&= \vec{x} + \frac{\frac{\beta^2}{1-\beta^2}}{\beta^2\left(\gamma+1\right)}\vec{\beta}\left(\vec{\beta}\cdot\vec{x}\right) - \gamma\vec{\beta}\left(\vec{\beta}\cdot\vec{x}\right) \\
&= \vec{x} + \frac{\gamma^2}{\gamma+1}\vec{\beta}\left(\vec{\beta}\cdot\vec{x}\right) - \gamma\vec{\beta}\left(\vec{\beta}\cdot\vec{x}\right) \\
&= \vec{x} + \frac{1}{\gamma+1}\left[\gamma^2\vec{\beta}\left(\vec{\beta}\cdot\vec{x}\right) - \gamma^2\vec{\beta}\left(\vec{\beta}\cdot\vec{x}\right) - \gamma\vec{\beta}\left(\vec{\beta}\cdot\vec{x}\right)\right]
\end{aligned}$$

$$\Rightarrow \vec{x}' = \vec{x} - \frac{\gamma}{\gamma+1}\vec{\beta}\left(\vec{\beta}\cdot\vec{x}\right). \tag{B.12}$$

Time dilation at some fixed x'^0 relates the 3-volume integration in two frames as

$$\left[\int d^3x' = \frac{1}{\gamma}\int d^3x\right]_{x'^0=const}. \tag{B.13}$$

Applying this to the equation for the magnetic dipole, Eq. B.4, in the lab frame K', we get

$$
\begin{aligned}
\vec{m}' &= \frac{1}{2c}\int \vec{x}' \times \vec{J}' d^3x' \\
&= \frac{1}{2c}\int \vec{x}' \times \vec{J}' \frac{1}{\gamma} d^3x \\
&\uparrow \\
&\text{Eq. B.13} \\
&= \frac{1}{2c}\int \left[\vec{x} - \frac{\gamma}{\gamma+1}\vec{\beta}\left(\vec{\beta}\cdot\vec{x}\right)\right] \times \gamma\vec{\beta}c\rho\, \frac{1}{\gamma} d^3x. \\
&\uparrow \\
&\text{Eqs. B.12 \& B.10}
\end{aligned}
$$

The c's and γ's cancel out. Regrouping terms:

$$
\vec{m}' = \frac{1}{2}\left[\int \vec{x} \times \vec{\beta}\rho d^3x - \int \frac{\gamma}{\gamma+1}\vec{\beta}\left(\vec{\beta}\cdot\vec{x}\right) \times \vec{\beta}\rho d^3x\right].
$$

The second integral equals zero by the cross product (parallel vectors).

$$
\begin{aligned}
\vec{m}' &= \frac{1}{2}\int \rho\vec{x} \times \vec{\beta} d^3c \\
&= \frac{1}{2}\left(\int \rho\vec{x} d^3x\right) \times \vec{\beta}.
\end{aligned}
$$

Which, by Eq. B.3, gives

$$
\vec{m}' = \frac{1}{2}\vec{p} \times \vec{\beta}. \tag{B.14}
$$

This shows that a moving electric dipole induces a magnetic dipole moment proportional to its magnitude and perpendicular to it.

Finally, the electric dipole moment in the lab frame K' is

$$\begin{aligned}
\vec{p}' &= \int \vec{x}'\rho' d^3x' \\
&= \int \left[\vec{x} - \frac{}{\gamma+1}\left(\vec{\beta}\cdot\vec{x}\right)\right]\gamma\rho\frac{1}{\gamma}d^3x \\
&\uparrow \\
&\text{Eqs. B.12 \& B.13} \\
&= \int \rho\vec{x}d^3x - \int \frac{\gamma}{\gamma+1}\rho\vec{\beta}\left(\vec{\beta}\cdot\vec{x}\right)d^3x \\
&= \vec{p} - \frac{\gamma}{\gamma+1}\left(\vec{\beta}\right)\vec{\beta}\cdot\int\rho\vec{x}d^3x,
\end{aligned}$$

which, by Eq. B.3, gives

$$\vec{p}' = \vec{p} - \frac{\gamma}{\gamma+1}\vec{\beta}\left(\vec{\beta}\cdot\vec{p}\right). \tag{B.15}$$

B.2 Physics of a Moving Magnetic Dipole

Consider a magnetic dipole $\vec{m}$ in the rest frame K of the moving particle with current density $\vec{J}$ and no charge density. The 4-current in K is, from Jackson, Eq. (11.128),

$$J^\mu = \left(0, \vec{J}\right). \tag{B.16}$$

Then we boost this quantity to the lab frame K'. The Lorentz Transformation gives

$$J'^\mu = \left(\gamma\vec{\beta}\cdot\vec{J}, \vec{J} + \frac{\gamma-1}{\beta^2}\vec{\beta}\left(\vec{\beta}\cdot\vec{J}\right)\right) = \left(c\rho, \vec{\beta}c\rho\right). \tag{B.17}$$

The last equality comes from Eqs. B.6 & B.9. Then the EDM in the lab frame, by Eq. B.3, is

$$\vec{p}' = \int \vec{x}'\rho' d^3x' \tag{B.18}$$

$$\begin{aligned}
&= \int \left[\vec{x} - \frac{\gamma}{\gamma+1}\vec{\beta}\left(\vec{\beta}\cdot\vec{x}\right)\right]\frac{\gamma\vec{\beta}\cdot\vec{J}}{c}\,\frac{1}{\gamma}d^3x \\
&\uparrow \\
&\text{Eqs. B.12, B.17 \& B.13}
\end{aligned}$$

$$\Rightarrow \vec{p}' = \frac{1}{c}\int \left[\vec{x} - \frac{\gamma}{\gamma+1}\vec{\beta}\left(\vec{\beta}\cdot\vec{x}\right)\right]\vec{\beta}\cdot\vec{J}\,d^3x. \tag{B.19}$$

To solve this integral we notice the following:

$$\begin{aligned}
\int x_i J_j d^3x &= \frac{1}{2}\int \left(x_i J_j + x_j J_i\right) d^3x + \frac{1}{2}\int \left(x_i J_j - x_j J_i\right) d^3x \\
&= \frac{1}{2}\int \left(J_j \partial_j x_i x_j + J_i \partial_i x_i x_j\right) + \frac{1}{2}\int \epsilon_{ijk}\left(\vec{x}\times\vec{J}\right)_k d^3x \\
&\uparrow \\
&\text{By Product Rule and Levi-Civita symbol permutation} \\
&= \frac{1}{2}\int J_k \partial_k \left(x_j x_i\right) d^3x + \frac{1}{2}\epsilon_{ijk}\int \left(\vec{x}\times\vec{J}\right)_k d^3x \\
&= -\frac{1}{2}\int x_i x_j \left(\vec{\nabla}\cdot\vec{J}\right) d^3x + \frac{1}{2}\int \left(x_i x_j\right)\vec{J}\cdot\vec{n}dS + \frac{1}{2}\epsilon_{ijk}\int \left(\vec{x}\times\vec{J}\right)_k d^3x \\
&\uparrow \\
&\text{By the Divergence Theorem} \\
&= -\frac{1}{2}\int x_i x_j \left(\vec{\nabla}\cdot\vec{J}\right) d^3x + \frac{1}{2}\epsilon_{ijk}\int \left(\vec{x}\times\vec{J}\right)_k d^3x.
\end{aligned}$$

But in the rest frame of the moving dipole, K, the current density is time independent, i.e., static, so the divergence of the current density is zero: $\vec{\nabla}\cdot\vec{J} = 0$. We have

$$\int x_i J_i d^3x = \frac{1}{2}\epsilon ijk \int \left(\vec{x}\times\vec{J}\right)_k d^3x.$$

From Eq. B.4, we obtain

$$\int x_i J_j d^3x = c\epsilon_{ijk} m_k. \tag{B.20}$$

So the EDM is given by, from Eq. B.19,

$$\begin{aligned}
p_i' &= \frac{1}{c}\int x_i \beta_i J_i d^3x - \frac{1}{c}\frac{\gamma}{\gamma+1}\int \beta_i \beta_{ji} \beta_k J_k d^3x \\
&= \epsilon_{ijk}\beta_j m_k - \frac{\gamma}{\gamma+1}\beta_i \beta_j \epsilon_{jln}\beta_l m_n.
\end{aligned}$$

Then, to first order in β, by the property $(A\times B)_i = \epsilon_{ijk}A_j B_k$, the EDM in the lab frame is given by the expression

$$\vec{p}' = \vec{\beta}\times\vec{m}, \tag{B.21}$$

telling us that a moving magnetic dipole induces an electric dipole in the lab frame.

B.3 Energy Loss of an Electric Dipole

Now consider the passage of the electric dipole moment $\vec{p}$ through matter. The momentum transfer due to the inelastic collision with an atomic electron is given by

$$\vec{F} = \frac{d\vec{p}_m}{dt}, \tag{B.22}$$

where the subscript m stands for "momentum", which implies

$$\int d\vec{p}_m = \int \vec{F} dt = \Delta\vec{p}_m. \tag{B.23}$$

Now, the Lorentz force, on the atomic electron, assuming that the electron is at rest, is given by

$$\begin{aligned} \vec{F} = q\left(\vec{E} + \vec{v} \times \vec{B}\right) = q\vec{E}. \\ \uparrow \\ \vec{v} = 0 \end{aligned} \tag{B.24}$$

Therefore, Eq. B.23 gives

$$\Delta p_m = q \int \vec{E} dt. \tag{B.25}$$

The electric field of the electric dipole on the impact area can be found through the definition of the electric potential applied to an electric dipole. With the dipole moving along the z axis at a constant velocity, we have

$$\begin{aligned} V_{dipole}(r,\theta) &= \frac{\hat{r} \cdot \vec{p}}{4\pi\epsilon_0 r^2} \\ &= \frac{p\cos(\theta)}{4\pi\epsilon_0 r^2}. \end{aligned}$$

Then

$$\begin{aligned} E_r &= -\frac{\partial V}{\partial r} \\ &= \frac{2p\cos(\theta)}{4\pi\epsilon_0 r^3} \end{aligned}$$

and

$$\begin{aligned} E_\theta &= -\frac{1}{r}\frac{\partial V}{\partial \theta} \\ &= \frac{p\sin(\theta)}{4\pi\epsilon_0 r^3} \end{aligned}$$

imply that

$$\vec{E} = \frac{p}{4\pi\epsilon_0 r^3}\left(2\cos(\theta)\hat{r} + \sin(\theta)\hat{\theta}\right). \tag{B.26}$$

We define the impact parameter $b \equiv y$. Remembering that we are considering a dipole moving along the z axis at constant speed $\vec{v}$, we obtain

$$\begin{aligned} r &= z^2 + y^2 \\ &= (\vec{v}t)^2 + b^2. \end{aligned}$$

We can also rewrite the trigonometric identities as

$$\cos(\theta) = \frac{b}{r} \quad \text{and} \quad \sin(\theta) = \frac{vt}{r}.$$

Then Eq. B.26 can be written as

$$\begin{aligned} \vec{E} &= \frac{p}{4\pi\epsilon_0 r^3}\left(2\frac{b}{r}\hat{r} + \frac{vt}{r}\hat{\theta}\right) \\ &= \frac{p}{4\pi\epsilon_0}\left(2\frac{b}{r^4}\hat{r} + \frac{vt}{r^4}\hat{\theta}\right) \\ &= \frac{p}{4\pi\epsilon_0}\left(2\frac{b}{\left[(vt)^2 + b^2\right]^2}\hat{r} + \frac{vt}{\left[(vt)^2 + b^2\right]^2}\hat{\theta}\right). \end{aligned} \tag{B.27}$$

Going back to Eq. B.25, we integrate with respect to time:

$$\begin{aligned} \Delta\vec{p}_m &= q\int \vec{E}dt \\ &= q\int_{-\infty}^{+\infty} \frac{p}{4\pi\epsilon_0}\frac{2b}{\left[b^2 + (vt)^2\right]^2}\hat{r} + \int_{-\infty}^{+\infty}\frac{p}{4\pi\epsilon_0}\frac{vt}{\left[b^2 + (vt)^2\right]^2}\hat{\theta}. \end{aligned}$$

Then the expression for the change in momentum is

$$\Delta\vec{p}_m = \frac{qp}{4\pi\epsilon_0}\frac{\pi}{b^2 v}\hat{r}. \tag{B.28}$$

With this, the energy transfer at the impact parameter b is given by the expression

$$E(b) = \frac{(\Delta\vec{p})^2}{2m_e} = \frac{1}{2m_e}\left(\frac{qp}{4\pi\epsilon_0}\right)^2\left(\frac{\pi}{b^2 v}\right)^2. \tag{B.29}$$

Now we consider a volume element $dV = 2\pi b db dx$ and an electron number density n_e. Then

$$\begin{aligned} -dE(b) &= E(b) n_e dV \\ &= \frac{1}{m_e}\left(\frac{qp}{4\pi\epsilon_0}\right)^2\left(\frac{\pi}{b^2 v}\right)^2 n_e\left(2\pi b db dx\right), \end{aligned} \tag{B.30}$$

where the negative sign comes from the loss of energy. We have

$$\begin{aligned} \frac{dE(b)}{dx} &= \frac{d}{dx}E(b) n_e dV \\ &= \frac{1}{2m_e}\left(\frac{qp}{4\pi\epsilon_0}\right)^2\left(\frac{\pi}{b^2 v}\right)^2 n_e\left(2\pi b db\right). \end{aligned} \tag{B.31}$$

Finally, by integrating from b_{min} to b_{max}, to consider all the possible values of the impact parameter b, we obtain the following expression for the energy loss:

$$-\frac{dE(b)}{dx} = \left(\frac{\pi^3 n_e}{2v^2 m_e}\right)\left(\frac{qp}{4\pi\epsilon_0}\right)^2\left(\frac{1}{b_{min}^2} - \frac{1}{b_{max}^2}\right). \tag{B.32}$$

To determine b_{min}, look at the energy transfer in a head-on collision (no incidence angle). According to Jackson [61], this energy transfer is

$$E = 2\gamma^2 m_e v^2. \tag{B.33}$$

Then, using this equation and Eq. B.29, we obtain

$$b_{min}^2 = \frac{1}{4\pi\epsilon_0}\frac{\pi qp}{2m_e\gamma v}. \tag{B.34}$$

Also from Jackson [61], we have

$$b_{max}^2 = \frac{\gamma^2 v^2}{\langle\omega\rangle^2}, \tag{B.35}$$

where $\langle\omega\rangle$ is the frequency of motion of the electronic binding.

Considering this information, we arrive at the conclusion that

$$-\frac{dE}{dx} = \left(\frac{ke^2p^2\pi^3 n_e}{2v^2 m_e}\right)\left(4\pi\epsilon_0 \frac{2m_e\gamma v^2}{\pi ep} - \frac{\langle\omega\rangle^2}{\gamma^2 v^2}\right), \tag{B.36}$$

where $k \equiv \frac{1}{4\pi\epsilon_0}$ and q was substituted by e, the unit charge.